TÉCNICO LISBOA

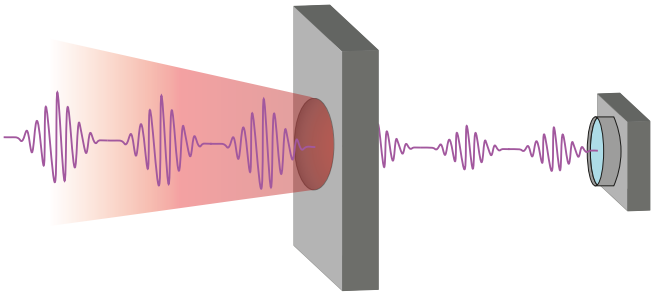

Time-resolved studies of Warm Dense Titanium:

A Bayesian search of coupling parameters

Sebastião Baptista Antunes

Thesis to obtain the Master of Science Degree in

Engineering Physics

Supervisor: Prof. Marta Leitão Mota Fajardo
Dr. Gareth Oisin Williams

Examination Committee

Chairperson:	Prof. João Alberto dos Santos Mendanha Dias
Supervisor:	Prof. Marta Leitão Mota Fajardo
Member of the Committee:	Prof. Hugo Fernando Santos Terças

November 2022

To my grandfathers Adelino e José

Acknowledgments

I would like to thank both of my supervisors Gareth and Marta for all their support, patience, and knowledge. They were an integral piece of the successful completion of this document and it was both a pleasure and a privilege working with them.

To Mariana, André and Patricia my office mates thank you for all the discussions and feedback and for putting up with me at my most burnt-out and crazed. Mariana thank you also for all the illustrations.

To my mom Helena and my dad Luis, who have been there since the beginning my most infinite gratitude. I would never be here without your encouragement, guidance, and love. Thanks are needed for my dad for proofreading my thesis as well, even though physics is really not his thing.

Thank you Violeta for believing when I doubted, lifting me when I fell and inspiring me to reach my full potential. Thank you as well for painstakingly going over every detail I need to clarify and for your multiple proofreads.

Finally a big and embracing thank you to all my friends and family (you know perfectly well who they are) who add color to my life and without whom I would certainly falter.

This work is supported by the European Union's Horizon 2020 research and innovation program under grant agreement 871161 and grant agreement No 101047223.

Resumo

Usou-se um impulso de laser infravermelho ultra-curto (10^14 W/cm^2, 50 fs, 800 nm), para criar plasmas de densidade sólida, com dezenas de eV de temperatura, de espessura comparável à profundidade de absorção do Titânio, nos 800 nm. A estrutura eletrónica da amostra aquecida foi sondada com um impulso XUV de energia próxima da borda de absorção $M_{2,3}$. O perfil espacial dos impulsos XUV transmitidos foi gravado numa única medição com uma resolução de (10 μm), e foi resolvido temporalmente em intervalos de 50 fs, com um tempo de aquisição máxima de cerca de 20 ps. Modelos foram depois usados para simular a respostas nas diferentes escalas temporais.

Palavras-chave: plasmas densos; geração de harmónicas de alta frequência; mapeamento ultra-rápido; plasmas fora do equilíbrio; interação laser-sólido de femtossegundos; inferência Bayesiana.

Abstract

An experimental set up consisting of an ultrashort infra-red laser pulse ($10^(14)$ W/cm^2, 50 fs, 800 nm) was used to create up to tens of eV solid-density plasma in the skin depth of a Ti metal film. The electronic structure of the heated sample was probed by sending a XUV pulse with energy close to that of the $M_{2,3}$ absorption edge. The transmitted XUVs spatial profile was recorded in a single-shot with 10 μm resolution, and scanned with up to 50 fs resolution, for tens of picoseconds. A map of XUV transmission for variable laser fluences was then recorded in every shot. Models were deployed to simulate the response in the different temporal scales at play.

Keywords: dense plasmas; high harmonic generation; ultrafast imaging; non-equilibrium plasmas, femtosecond laser-solid interaction; Bayesian parameter estimation.

Contents

Resumo . . . vii

Abstract . . . ix

List of Tables . . . xiii

List of Figures . . . xv

1 Introduction **1**

1.1 Applications . . . 1

1.2 WDM: In the crossroads between plasma and condensed matter . . . 3

1.2.1 Equilibrium distribution function: degeneracy . . . 3

1.2.2 Screening in Coulomb plasmas . . . 5

1.3 The Temperature - Density Plane . . . 7

1.4 Creating WDM states in the lab . . . 8

1.5 IH: Physical processes . . . 10

1.5.1 Absorption of Energy . . . 10

1.5.2 Relaxation processes . . . 12

1.5.3 The Two-temperature Model . . . 14

2 State of the art **17**

2.1 Probing non-equilibrium WDM states . . . 17

2.2 Simulating non-equilibrium WDM . . . 19

2.2.1 Hydrodynamic Regime . . . 19

2.2.2 Modelling electronic distribution of WDM . . . 21

2.2.3 The TTM and e-i coupling . . . 27

2.3 X-ray Absorption Near Edge Spectroscopy: XANES . . . 30

2.3.1 Aluminium . . . 31

2.3.2 Molybdenum . . . 32

2.3.3 Long lived non-thermal electrons: Copper . . . 33

2.4 Bayesian Inference: tackling uncertainty . . . 34

2.4.1 Priors and Likelihood . . . 35

2.4.2 Markov Chain Monte Carlo (MCMC) . . . 36

3 Experiment and Data **39**

3.1 Experimental Set Up . . . 39

3.2 Collected Data . . . 40

3.3 Feature Extraction . . . 42

3.3.1 Background removal . . . 42

3.3.2 Subdividing the zone of interest . . . 46

3.4 Results . . . 49

3.5 Summary and Conclusions . . . 53

4 Algorithms, Results and Discussion **55**

4.1 Forward Modelling the Relative XUV Transmission . . . 55

4.2 Two-Temperature Model . . . 58

4.2.1 MCMC searches with Lin's G_{ei} . . . 60

4.2.2 MCMC searches for constant G_{ei} . . . 69

4.2.3 Summary and Conclusions . . . 72

4.3 Quantum Boltzmann Statistics . . . 73

4.3.1 Analytical simplification of the collision terms . . . 73

4.3.2 Algorithm . . . 75

4.3.3 Analysis of solutions . . . 78

4.3.4 MCMC searches . . . 80

4.3.5 Summary and Conclusions . . . 86

5 Conclusions and Perspectives **87**

5.1 Contributions . . . 88

Bibliography **89**

A **95**

List of Tables

1.1 Table summary of the methods used to create warm dense matter. 8

3.1 Average w (where intensity decays to I_0/e^2) of the laser taking, in the Ti film plane, for each of the data families. 52

4.1 Theoretical (and normalizing) values of the free scale parameters of the TTM. 60

4.2 Most likely value and 1σ errors of the MCMC searches performed for a physical forward model of a TTM, with Lin-like coupling parameter and DOS as in equation 4.4. 61

4.3 Most likely value and 1σ errors of the 5 MCMC searches performed, one for each sub-zone, for a physical forward model of a TTM, with a constant coupling parameter and nearly free electron DOS. 70

4.4 Most likely value and 1σ errors of the 3 MCMC searches performed, one for each sub-zone, for a physical forward model of the Boltzmann equation 2.9, without the phonon term. 86

List of Figures

1.1 SEM micrographs of holes drilled in 100-μm-thick steel foils by ablation using laser pulses with the following parameters: (a) pulse duration (τ_p): 200 fs, pulse energy: 120 mJ, fluence (F): 0.5 J/cm^2, λ = 780 nm; and (b) τ_p =3.3 ns, pulse energy: 1 mJ, F = 4.2 J/cm^2, λ = 780 nm. The scale bars represent 30 μm. Integrally taken from [9]. 3

1.2 Chemical potential μ as a function of Θ. From [3]. 5

1.3 Temperature-density plane with several adimensional parameters plotted, for the equilibrium case, along with demarcations of different zones of physical and technological interest. From [11]. 8

1.4 Electron-ion collision frequency for solid Al, interpolated between known regimes, with resource to a harmonic mean. The dashed line represents the plausible requirement that the electron's mean free path is bigger than the ion radius. From [22]. 12

1.5 Sketch of energy deposition and relaxation processes in laser irradiated metal. First, the cold electronic population is excited into a non-thermal population, then the population thermalizes and forms a Fermi-Dirac before relaxation to the ions to a joint temperature. From [17]. . . . 13

2.1 Energy diagram of different core states transitions to near continuum states. E_f is the Fermi energy and the different edges are labeled. Adapted from [29]. 19

2.2 Temperature-desity profile of an Al sample irradiated for 150 fs with a 400 nm pulse with intensity $I = 10^{15}$ W/cm^2. Adapted from [21]. 20

2.3 Electornic density of states (DOS) for Al and Ti at finite temperatures. The dashed lines are the chemical potentials and the dots overlaid are the corresponding Fermi-Dirac distributions. Adapted from [35]. 23

2.4 Modulus squared of the screened two-particle interaction potential for e-i and electrons-phonon interactions. From [40]. 27

2.5 Electron ion coefficient G as a function of T_e obtained in [41]. 29

2.6 Electron ion coefficient G as a function of T_e obtained from the different references mentioned above. Adapted from [10]. 30

2.7 Ab initio QMD simulations of Al-K edge XANES spectra, for different (equilibrated) temperatures and solid density. Adapted from [29]. 32

2.8 Time evolution of XANES near the K-edge for a 100nm isochorically heated Al sample. From [38]. . . . 32
2.9 Ab initio QMD simulation of Al-K edge XANES spectra for non-equilibrium at solid density. From [29]. . . . 32
2.10 Ab initio QMD simulation of XANES spectra for the L3 Mo edge calculated in equilibrium. From [29]. . . . 33
2.11 Ab initio QMD simulation of XANES spectra for the L3 Mo edge calculated in the non-equilibrium situations, at solid density. From [38]. . . . 33
2.12 Evolution of x-ray absorption at selected energies. Experimental results are compared with calculations for different non-thermal lifetimes τ_{nt}. The experimental results are convoluted with the time resolution. From [50]. . . . 33
2.13 The fitting process to compare forward model and experimental data. From [51]. . . . 34
2.14 Results for an MCMC sampling of the likelihood function, using the "stretch move. An ensemble of 40 walkers and a total of 2500 ensemble steps were used. Initialization of the walker was done in a tight ball around the true value. . . . 38
2.15 Results for an MCMC sampling of the likelihood function, using the "stretch move. An ensemble of 40 walkers and a total of 2500 ensemble steps were used. . . . 38

3.1 The experimental setup. Marked IR is the 800 nm pump laser of variable intensity $\sim 10^{14}$ W/cm^2, while the XUV laser pulse is the probe pulse obtained through HHG, of much lower intensity and with a mean photon energy of 26.2 eV. The target being irradiated is a 100 nm thick Ti foil and the transmitted probe pulse is recorded with a CCD prepared for XUV radiation. 39
3.2 The HH spectrum. . . . 40
3.3 Images of the transmitted XUV radiation. Shots concerning a pump pulse with 150 μJ of pulse energy, at -125 fs of pump-probe delay. . . . 41
3.4 Images of the transmitted XUV radiation. Shots concerning a pump pulse with 150 μJ of pulse energy, at 425 fs of pump-probe delay. . . . 41
3.5 Images of the transmitted XUV radiation. Shots concerning a pump pulse with 500 μJ of pulse energy, at 200 fs of pump-probe delay. . . . 41
3.6 Line outs of a dark part of the CCD image, after subtracting figure the average background. Taken for all the images in a given time series. Yellow points are from before setting the average noise level to zero and blue points are from after. . . . 43
3.7 25×25 zoom in of XUV transmission images concerning a pump pulse with 150 μJ of pulse energy, at 425 fs of pump-probe delay. . . . 44
3.8 40×40 zoom in of XUV transmission images concerning a pump pulse with 500 μJ of pulse energy, at 200 fs of pump-probe delay. . . . 44

3.9 Masks of the zone of interest, obtained with a threshold method. Pixels set to one correspond to ablated regions, that went through a warm dense state while pixels set to zero correspond to regions that remained solid Ti. Based on the zoomed-in shots at $t = \infty$. 45

3.10 Images of the transmitted XUV radiation. Shots concerning a pump pulse with 1000 μJ of pulse energy, at 100 fs of pump-probe delay. 45

3.11 Correcting pumped shots for thermal emission, 150 μJ series at t=425 fs, by fitting expression 3.2 to the unpolluted XUV-only shot. 47

3.12 Correcting pumped shots for thermal emission, 1000 μJ series at t=100 fs, by fitting expression 3.3 to the unpolluted XUV-only shot. 47

3.13 Subdividing zone of interest, 150 μJ series at t=425 fs. 3 different zones are defined, after the center of the pulse is found, based on a fraction of the radii of the total zone of interest, defined in figure 3.9. 48

3.14 Subdividing zone of interest, 500 μJ series at t=200 fs. 3 different zones are defined, after the center of the pulse is found, based on a fraction of the radii of the total zone of interest, defined in figure 3.9. 49

3.15 Subdividing zone of interest, 1000 μJ series at t=100 fs. 3 different zones are defined, after the center of the pulse is found, based on a fraction of the radii of the total zone of interest, defined in figure 3.9. 49

3.16 Relative (to probe only) transmission, as a function of time, calculated for all the sub-zones of all the acquired series (with varying total pump energy). Data showed up to 1 ps pump-probe delay. Laser pulse peaks at 0 s. 51

3.17 Relative (to probe only) transmission, as a function of time, grouped by absorbed fluence of the respective sub-zone. Laser pulse peaks at 250 fs. Log scale. 52

4.1 A schematic representation of the pumping and probing process complete with the electronic distributions and the cold DOS of Ti. 56

4.2 Spectrum of the HHG pump pulse after going through a cold Ti film (red) and through the whole in the film (blue). 56

4.3 Integrand of equation 4.1, as a function of energy and its two components for $\varepsilon_t = 4$ eV. $(1 - f)$ was calculated from a TTM simulation. 57

4.4 2D correlations and marginalized posterior distribution of the free parameters of a physical forward model based on the TTM, with Lin-like coupling parameter (equation 2.17) and DOS as in equation 4.4. The estimations were performed with MCMC searches, over the free parameter space, with an ensemble of 40 walkers and a least squares likelihood function. The darker line on the 2D correlation is the 1σ band. 62

4.5 100 model runs with parameters sampled independently from the ensembles generated by the MCMC searches, for a physical forward model of a TTM, with Lin-like coupling parameter (equation 2.17) and DOS as in equation 4.4, plotted on top of the experimental data. In log scale with the laser fluence peaking at 100 fs. 63

4.6 100 model runs with parameters sampled independently from the ensemble generated by the MCMC search, considering all sub-zones, for a forward model comprised of a TTM with Lin-like coupling parameter and DOS as in equation 4.4, plotted on top of the experimental data. In log scale with the laser fluence peaking at 100 fs. 64

4.7 Temporally averaged G_{ei} vs maximum T_e, for each sub-zone considered. Central estimate and error bars obtain by sampling 100 model runs, from MCMC search results for a forward model comprised of a TTM with Lin-like coupling parameter and DOS as in equation 4.4. The light green line is Lin's result ([41]) for a cold Ti DOS and the dark blue line refers to calculations with the same formula but an Al (or FEG-like) DOS. In dark green the result of Rethfeld ([23]) for a FEG and in light blue the XTANT-3 code predictions for Ti [10]. 65

4.8 C_e simulated vs maximum T_e, for each sub-zone considered. Central estimate and error bars were obtained by sampling 100 model runs, from MCMC search results for a forward model comprised of a TTM with Lin-like coupling parameter and DOS as in equation 4.4. The light green line is Lin's result ([41]) for a cold Ti DOS and the dark blue line refers to calculations with the same formula but an Al (or FEG-like) DOS. The black dots are the heat capacity estimates from a finite temperature DFT simulation with a cold lattice. 65

4.9 Minimum XUV transmission vs maximum T_e, for each sub-zone considered. Central estimate and error bars were obtained by sampling 100 model runs, from MCMC search results for a forward model comprised of a TTM with Lin-like coupling parameter and DOS as in equation 4.4. The black dots are the optical response properties estimates from a finite temperature DFT simulation with a cold lattice. 66

4.10 2D correlations and marginalized posterior distribution of the free parameters of a physical forward model based on the TTM, with Lin-like coupling parameter (equation 2.17) and Ti DFT-calculated DOS. The estimations were performed with MCMC searches, over the free parameter space, with an ensemble of 40 walkers and a least squares likelihood function. The darker line on the 2D correlation is the 1σ band. 40000 total model evaluations were performed and the first 20000 were discarded. 67

4.11 50 model runs with parameters sampled independently from the ensemble generated by the MCMC search, for a physical forward model of a TTM, with Lin-like coupling parameter and TI DFT-calculated DOS, plotted on top of the experimental data. In log scale with the laser fluence peaking at 100 fs. 67

4.12 Temporally averaged G_{ei} vs maximum T_e, for each sub-zone considered. Central estimate and error bars obtain by sampling 100 model runs, from MCMC search results for a forward model comprised of a TTM with Lin-like coupling parameter and DFT calculated Ti DOS. The light green line is Lin's result ([41]) for a cold Ti DOS and the dark blue line refers to calculations with the same formula but an Al (or FEG-like) DOS. In dark green the result of Rethfeld ([23]) for a FEG and in light blue the XTANT-3 code predictions for Ti [10]. 68

4.13 C_e vs maximum T_e, for each sub-zone considered. Central estimate and error bars obtain by sampling 100 model runs, from MCMC search results for a forward model comprised of a TTM with Lin-like coupling parameter and DFT calculated Ti DOS. The light green line is Lin's result ([41]) for a cold Ti DOS and the dark blue line refers to calculations with the same formula but an Al (or FEG-like) DOS. Heat capacity estimates from a finite temperature DFT simulation with a cold lattice (black dots). 68

4.14 Minimum XUV transmission vs maximum T_e, for each sub-zone considered. Central estimate and error bars obtain by sampling 100 model runs, from MCMC search results for a forward model comprised of a TTM with Lin-like coupling parameter and DFT calculated Ti DOS. The black dots are the optical response properties estimates from a finite temperature DFT simulation with a cold lattice. 69

4.15 2D correlations and marginalized posterior distribution of the free parameters of a physical forward model based on the TTM, with constant G_{ei} and DOS as in equation 4.4. The estimations were performed with MCMC searches, over the free parameter space, with an ensemble of 40 walkers and a least squares likelihood function. The darker line on the 2D correlation is the 1σ band. 69

4.16 50 model runs with parameters sampled independently from the ensembles generated by the MCMC searches, for a physical forward model of a TTM, with constant G_{ei} and DOS as in equation 4.4, plotted on top of the experimental data. In log scale with the laser fluence peaking at 100 fs. 69

4.17 G_{ei} vs maximum T_e, for each sub-zone considered. Sample comprised of 100 model runs, from MCMC search results for a forward model comprised of a TTM with constant G_{ei} and DOS as in equation 4.4. The light green line is Lin's result ([41]) for a cold Ti DOS and the dark blue line refers to calculations with the same formula but an Al (or FEG-like) DOS. In dark green the result of Rethfeld ([23]) for a FEG and in light blue the XTANT-3 code predictions for Ti [10]. 71

4.18 C_e vs maximum T_e, for each sub-zone considered. Central estimate and error bars obtain by sampling 100 model runs, from MCMC search results for a forward model comprised of a TTM with constant G_{ei} and DOS as in equation 4.4. The light green line is Lin's result ([41]) for a cold Ti DOS and the dark blue line refers to calculations with the same formula but an Al (or FEG-like) DOS. The black dots are the heat capacity estimates from a finite temperature DFT simulation with a cold lattice. 71

4.19 Minimum XUV transmission vs maximum T_e, for each sub-zone considered. Central estimate and error bars obtain by sampling 100 model runs, from MCMC search results for a forward model comprised of a TTM with constant G_{ei} and DOS as in equation 4.4. The black dots are the optical response properties estimates from a finite temperature DFT simulation with a cold lattice. 72

4.20 $\sum_\ell \ell \cdot \int \left\langle J_l(\frac{eE_L \cdot \Delta k \cdot \mu}{m_{eff}\omega_L^2}) \right\rangle_\mu d\Delta k$ as a function of E_L, in black. $\int \left\langle J_l(\frac{eE_L \cdot \Delta k \cdot \mu}{m_{eff}\omega_L^2}) \right\rangle_\mu d\Delta k$ for select orders of the Bessel function in different colors. 77

4.21 Analytical solution of equation 2.9, without the phonon term, at different time steps, for $F = 3900$ J/m^2, $\kappa_{ee} = \kappa_{ie} = 1$ and $m_{eff} = m_e^0$. Here, as in the TTM section, laser intensity peaks at 100fs. The light blue line corresponds to a fit of a Fermi Dirac function to the obtained non-equilibrium $f(k,t)$. 78

4.22 Analytical solution of equation 2.9, without the phonon term, at 100 fs, for 3 different simulations run with $F = 3900$ J/m^2, $\kappa_{ee} = 1$, $m_{eff} = m_e^0$ and different κ_{ie}. Here, as in the TTM section, laser intensity peaks at 100fs. The light blue line corresponds to a fit of a Fermi Dirac function to the obtained non-equilibrium $f(k,t)$. 79

4.23 Analytical solution of equation 2.9, without the phonon term, at 100fs, for 3 different simulations run with $F = 3900$ J/m^2, $\kappa_{ie} = 1$, $m_{eff} = m_e^0$ and different κ_{ee}. Here, as in the TTM section, laser intensity peaks at 100fs. The light blue line corresponds to a fit of a Fermi Dirac function to the obtained non-equilibrium $f(k,t)$. 79

4.24 Analytical solution of equation 2.9, without the phonon term, at 100fs, for 3 different simulations run with $F = 3900$ J/m^2, $\kappa_{ie} = \kappa_{ee} = 1$, and different $_{eff}$. Here, as in the TTM section, laser intensity peaks at 50 fs. The light blue line corresponds to a fit of a Fermi Dirac function to the obtained non-equilibrium $f(k,t)$. 80

4.25 2D correlations and marginalized posterior distributions of the free parameters of a physical forward model based on the Boltzmann equation 2.9, without the phonon term. Estimated via MCMC search, with an ensemble of 40 walkers, evolved for a total of 15000 model evaluations. 10000 evaluations discarded as burn-in. Family of 150 μJ data series utilized. The darker line on the 2D correlation is the 1σ band. 81

4.26 50 model runs with parameters sampled independently from the ensemble generated by the MCMC search, for a physical forward model of the Boltzmann equation 2.9, without the phonon term, plotted on top of the experimental data. In log scale with the laser fluence peaking at 100 fs. 81

4.27 C_e vs maximum T_e, for each sub-zone considered, calculated from equation 4.6. Central estimate and error bars obtain by sampling 50 model runs, from MCMC search results for a physical forward model of the Boltzmann equation 2.9. The light green line is Lin's result ([41]) for a cold Ti DOS and the dark blue line refers to calculations with the same formula but an Al (or FEG-like) DOS. The black dots are the heat capacity estimates from a finite temperature DFT simulation with a cold lattice. 82

4.28 Minimum XUV transmission vs maximum T_e, for each sub-zone considered. Central estimate and error bars obtain by sampling 50 model runs, from MCMC search results for a physical forward model of the Boltzmann equation 2.9. The black dots are the optical response properties estimates from a finite temperature DFT simulation with a cold lattice. 82

4.29 Average e-e collision rates calculated from equation 4.16, as a function of T_e, for 50 different model runs. Each continuous line corresponds to results of a model run. 83

4.30 Average e-e collision rates calculated from equation 4.16, as a function of T_e, for 50 different model runs. Each continuous line corresponds to the results of a model run. 83

4.31 Chemical potential $\mu/k_B T_e$ as a function of the degeneracy parameter calculated form equation 1.5, for the maximal T_e of the sub-zone in question. Central estimate and error bars obtain by sampling 50 model runs, from MCMC search results for a physical forward model of the Boltzmann equation 2.9. The blue line corresponds to the interpolating fit between the two degeneracy regimes shown in figure 1.2. 84

4.32 Plasma parameter $\Gamma = d/l$ (section 1.2.2), as a function of maximal T_e of the sub-zone in question. Central estimate and error bars obtain by sampling 50 model runs, from MCMC search results for a physical forward model of the Boltzmann equation 2.9. 84

4.33 δ_s as a function of T_e calculated by inversion of the absorbed energy calculation for each sub-zone. Central estimate and error bars obtain by sampling 50 model runs, from MCMC search results for a a physical forward model of the Boltzmann equation 2.9. The blue line corresponds to the interpolating fit between the two degeneracy regimes shown in figure 1.2. The dark green line the [56] measurement. 84

4.34 2D correlations and marginalized posterior distributions of the free parameters of a physical forward model based on the Boltzmann equation 2.9, without the phonon term. Estimated via 3 different MCMC searches, with an ensemble of 40 walkers, evolved for a total of 15000 model evaluations and 20000 evaluations discarded as burn-in. Family of 150 μJ data series utilized. The darker line on the 2D correlation is the 1σ band. 85

4.35 50 model runs with parameters sampled independently from the ensembles generated by the MCMC searches, for a physical forward model of the Boltzmann equation 2.9, without the phonon term, plotted on top of the experimental data. In log scale with the laser fluence peaking at 100 fs. 85

A.1 Marginalized posterior distributions of MCMC searches performed for a physical forward model of a TTM, with constant G_{ei} and DOS as in equation 4.4. Ensemble of 40 walkers. The darker line on the 2D correlation is the 1σ band. 95

Chapter 1

Introduction

Warm Dense Matter (WDM) states are characterized by temperatures ranging from 0.1 to 100 eV and close to solid-state densities (0.1 to 10 times ρ_{solid}). Having thermal and Fermi energies close to one another, these states of matter are placed in between the quantum regime of strong degeneracy and the classical regime of non-degeneracy. Atomic or ionic binding energies also close to the average thermal energy makes WDM states sit in the transition between solid, liquid gas and plasma [1].

This chapter describes the motivations for the study of Warm Dense Matter, in terms of its applications in technological fields and as states of inherent theoretical interest. It ends with a brief overview of the current methods for creating WDM states in a laboratory and a review of the fundamental physical processes that take place under isochoric heating (IH).

1.1 Applications

The interest in the WDM field was been fueled, in recent years, by its broad applications. WDM is created in Inertial Confinement Fusion (ICF) experiments - when a driving laser heats up and compresses a solid fuel target - and is present in astrophysical objects such as gas giants, brown and white dwarfs and low-mass stars. It is also created in intense laser-matter interactions, common in material processing techniques.

Inertial Confinement Fusion

ICF works, in theory, by igniting a target (starting a fusion reaction) and extracting energy from it. There are different types of ICF, requiring different targets specifically optimized to absorb the driving energy that can take multiple forms. They will, however, always include a fuel capsule (most likely spherical and made of Deuterium and Tritium) and an ablator surrounding it. To reach ignition, energy must be provided to the ablator by the driver, which is usually a laser. The ablator will heat considerably and high-velocity ablated material will be propelled away, while, in reaction, the fuel capsule will be pushed inwards. [2]

In direct drive ignition, irradiation of the target causes the energy from the driver to couple directly to electrons of the ablator material. These subsequently equilibrate with the ions, heating the atomic lattice

enough to remove the ablator coating and turn it into a coronal plasma [1]. The electron-electron (e-e) and electron-ion (e-i) coupling coefficients, or equilibration rates, will determine laser energy absorption, transport properties and ablation rate, along with the mass and temperature of the coronal plasma. These equilibration rates are, then, vital for both simulation and target design in ICF experiments [2].

The compressed fuel will move rapidly through the phase diagram, transversing WDM conditions before exceeding them. Knowledge of the equation of state in this regime is of vital importance for the proper understating of the processes leading to ignition of the capsule.[1]

Astrophysical Objects

Some layers of the interior of giant planets like Jupiter and Saturn are WDM. These states of matter can also be found in brown and white dwarfs, low-mass stars, and the hot metallic core of terrestrial planets. Much of the early WDM research has been and is driven by geophysics and planetary sciences. The possibility of studying astrophysical conditions such as WDM states in a laboratory has, relatively recently, given birth to the field of laboratory astrophysics [3]. The discovery of a large number of exoplanets has expanded the conditions and materials where WDM states can be observed in the universe and, as such, has fueled the need for further investigation into this topic [4] [5].

Elucidation on the properties of WDM, such as the equation of state of compressed hydrogen, has great implications for the determination of the size and thermodynamical state of the core of Jupiter and other gas giants. The number of layers in the planetary interior, the phase state transitions happening in the boundary between these layers (possibly including de-mixing of hydrogen and helium or the transition of hydrogen to a metallic phase), the mass-radius relation and formation process of gas giants, and the nature of the planetary dynamo and the magnetic field it generates are all open questions also requiring further knowledge of WDM conditions. [4]. The X-ray opacity of WDM states is also of great consequence as much of the energy transport within stars and other hot astrophysical objects is done by radiation [3].

Material processing

Femtosecond laser technology provides many practical applications for material modification, including the promising technique of laser ablation that enables precise micro and nano machining [6]. In biology and medicine, ultrafast lasers have also led to considerable advances, including precise biological tissue manipulation, with possible surgical applications [7].

In laser ablation techniques sub-picosecond pulses have two distinct advantages when compared with longer pulses: they require lower fluences for ablation to occur (the intensity delivered in the focal spot will still be very high) and they produce considerably sharper contours, which can be seen in figure 1.1. This last effect is possible due to the unique energy delivery system that couples the energy to the electrons. After the pulse stops, the ionic temperature can quickly rise above the critical one and ejection of the material will follow, allowing for the removal of most of the absorbed laser energy as well. Very little collateral damage might be expected then since there is not much thermal energy to be dissipated through the bulk of the material [8].

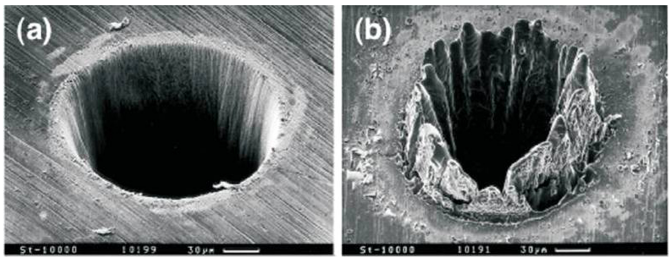

Figure 1.1: SEM micrographs of holes drilled in 100-μm-thick steel foils by ablation using laser pulses with the following parameters: (a) pulse duration (τ_p): 200 fs, pulse energy: 120 mJ, fluence (F): 0.5 J/cm^2, $\lambda =$ 780 nm; and (b) τ_p =3.3 ns, pulse energy: 1 mJ, F = 4.2 J/cm^2, $\lambda =$ 780 nm. The scale bars represent 30 μm. Integrally taken from [9].

Despite these advantages, many fundamental aspects of material response to femtosecond irradiation remain poorly understood. The electronic population directly excited by the laser achieves a non-equilibrium temperature high above the ionic one. This induces a variety of effects, including energy exchange between electrons and ions, modification of the inter-atomic potential, evolution of material properties, phase transitions, etc. [10]. Proper parameterization of WDM models is then crucial to understand how these non-equilibrium transient states affect the outcomes of the technological processes previously mentioned.

1.2 WDM: In the crossroads between plasma and condensed matter

WDM sits between cold solids and classical plasma conditions both because of the strongly correlated nature of the ions and quantum nature of the electrons and of the high temperatures it exists in. The interplay of these factors makes it so that WDM states can exist between the degenerate and non-degenerate regimes. The goal of this section will be to provide an elementary description of the (semi) degenerate and strongly correlated nature of these states, with the discussion mainly based on [11], unless otherwise mentioned.

1.2.1 Equilibrium distribution function: degeneracy

For rarefied plasmas, whose constituent particles can be treated classically, (non-degenerate plasmas) equilibrium momentum distribution function of species a is given by the Boltzmann distribution:

$$f_a(p) = e^{-(1/k_B T)(p^2/2m_a - \mu_a)} \tag{1.1}$$

where k_B is the Boltzmann constant, μ_a is the chemical potential and T is the temperature. Furthermore, the chemical potential can be written, with the help of the usual constraints on the number of particles, as [11]:

$$\mu_a = k_B T \ln \frac{n_a \Lambda^3}{2s_a + 1} \text{ and } \Lambda_a = \sqrt{\frac{2\pi\hbar}{m_a k_B T}} \tag{1.2}$$

where Λ_a is the thermal wavelength, s_a is the spin and n_a is the number density of species a.

If the plasma is dense, however, we cannot neglect the quantum nature of its constituent particles. From this new starting point, the state of a particle with momentum $\mathbf{p}$ is characterized by a wave function $\Psi_{\mathbf{p}}(\mathbf{r})$,

rather than a classical trajectory. The probability density of finding a particle with momentum $\mathbf{p}$ and position $\mathbf{r}$ is then given by: $d\omega(\mathbf{p},\mathbf{r}) = |\Psi_{\mathbf{p}}(\mathbf{r})|^2 d\mathbf{r}$. In equilibrium conditions, the spatial width of the most likely region for the electron is roughly given by Λ_a. The mean particle distance, on the other hand, can be written as $d_a \propto 1/\sqrt[3]{n_a}$. For dense plasmas, such as solid density ones, the inter-atomic distance may be of the order of the thermal length, i.e $n_a\Lambda_a \approx 1$. In this case, the indistinguishability of the plasma particles has to be taken into account (degenerate plasmas) and, as such, the spin-statistics theorem will govern their behavior. Their momentum distribution will now be dependent on their spin:

$$f_a(\mathbf{p}) = \frac{1}{e^{(1/k_B T)(p^2/2m_a - \mu_a)} \pm 1} \tag{1.3}$$

with the $+$ sign for fermionic species and the $-$ sign for bosonic ones. This difference in sign is more important for low temperatures: for fermionic systems, the distribution leads to an uppermost occupied state, called the Fermi level; while for bosonic systems it leads to the bunching of particles in the lowest energy state.

The boundary between degenerate and non-degenerate plasmas is, then, roughly given by:

$$n_a\Lambda_a^3 = n_a \left(\frac{h}{\sqrt{2\pi m_a k_B T}} \right)^3 = 1 \tag{1.4}$$

with the strongly-degenerate result recovered for $n_a\Lambda_a^3 \gg 1$ and the non-degenerate one recovered for $n_a\Lambda_a^3 \ll 1$, for which both equations in expression 1.3 reduce to their common limit, expression 1.2.

Closely related to this discussion and to equation 1.4 is the Θ parameter, defined specifically for fermionic systems, as the ratio between electronic temperature and the Fermi temperature (T_F) [3]:

$$\Theta = \frac{T_e}{T_F} = T_e \left[\left(\frac{8\pi}{3n_e} \right)^{2/3} \frac{2m_e k_B}{h^2} \right] \tag{1.5}$$

where $T_F = \epsilon_f / k_B$ and ϵ_f is the energy of the uppermost occupied states, i.e., the Fermi energy. The boundary between the plasma regimes being discussed is also at $\Theta \approx 1$.

With the knowledge of the distribution of the species, all thermodynamical properties of degenerate plasmas can be determined [11]. To fully characterize an equilibrium situation one needs to calculate the chemical potential μ, which is the generalization of the Fermi temperatures for non-zero temperatures. Thermodynamically, it is the variation of the internal energy required to add a particle to a given ensemble of particles, at constant entropy and volume. For non-degenerate systems μ will be negative: a new particle can be added with zero energy but the energy of the system must decrease to keep entropy constant; while for a strongly degenerate fermionic system it will be positive: to respect Pauli's exclusion principle a particle enters an unoccupied state (whose energy is above zero), thus increasing the internal energy [3].

This important quantity, which controls the number of particles in the Grand Canonical Ensemble, can be calculated by inversion of the number of particles constraint, mentioned earlier, as:

$$n_a = \frac{2s_a + 1}{\Lambda_a^3} I_{1/2}(x_a) \text{ with } I_\nu(x) = \frac{1}{\Gamma(\nu+1)} \int_0^\infty dt \frac{t^\nu}{e^{t-x}+1} \tag{1.6}$$

with the family of integrals $I_\nu(x)$ being referred to as the Fermi integrals and $x = \mu/k_B T$ the dimensionless chemical potential. The condition states that the integral of the distribution function integrated over all phase space needs to correspond to the number density of the ensemble of particles. Well-known analytical expressions for μ_a exist for the limiting cases of strong degeneracy and non-degeneracy, however, near the boundary defined by equation 1.4, the required integrals have to be computed numerically. In figure 1.2 one can see the limiting cases as well as a bold line, with the full calculation performed computationally.

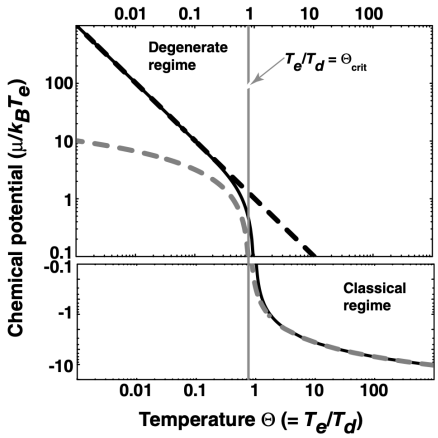

Figure 1.2: Chemical potential μ as a function of Θ. From [3].

1.2.2 Screening in Coulomb plasmas

An important phenomenon in plasma is the screening of the potential of an electric charge. To discuss this phenomenon a point-like charge (e_0) is introduced, moving with velocity $\mathbf{v}_0$ through the plasma. Such a particle will change its surrounding medium by creating an induced charged density. Another charged particle, at position $\mathbf{r}$, will feel both the test charge and the induced charged density. The potential at $\mathbf{r}$ results from these two different contributions and can be named $\Phi^{\text{eff}}(\mathbf{r}, t)$. Under the electrostatic approximation (for non-relativistic plasmas) the particles interact with each other via the binary Coulomb potential and one can write, for species a:

$$\Phi^{\text{eff}}(\mathbf{r}, t) = \Phi^{\text{ext}}(\mathbf{r}, t) + \sum_b \int d\mathbf{r}' \frac{e_a e_b}{\mathbf{r} - \mathbf{r}'} \int \frac{d\mathbf{p}}{(2\pi\hbar)^3} f_b(\mathbf{p},\mathbf{r},\mathbf{t}) \tag{1.7}$$

with the e_a and e_b the electric charges of the respective plasma species and Φ^{ext} the potential induced by the moving point-like charge. In the case of non-external perturbation, this potential will add to zero due to charge neutrality.

Determining the time evolution of the distribution function $f_b(\mathbf{p},\mathbf{r},\mathbf{t})$) requires the well known Boltzmann equation, if we wish to consider non-equilibrium situations:

$$\frac{\partial f_a}{\partial t} + \frac{\mathbf{p}}{m} \cdot \frac{\partial f_a}{\partial \mathbf{r}} + \mathbf{F} \cdot \frac{\partial f_a}{\partial \mathbf{p}} = \left(\frac{\partial f_a}{\partial t}\right)_{\text{coll}} \tag{1.8}$$

where on the right-hand side, beside the temporal derivative, there is the diffusion term and the force term, with $\mathbf{F}$ the external force the system is subject to. The collision term on the left-hand side describes the details

of the two-, three- and many-body collisions that can take place.

Taking the right-hand side to zero, the Vlasov equation is obtained, which describes most collective phenomena in plasmas. Furthermore, for non-relativistic plasmas, the force term can be reduced to the electrostatic approximation and it is possible to write:

$$\left[\frac{\partial}{\partial t}+\frac{\mathbf{p}}{ma}\cdot\frac{\partial}{\partial \mathbf{r}}-\frac{\partial}{\partial \mathbf{r}}\Phi^{\text{eff}}\left(\mathbf{r},t\right)\cdot\frac{\partial}{\partial \mathbf{p}}\right]f_a\left(\mathbf{p},\mathbf{r},t\right)=0 \tag{1.9}$$

with Φ^{eff} described by expression 1.7. Splitting the distribution function into an equilibrium component plus a perturbation ($f_a\left(\mathbf{p},\mathbf{r},t\right)=f_a^0(p)+\delta f_a\left(\mathbf{p},\mathbf{r},t\right)$), which is assumed small, allows equation 1.9 to be linearized. After a subsequent Fourier Transform the solution can be written as:

$$\delta f_a(\mathbf{p},\mathbf{r},t)=\frac{e_a}{\mathbf{k}\cdot\frac{\mathbf{p}}{m_a}-\omega-i\epsilon}\mathbf{k}\delta\Phi^{\text{eff}}\left(\mathbf{k},\omega\right)\cdot\frac{\partial f_a^0\left(p\right)}{\partial \mathbf{p}} \tag{1.10}$$

with ϵ term arising from the usual adiabatic switching scheme for proper pole integration.

Finally, equation 1.10 can be introduced in the Fourier transformed version of equation 1.7 to obtain:

$$\Phi^{\text{eff}}(\boldsymbol{k},\omega)=\frac{\Phi^{\text{ext}}(\boldsymbol{k},\omega)}{1-\sum_d\frac{e_d^2}{k^2}\int\frac{d\boldsymbol{p}}{(2\pi\hbar)^3}\frac{\mathbf{k}\cdot\partial f_c^0/\partial \boldsymbol{p}}{\left(\boldsymbol{k}\cdot\frac{\boldsymbol{p}}{m_c}-\omega-i\epsilon\right)}}=\frac{\Phi^{\text{ext}}(\boldsymbol{k},\omega)}{\varepsilon(\mathbf{k},\omega)} \tag{1.11}$$

with $\varepsilon(\mathbf{k},\omega)$ defined as the retarded response function of the medium, i.e the dielectric function and $\Phi^{\text{ext}}(\boldsymbol{k},\omega)=\Phi^{\text{eff}}(\mathbf{r},t)$ can be determined by the Fourier transformed Poisson equation which, enables us to write the potential as the sum of the test particle contribution, with the usual form: $\Phi^{test}(\boldsymbol{k},\omega)=(4\pi/k^2)e_0\delta(\omega-\mathbf{k}\cdot\mathbf{v}_0)$.

If v_0 is much smaller than the typical thermal velocity of the plasma constituents, they can be said to follow any oscillation of the potential instantly. The statistic limit of the dielectric function $\varepsilon(\mathbf{k},0)$ (instantaneous response function), corresponding to the charge being immobile, $\mathbf{v}_0=0$, is then sufficient to describe this interaction. From the above result:

$$\varepsilon(\boldsymbol{k},0)=1+\sum_d\frac{4\pi e_d^2}{k^2}\int\frac{dp}{(2\pi\hbar)^3}\frac{\partial}{\partial\left(\frac{p^2}{2m}\right)}f_d\left(\frac{p^2}{2m}-\mu_c\right)=1+\sum_d\frac{4\pi e_d^2}{k^2k_BT}\frac{d}{d\left(\mu_d/k_BT\right)}n_d\left(\mu_d\right) \tag{1.12}$$

where $n_d(\mu_d)$ is the number density of species d. These relations are both valid for arbitrary degeneracy as they do not assume a form of the distribution function. To make the physical meaning of the function clear it can be rewritten as:

$$\varepsilon(\mathbf{k},0)=1+\frac{1}{k^2r_0^2}\text{ , where }r_0^{-2}=\frac{4\pi\sum_c e_c^2}{k_BT}\frac{\partial n_c}{\partial\left(\beta\mu_c\right)}. \tag{1.13}$$

where r_0 is then a distance (and κ the inverse of said distance) and can be interpreted as the screening radius, as can be seen by the resulting effective potential:

$$\Phi^{\text{eff}}(\mathbf{k},0)=\frac{e_0}{k^2+\kappa^2}\longrightarrow\Phi^{\text{eff}}(r)=\frac{e_0}{r}\exp(-r/r_0). \tag{1.14}$$

The expression above makes clear that the long-range nature of the Coulomb potential of the point charge is suppressed by the polarized plasma particles, in a phenomenon called screening or shielding. The potential mediating the interaction between two constituent plasma particles is the Coulomb one, up to a radius of $\approx r_0$ and decays exponentially for larger radii.

Valuable physical insight is hidden, as usual, in the limiting cases. By rewriting equation 1.13 in terms of its Fermi integrals and setting $n_a\Lambda_a^3 \ll 1$, i.e. in the non-degenerate regime, the well-known Debye screening length is obtained:

$$r_0 = r_D = \left(\frac{4\pi}{k_B T} \sum_c n_c e_c^2 \right)^{-1/2} . \tag{1.15}$$

In the strongly degenerate regime where $n_a\Lambda_a^3 \gg 1$, on the other hand, the Thomas-Fermi screening length is recovered:

$$r_0 = r_{TF} = \left(\sum_c \frac{6\pi e_c^2 n_c}{\varepsilon_c^F} \right)^{-1/2} . \tag{1.16}$$

Electrons in metals at room temperature, for example, are subject to Thomas-Fermi screening, which is very pronounced since $r_{TF} \sim 10^{-10}$ m.

To uncover the temperature-density boundary between the two regimes we turn to more ad hoc arguments. To have a strongly correlated, i.e., non-ideal plasma, the condition $\langle E_{pot} \rangle \geq \langle E_{kin} \rangle$ needs to be met. In this regime, the particles stop being nearly free and "feel" the Coulomb potential in a more significant way: bound states appear and the dispersion relation of the particles is modified. Introducing the characteristic length l_{ab} as the distance between a particle of species a and one of species b for which the Coulomb interaction is of the order of the mean kinetic energy, in the case of a non-degenerate plasma, we can estimate $E_{kin} \approx k_B T$ such that $k_B T = |e_a e_b / l_{ab}|$. This can be generalized for arbitrary degeneracy with the appropriate Fermi integrals. Further defining the mean particle distance as $d_a = (3/4\pi n_a)^{1/3}$ the potential and kinetic energies can be compared through $\Gamma_{ab} = l_{ab}/d$, where strong correlations are expected if $\Gamma \leq 1$. Ideal gas behavior, on the other hand, is expected if $\Gamma \ll 1$, such that the kinetic energy is much stronger than potential energy, making free particle scattering the dominant interaction.

1.3 The Temperature - Density Plane

Having defined, in the previous section, the parameters of interest to characterize non-ideal plasmas, namely Θ and Γ, we can now define the Warm Dense region in a phase space diagram. We expect quantum effects to dominate, namely strong correlations and degeneracy effects, where $\Gamma > 1$ and $n_e\Lambda_e > 1$. These boundaries push our regime to the hotter and denser side of the diagram. At high enough densities, however, full ionization will take place and the quantum correlations lose importance. This places an upper bound to our regime at the line $r_s = 1$, with r_s called the Brueckner parameter, and being the ratio between the mean particle distance and the Bohr radius.

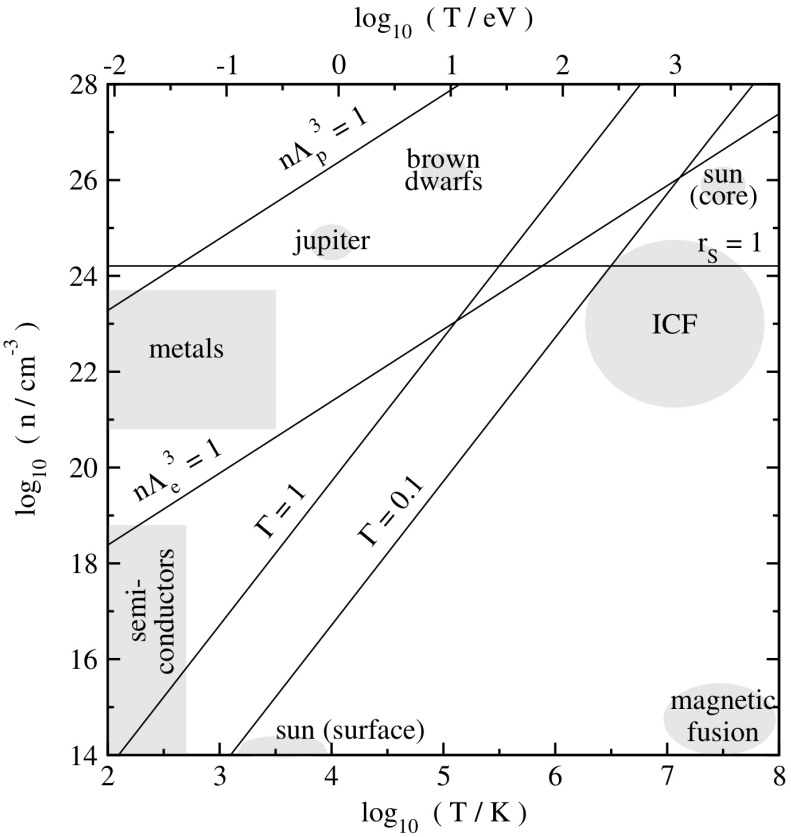

Figure 1.3: Temperature-density plane with several adimensional parameters plotted, for the equilibrium case, along with demarcations of different zones of physical and technological interest. From [11].

1.4 Creating WDM states in the lab

Several methods can be used to achieve WDM conditions in the laboratory, among them static and dynamic compression and isochoric heating. All try to solve the experimental difficulties in creating a large enough sample with uniform conditions that arise either because the compression or the heating process necessarily create temporal and spatial gradients in the temperature and/or density profiles [5]. The degenerate plasma that is created from these methods is typically a Coulomb plasma with its constituent particles being electrons and ions. Table 1.1 presents an overview of some of the most commonly used sources to produce warm dense conditions. They will be expanded upon through the remainder of this section.

Source	Equilibrium	Heating depth	Steady Conditions	$\Delta T_e^{\max}$	Density
fs laser	✗	(10-100) nm	10's ps	keV	$\sim \rho_{\text{solid}}$
ns laser (Dynamic Comp)	∼	(10-100) μm	ns	keV	$1000 \cdot \rho_{\text{solid}}$
Diamond Cell (Static Comp)	✓	—	∞	<1 eV	$10 \cdot \rho_{\text{solid}}$
X-rays	✗	(10-100) μm	10's ps	100's eV	$\sim \rho_{\text{solid}}$
Protons	✗	(10-100) μm	10's ps	10's eV	$\sim \rho_{\text{solid}}$

Table 1.1: Table summary of the methods used to create warm dense matter.

Static compression relies on mechanical pressure induced by a diamond cell while dynamical compression

usually takes advantage of direct high-intensity irradiation of the sample with nanosecond lasers. The latter and more commonly used method is based on the density shock wave created (due to ablation) propagating to the bulk of the material [5]. It uses nanosecond ablation modes that take place after equilibration between the electronic and ionic populations. Both of these processes are not well suited for the study of non-equilibrium states, as they rely on density changes which, even for shorter pulses, would be on ionic (10's of picoseconds) time scales.

Isochoric heating (IH) of thin films creates states of solid density but higher electronic temperatures, in which only transverse spatial temperature gradients exist and the sample can be said to be at a single temperature in all its width: idealized slab approach [12]. Different types of sources that drive the energy into the sample result in different initial out-of-equilibrium states in which only the electronic or the ionic population is perturbed. They will equilibrate afterward, on a time scale bigger than the energy deposition process.

IH can be achieved with X-ray sources or proton beams than penetrate inside solid density material beyond the skin depth, depositing their energy in μm, length scales before significant hydrodynamic expansion kicks in [13]. The expansion process is expected to happen at roughly the speed of sound ($c_s \approx 10^4$ m/s for metals) which can be easily converted to expansion timescales in the tens of ps to tens of ns, for targets of thickness between 100 nm and 1mm, respectively [5]. Until the advent of Free Electron Lasers (FEL), with their combined ultra-short pulse duration (tens of femtoseconds) and high intensities, X-ray pulse duration only allowed for the study of states where electronic and ionic temperatures were already the same. Now, this emerging technology has renewed interest in the non-equilibrium properties of WDM states, with the possibility of additional insight into the optical and transport properties in this regime, such as the transparency of WDM Al to XUV due to fast electronic occupation of excited states [14, 15]. FELs, however, are limited in access and beam time due to high construction and operational costs.

Optical lasers also present an opportunity to create IH states in non-equilibrium setups, but only in the skin-depth layer, with a typical scale of tens of nm, for metals. As such the need for thinner samples arises to achieve idealized slab conditions of constant density and minimal transverse T_e gradients. The method is still constrained by the expansion times of the foil, which are on the lower end for thinner foils. This approach has the distinct advantage of being widely accessible when compared to FEL isochoric heating experiments, while still allowing access to non-equilibrium states of WDM of well-defined density if benchmarked against compression approaches.

In this thesis, our focus will be on the transient, warm dense, non-equilibrium states created by isochorically heating metals with femtosecond laser pulses. For the conditions stated above a simple mental picture can approximate the process: the energy being isochorically deposited in the electronic population within hundreds of fs which then equilibrates with the ions in tens of ps, that is, before they have time to move significantly thus maintaining solid/liquid density levels. Note that after significant expansion takes place, the warm dense state reverts to a classical plasma which is no longer in the purview of this thesis. We will focus on states with well-defined densities, only lightly touching upon different expansion and ablation mechanisms.

1.5 IH: Physical processes

A quick overview of the fundamental physical processes going on during and after excitation of a thin metal sample by an ultra-fast, tabletop, optical laser is now in order. Early theoretical frameworks for the absorption and relaxation of energy in the sample will be touched on.

1.5.1 Absorption of Energy

The energy from the femtosecond laser pulses is deposited in a solid by one of the following mechanisms [16]:

- intra-band absorption by the free charge carriers in the conduction band - this is a 3-body process (to first order), known as Inverse Bremsstrahlung (IB), where a phonon or ion is also required to participate to conserve overall crystal momentum;
- inter-band transitions - direct gap transitions as a first-order contribution and indirect ones (where again a phonon is required) appearing as a second-order contribution to the cross-section;
- absorption by collective excitations;
- absorption due to impurities and defects;
- ionization of core electrons.

The extent to which each of these contributes to the overall absorption cross section depends on some fundamental laser parameters including laser wavelength λ_L; laser frequency $\omega_L = 2\pi c/\lambda$; energy per pulse E_p; pulse duration τ_L; and focal spot area S_f. From these, we can also derive the average intensity $I = E_p/S_f \cdot \tau_L$, measured in W/cm^2, and the fluence $F = E_p/S_f$, measured in J/m^2. For femtosecond infrared pulses with intensities up to $I \approx 10^{14}$ W/cm^2 ($F \approx 5 \times 10^4$ J/m^2), and in the case of metal samples that have conduction band electrons free to partake in the IB, the sheer number of available photons quickly saturates the inter-band channel of absorption, making intra-band absorption the dominant process. Direct absorption by phonons does not play a significant role as the pulse duration is much shorter than their period. Ionization effects are still expected to provide a small contribution since, under IH conditions, the density never surpasses solid ones and so r_s remains below one.

In the Drude picture, nearly free electrons move in the conduction band due to the laser field, while e-i collisions, with a frequency ν_{e-i}, dampen their movement. Since IB is an intra-band phenomenon, the average energy increase is correctly described by this picture [17].

To obtain the Drude dielectric function for metals, a classical equation of motion for the free electron displacement needs to be written. Besides the electron acceleration term under the driving electric field, a frictional damping force of the medium is also present. Naturally, no restoration force is present if electrons are considered free. Using the equation of motion, the polarization vector can be determined if a linear response of the medium is assumed. This is justified, as the peak electric fields of interest to this work are well below the non-resonant non-linearity threshold (roughly where the driving electric field matches the one binding the

electron to the nucleus) and no fine tunning to achieve resonant non-linearities will be performed. By solving for the electronic displacement and assuming a direct proportionality to the polarization vector, it is possible to write the latter. Since the polarization is, by definition, the response of the medium to the electromagnetic (E-M) field, it is closely related to ε, such that we can write [18]:

$$\varepsilon(\omega) = \varepsilon_0 \left(1 - \left(\frac{\omega_p}{\omega}\right)^2 \frac{1}{1 - i\nu_{e-i}/\omega}\right) \tag{1.17}$$

with ε_0 the vacuum permittivity and $\omega_p = \sqrt{n_e e^2/m_e \epsilon_0}$ the plasma frequency. From equation 1.17, the behavior of the electric field propagating inside the medium can be extracted. Defining the complex refractive index as $\tilde{n} = \sqrt{\epsilon(\omega)} = n + ik$ and assuming the electric field is a plane wave propagating in the z-direction according to Maxwell's equations, inside the material we will have [18]:

$$E(z,t) = E_0 \cdot \exp\left(i\left(kz - \omega t\right)\right) = E_0 \cdot \exp\left(i\left(\tilde{n}\frac{\omega}{c}z - \omega t\right)\right) \tag{1.18}$$

with E_0 the electric field magnitude at the boundary of the material and k the wave-vector of light. As a limiting case, one can study the system with friction turned off, i.e., $\nu_{e-i} = 0$. In these conditions, the Drude term in equation 1.17 disappears if $\omega \gg \omega_P$, making the free electron medium transparent to high-frequency radiation, and the same term becomes strongly negative if $\omega \ll \omega_p$, making $\tilde{n}$ an imaginary number which, in turn, by equation 1.18, makes the electric field decay exponentially, in what is known as the skin effect. The critical frequency at which the system transitions from reflective to transparent is ω_p.

In the general case, from the definitions introduced above, the skin depth δ_s can be defined as the characteristic decay length of the electric field inside the material and write $\delta_s = c/\omega k$. For metals at room temperature and optical wavelength radiation, δ_s typically falls in the 10-60 nm range, or hundreds of atomic layers [19]. The fact that this distance is much smaller than the typical focal spot of the driving laser, tens of micrometers, generally justifies a 1-dimensional approximation (semi-infinite plane with a given thickness).

Still within the purview of linear response, the absorbed power density (energy absorbed per unit time and unit volume) is considered proportional to the photon flux, i.e., pulse intensity, which itself will decay exponentially in the direction of propagation. This results in the Lambert-Beer law of exponential decay with an attenuation coefficient equal to $2/\delta_s$. Also considering the Fresnel formula for absorption at a boundary, the absorbed energy density rate per unit time is then given by [17]:

$$Q_{abs}(x,r,t) = \frac{2}{\delta_s} A I(t,r) \exp(-2x/\delta_s) \text{ and } A = 1 - \frac{|n-1|^2}{|n+1|^2}. \tag{1.19}$$

Several caveats apply to this overly simplistic picture. Note that, during and after the pulse variations, the material parameter ν_{e-i} can change, as the e-e population thermalizes. It is known that electron-phonon or e-i collision rates are temperature-dependent, even in equilibrium conditions. In the limit of a cold solid, below the Fermi temperature, the electrons are degenerate and so the collision frequency only depends on ionic temperature and only by proxy on electronic temperature, $T_e = T_i$. In the fully ionized plasma limit, dominated by Coulomb collisions, the collision frequency decreases with the increase in electronic temperature,

as expressed by Spitzer's formula [20]. In figure 1.4, the collision frequency for Aluminium (Al) was plotted, for different temperatures of equilibrated electron and ion populations, by a harmonic mean interpolation between the behaviors in known regimes [21]. The dashed line imposes the physical constraint that the electron's mean free path is not smaller than the ion radius. Depending on the metal, the overall free electron density might also change during the pulse (through lowering the continuum and ionizing some bound states), also affecting the collision frequency.

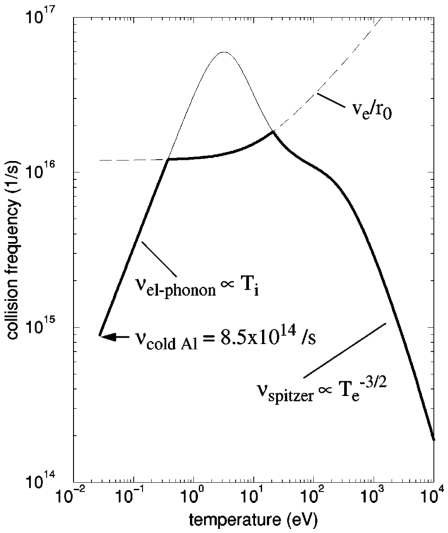

Figure 1.4: Electron-ion collision frequency for solid Al, interpolated between known regimes, with resource to a harmonic mean. The dashed line represents the plausible requirement that the electron's mean free path is bigger than the ion radius. From [22].

Inter-band absorption phenomena were also not part of the above calculation. Metals with valence *d* band electrons, more localized in energy than the *s* and *p*, close in energy to their "freer" *s* and *p* bands, for example, give rise to a complicated array of possible optical transitions, for sufficiently energetic photons. More sophisticated analytical models may be applied, with the inclusion of, for example, Lorentz-like discrete oscillator terms in the dielectric function at the expense of the inclusion of significantly more phenomenological parameters.

Finally, the ultra-fast excitation electrons are subject to puts into question the very notion of temperature, as it was discussed for electrons and ios in equilibrium. The initial (after absorption) non-thermal distribution of electrons can itself affect the band structure which would be reflected both in the intra-band contribution (for example through the electron effective mass) and the inter-band one.

1.5.2 Relaxation processes

After the pulse energy is initially deposited in the electrons, it will gradually start being shared by the electron and ion populations. Electron-electron collision rates, at WDM temperatures, are roughly $\nu_{e-e} \approx 10^{16}$ Hz $\approx \omega_p$ and, as such, e-e energy exchange rates are on the order of 0.1 fs. Even if several collisions are necessary to obtain e-e equilibrium, it should still be achieved on the order of the pulse duration length $\tau_p \approx 50$ fs. This can be seen in [23] where Boltzmann equations for two fluids at different temperatures are solved with ultra-fast excitation of the electronic population by a laser pulse with peak intensity 10^{11} W/cm^2. From

their results, it can be deduced that, from very early on, an electron equilibrium distribution with a given electronic temperature T_e is established and follows the pulse fluence adiabatically. Similar conclusions were experimentally obtained in [24] for intensities in the 10^{12} W/cm^2 range.

As for the ions, they will remain cold for significantly longer, even when their collision rates with electrons are at their peak, i.e. $\nu_{e-ion} \approx \nu_{e-e}$ (corresponding to the flat top of figure 1.4), because of their much bigger mass which makes energy transfer rates slower. For example, in the case of copper, the characteristic energy exchange time will be on the order of tens of picoseconds [19].

From the moment equilibrium is reached in the electronic population, thermodynamic properties - like heat capacity - can be safely used to describe the energy exchange between electrons and ions. These will be dependent on the temperature of both electrons (with well known degenerate - $C_e \approx \pi^2 k_B^2 T_e / 2\epsilon^f$, and classical limits $C_e = 3k_b/2$) and ions (where for lower temperatures $C_{ph} \approx 3k_B$ due to harmonic character of atomic motion changes to $C_i \approx 3k_B/2$ as said motion turns to a translational mode).

The electrons are subject to multiple forces (or drifts) during irradiation. The most consequential one, in our regime, due to its bigger magnitude and lasting effects (still active after the pulse) is the thermal drift [17][19]. For intensities $I < 10^{13}$ W/cm^2, this drift will act as a perturbation to the ionic potential exciting harmonic motion. As the lattice heats up, through electron-phonon collisions, the phonons lose their harmonic behavior and start interacting with each other. The average displacement goes from zero to temperature dependent and the material will experience lattice expansion and melting.

For higher intensities, above the so-called ablation threshold, electrons might transfer enough energy to ions to vaporize them, in which case they are removed from the solid at relatively long time scales ($\sim \delta_s/c_s$). This effect is preceded by a disordering of the material, at densities close to the solid one, which can be interpreted as melting [17]. Figure 1.5 schematically shows all of the processes discussed so far, from the non-thermal excitation of electrons to the final equilibration of the electrons and ions above the melting temperature. In some cases, even while the ions are still cold, but after the electrons are thermalized, the abrupt change in effective electronic potential the latter feel due to electronic heating might originate forces strong enough to quickly disorder the material. In this scenario (non-thermal melting), the increase in ionic temperature and decrease in density will happen in an already "melted plasma" state.

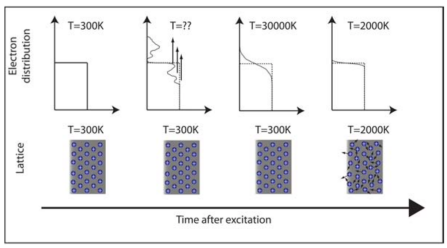

Figure 1.5: Sketch of energy deposition and relaxation processes in laser irradiated metal. First, the cold electronic population is excited into a non-thermal population, then the population thermalizes and forms a Fermi-Dirac before relaxation to the ions to a joint temperature. From [17].

A controversial but even more extreme mode of ablation may also exist, called Coulomb explosion. This process is known to happen in large molecules or clusters, where highly excited electrons leave the structure,

resulting in repulsive forces between the ions that destroy the cluster [17]. In [25] the possibility of this electrostatic ablation mode was studied for solids. It was concluded that while in dielectrics sufficient charge can build up at the surface boundary to create electrostatic pressure comparable to the mechanical binding strength; in metals the higher electron number density and mobility resulted in a more efficient neutralization of the electrostatic field, generally excluding the Coulomb explosion ablation mode.

1.5.3 The Two-temperature Model

From the discussion in section 1.5.2 we expect transient (non-equilibrium) states of elevated temperatures and unchanged density (roughly solid one) to exist in our sample, for at least a few picoseconds, after excitation and before ablation. To describe the thermal equilibration of electrons with ions across different phase states (from cold solids to non-equilibrium dense plasma) the two-temperature model (TTM), first proposed in [26], is often used. From the moment e-e population reaches equilibrium, and while total mass and momentum remain conserved, i.e., no hydrodynamic motion has taken place, energy conservation can be expressed as [19]:

$$\frac{\partial C_e n_e T_e}{\partial t} = Q_{abs} - \Delta Q_{e-th} - Q_{e-i} \text{ and } \frac{\partial C_i n_i T_i}{\partial t} = Q_{e-i} \tag{1.20}$$

where Q_{abs} is given by equation 1.19, $Q_{e-i} = \nu^E_{e-i} n_e (T_e - T_i)$ where ν^E_{e-i} is the e-i energy exchange rate and n_e is the electron number density; finally $\Delta Q_{e-th} = \kappa_e \nabla T_e$ is the conduction term.

Now from [27], we know that in solids:

$$\kappa_e = C_e n_e D \text{ and } D = \frac{\nu_e l_{mfp}}{3} = \frac{\nu_e^2}{3\nu^{mom}_{e-ph}} \tag{1.21}$$

with D the diffusion coefficient, ν^{mom}_{e-ph} the electron-phonon exchange rate, ν_e the electronic velocity and l_{mfp} the electronic mean free path. This diffusion approximation is also legitimate, on a skin-layer length scale, for intensities above the ablation threshold, here ν^{mom}_{e-ph} should be replaced with $\nu^{mom}_{e-i} = (M_i/m_e)\nu^E_{e-i}$ the electron-ion collision rate. Some authors considered enhanced laser energy penetration by conduction due to ballistic electrons (high energy tail electrons) but this approach is phenomenological and not based on sound kinetic arguments [17] (where another commonly used parameterization of κ_e between known ideal plasma and solid regimes is also given).

The dependencies on electron and ion temperatures of C_i, C_e and ν_{e-ph} also remain up for debate. For the latter parameter, the situation in figure 1.4 is no longer applicable as electrons and ions do not share a single temperature. Furthermore, the concept of phonons is no longer applicable after lattice disordering ("melting") and other models are needed, as in [28], where non-thermal distributions were accommodated in the calculations. These will be discussed more in-depth in 2.2.3.

As previously stated, this picture also assumes that there is no macroscopic material expansion. To know up to when this is a valid assumption, phase state information is needed - for which other approaches are required. One of the simplest analytical hydrodynamic models that attempted to describe the expansion of

the material after fs laser excitation was proposed in [26], for intensities close to the ablation threshold.

The initial excitation is viewed as isochoric heating of the electrons. e-i equilibration is assumed faster than material expansion, which is, in turn, considered faster than heat conduction times. These approximations result in an adiabatic expansion (i.e., along an isentrope) of the material, at the sound velocity $c_s = \sqrt{(\partial p/\partial \rho)_S}$, after the heating and equilibration temperature is reached. At the typical sound velocities for metals $c_s = 5000$ m/s it still takes tens of picoseconds for the ions to travel 100 nm, justifying our previous approximations, even for thin foils.

Chapter 2

State of the art

2.1 Probing non-equilibrium WDM states

Time-resolved diagnostics of appropriate time resolution are necessary to study the properties of the transient warm dense states generated during IH. Otherwise, a measurement with a single time stamp can be contaminated by widely different temperatures, pressures and densities, as these quantities vary over time. The study of conditions before a thermal electronic distribution is established is only possible with sub-picosecond resolution techniques, which are then deployed to study fast equilibration dynamics and subsequent processes.

With these aims in mind, several pump-probe techniques have been developed to access the exotic states following laser excitation, among them: optical probing, X-ray absorption spectroscopy, emission spectroscopy and time-resolved electron and X-ray diffraction [5]. They have in common that an adjustable time delay between the pump signal (that "creates" the conditions in the sample we wish to study) and a probe pulse (of varying nature, depending on what we wish to probe) allows us to study some optical or transport property at a certain time after the excitation. As the pump and probe are perfectly synchronized and the time delay is adjusted by changing the optical paths, the time resolution is usually limited by pulse duration.

Of these methods, the simplest to implement (due to the availability of light sources) are the optical probe ones. In these experiments, simultaneous measurements of reflectivity and transmissivity or phase in both polarisations can lead to the complete determination of the dielectric function [29], which can be used to determine ν^{e-ph} in different regimes, among other properties. The relationship between measurements and electron/structural properties is however indirect and based on a model such as Drude's. Other common optical probing techniques are velocity interferometry system for any reflector (VISAR) that allows for the measurement of the velocity of a reflecting surface, such as an ablated and extended plasma plume; and streaked optical pyrometry where the black-body radiation relation is used to measure time-dependent peak surface temperature (as the medium itself is opaque to optical radiation and, as such, radiation from the bulk of the material is trapped) [5].

Time-resolved diffraction experiments, on the other hand, are typically carried out with X-rays. They have several advantages including penetrating the bulk of the material. Due to the nature of X-ray diffraction,

they are good probes of ionic structure and consequently of phase transitions and states that the sample goes through as it becomes warm dense. The birth of the X-ray free electron laser (XFEL) greatly improved the time resolution of these experiments as it can provide a femtosecond source of high-brightness collimated X-rays. Ultrafast laser-accelerated electrons have also been deployed to study diffraction patterns and consequently long-range order of ions. Bright X-ray sources can be deployed in WDM diagnostics for Thompson X-Ray scattering experiments, as well. These can measure the dynamic structure factor that can be linked to the dielectric function [5].

X-ray absorption experiments, when close to absorption edges (XANES: X-ray Absorption Near Edge Spectroscopy) provide direct information about both the valence electrons and the short-range atomic order. For the diagnostics to work, however, it needs broadband high-brightness radiation on a time scale compatible with the desired time resolution. On the side of large facilities, while synchrotrons provide the necessary broadband radiation their pulse width of $\tau_p \approx 100$ ps severely limits temporal resolution and consequently the ability to perform IH non-equilibrium studies. XFELs offer a possible avenue for improvement of XANES techniques, despite their narrow spectral range, because tunability of the beam spectral jitter can be used to obtain enough range for X-ray absorption spectroscopy experiments [5].

The tabletop versions of such experiments are constrained in their time resolution by the availability of broadband X-ray sources of small enough duration (they are typically produced from plasma emission inherently limited due to heating and cooling dynamics of the plasma [29]). Source intensity is also a limiting factor as it regulates the number of shots needed for obtaining a spectrum. In WDM conditions, the sample is expected to ablate, creating a bottleneck in said acquisitions, since there is a need to move or replace the sample after each shot.

A schematic electron density of states (DOS) is present on figure 2.1. The probe pulse of a XANES experiment will have energy centered around one of the edges (K, L, M, etc) and as such will be able to make an electron on the sample transition from a core state to a near-free (continuum) one. The cross-section of such a process is dominated by the photoelectric effect coupling the two levels and is given by [29]:

$$\sigma(h\nu) = c \cdot h\nu |\langle \psi_i | R | \psi_f \rangle|^2 [1 - f(E)] \tag{2.1}$$

where R is the electric dipole operator, c is a constant and $f(E)$ is the Fermi Dirac distribution, explicitly dependent on energy instead of momentum. The last factor in the above expression describes the availability of the final state for the transition since for fermions the Pauli exclusion principle needs to be respected.

Generically, then, the absorption spectrum will have a sharp edge (as the X-ray probe energy moves from lower to higher than the edge's energy) followed by additional higher energy features. For $\sim$ 10 eV after the edge, these features result from the near continuum electronic structure (contained in $|\psi_f\rangle$ whose square modulus gives us the DOS), further features are a consequence of short-range order, i.e scattering of $|\psi_f\rangle$ on nearest neighbors atoms. As such, X-ray absorption measurements can directly probe the distribution of valence electrons and, consequently, be sensitive to the disturbances to the electronic population as the sample is isochorically heated to warm dense conditions.

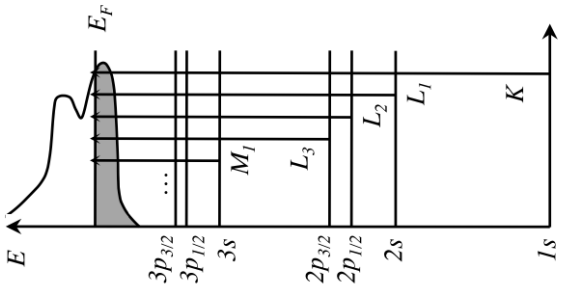

Figure 2.1: Energy diagram of different core states transitions to near continuum states. E_f is the Fermi energy and the different edges are labeled. Adapted from [29].

2.2 Simulating non-equilibrium WDM

This section will focus on the warm dense conditions achieved by isochorically heating thin metal samples. When modeling such conditions, with several important effects competing for dominance at any given phase state, the question often becomes which effects is our type of experience most sensitive to. From now on, X-ray and extreme ultra-violet (XUV) time-resolved studies near absorption edges with pump fluences up to 5×10^4 J/cm^2 (corresponding to $I \approx 10^{14}$ W/cm^2) will be our main concern. As mentioned before, these types of experiments are most sensitive to the behavior of the electronic distribution function. This function is in turn heavily dependent on the electronic temperature, which will vary abruptly throughout the experience and lead to multiple degeneracy regimes and many-body effects. These may change the screening of outer electron shells and as such the band structure and DOS of the metal.

Since the shielding and degeneracy regimes change rapidly in the warm dense region of the phase space diagram, as explored in section 1.2, our models will generally need to be tailored for the high-density regime (close to solid density), while they will need to "withstand" a range of degeneracy regimes as the electrons quickly heat up and then equilibrate with the ions.

To know at which point sample expansion starts to be significant, equilibration dynamics and equation of state considerations usually need to be taken into account in what we will call TTM - Hydro simulations. These will be discussed first, together with a more detailed description of the possible avenues for simulating the behavior of the electronic population during and after IH.

2.2.1 Hydrodynamic Regime

The pure TTM equations, discussed in section 1.5.3, are only valid so long as mass conservation can be reasonably assumed, i.e., up until significant hydrodynamic expansion takes place. To take into account phase state effects, such as moderate changes of density from solid to liquid phase or more abrupt ones to a vaporized state, it is possible to couple these equations to the equation of state (EOS), obtained from other means, which models thermodynamical properties of materials at high temperatures and pressures. For our purposes, these simulations will be used to define the time range we are interested in, namely up to what point, after heating, the density remains close to the solid one.

This type of study was done in [21] where TTM equations were coupled to an EOS to simulate equilibration and expansion effects happening concurrently, on an isochorically heated metal sheet, with an optical laser pulse. The equation of states was taken from the SESAME database, for Al, whose electronic component resembles a free electron gas. The parameters for the TTM result from interpolation between known regimes (where electrons and ions are thermalized) and are extrapolated for the non-equilibrium situation, following the method used to construct figure 1.4. Simulations at $I = 10^{15}$ W/cm^2 were selected and density and temperature profiles were presented. The density profile is observed to significantly deviate from a vacuum-solid step-like shape on a picosecond time scale, as is illustrated in figure 2.2. Intensity scaling laws of pressure and temperature were also reported (these suggest that for aluminium (Al) irradiated with $I = 10^{14}$W/cm^2, peak electronic temperatures - T_e - of around 70000 K are to be expected).

In [30], simulations of isochorically heated metals, with an infrared laser pulse, were performed by coupling the EOS to the TTM. The EOS takes into consideration known information about phase transitions and meta-stable states, along with a separate model for evaporation. It was shown that at intensities of $I = 5 \times 10^{14}$ W/cm^2 ($F = 5 \times 10^4$ J/m^2) a melting front develops. This shock wave moving through the liquid is followed by a rarefaction wave (low pressure) leading to negative tensile stress and spallation (droplet formation). Simulated ablation depths appeared to be in broad agreement with experimental results for the several metals tested. For all of them, the overall picture remained similar: for the highest tested fluence a stable liquid phase forms over $\approx$ 100 nm of thickness and during 10's of picoseconds. This fluid state is characterized by a density only slightly lower than the solid one, on the same order of magnitude. It is also noticeable that for lower fluences the vacuum-material boundary remains mostly unchanged for tens of ps while at the highest ones a gas appears from the earliest times, indicating some amount of material ejection from very early on.

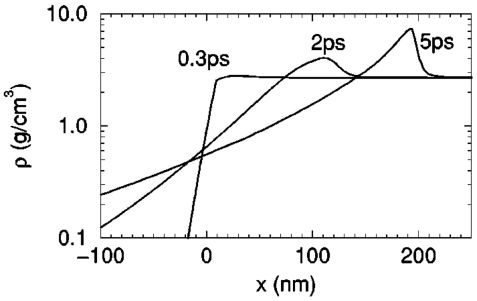

Figure 2.2: Temperature-desity profile of an Al sample irradiated for 150 fs with a 400 nm pulse with intensity $I = 10^{15}$ W/cm^2. Adapted from [21].

Although computationally more expensive, molecular dynamic (MD) simulations are another option to study the ablation process. They consist of individually solving Newton's equation of each atom, with the main challenge being the choice of the interaction potential between the atoms [17]. These have the advantage of not needing a priori assumptions about the kinetics of metastable states and phase transitions, but thermodynamical quantities need to be averaged out of simulated conditions. Smaller MD simulations often inspire the metastable phase states information that is then introduced in less demanding hydro-dynamical codes, through the EOS.

2.2.2 Modelling electronic distribution of WDM

The non-equilibrium states the metal's electronic population goes through, when isochorically heated, are not taken into account by hydro-TTM models. These states arise from the interplay of many-body correlations and the Pauli exclusion principle. When they do incorporate some quantum effects, this is achieved through EOS obtained from more accurate quantum mechanical simulations.

This section disucsses both finite temperature density functional theory created to overcome the problems arising from solving the quantum many-body Schrodinger equation (originally for much colder systems, but now often extended to WDM) and Boltzmann equation methods for non-ideal quantum plasmas. Both have advantages and disadvantages and can lean on one another. While finite temperature DFT does not model the deposition of energy, requiring an ad hoc source, and only works in equilibrium conditions (when the electrons have thermalized amongst themselves, but not necessarily with the ions); the Boltzmann equation methods successfully model both of those responses but are not capable of calculating the many-body properties of a correlated system, like the electronic band structure.

Density Functional Theory

Assuming we can determine the ionic potential separately (usually from quantum mechanics calculations for a single atom at long distances) our generic goal is to solve the many-body Schrodinger equation that governs the dynamics of any quantum system. One such system of N electrons subject to an external static potential (created by the ions) is described by the spin-independent Hamiltonian [31]:

$$H = \sum_{i=1}^{N} \left(-\frac{\hbar}{2m}\nabla_i^2 + V(\mathbf{r}_i) \right) + \frac{1}{2}\sum_{i \neq j} \omega_{ij}(\mathbf{r}_i, \mathbf{r}_j) \tag{2.2}$$

with V the external potential and ω_{ij} the e-e interaction energy. The desired result is to discover $\Psi(\mathbf{r}_1, ..., \mathbf{r}_N)$ describing stationary electronic states. Density Functional Theory (DFT) offers a way to map this N-body interacting problem into a non-interacting single-body one (i.e without ω_{ij}), making use of the density operator, expressed in coordinate space as:

$$n(\mathbf{r}) = N \int d^3\mathbf{r}_2 ... \int d^3\mathbf{r}_N \Psi^\dagger(\mathbf{r}, \mathbf{r}_2, ..., \mathbf{r}_N)\Psi(\mathbf{r}, \mathbf{r}_2, ..., \mathbf{r}_N). \tag{2.3}$$

In [32] it was proven that there is a universal functional of the density $F(n(\mathbf{r}))$, independent of the external potential, such that $\int V(\mathbf{r})n(\mathbf{r})d\mathbf{r} + F(n(\mathbf{r}))$ has its minimum equal to the ground state energy of the interacting electron problem. To do so, the authors used the fact that the ground state wavefunction is a unique functional of $n_0(\mathbf{r})$ (a given ground state density), which can be derived from equation 2.3. The functional itself was written as:

$$F(n(\mathbf{r})) = \frac{1}{2}\int\int \frac{n(\mathbf{r'})n(\mathbf{r})}{|\mathbf{r} - \mathbf{r'}|} d^3\mathbf{r'}d^3\mathbf{r} + V_{XC}(n(\mathbf{r})) \tag{2.4}$$

where the first term is a Hartree-like one (responsible for e-e repulsion) while the second one is an exchange

term, that parameterizes all the many-body interactions. This proof was extended to finite temperature systems in [33] by using the grand canonical ensemble. Proving that for a given temperature, number of particles, and external potential the equilibrium density is unique, the authors were able to add a chemical potential term to the functional. As the electrons can be excited into infinitely many continuum states, the occupancy of those states becomes needed in our density definition, which becomes [31]:

$$n(\mathbf{r}) = 2\sum_{i=1}^{\infty} f(\epsilon_i) \int d^3\mathbf{r}_2 ... \int d^3\mathbf{r}_N \Psi_i^{\dagger}(\mathbf{r}, \mathbf{r}_2, ..., \mathbf{r}_N)\Psi_i(\mathbf{r}, \mathbf{r}_2, ..., \mathbf{r}_N) \tag{2.5}$$

with $f(\epsilon_i)$ the occupancy factor for a given energy state's energy ϵ_i and where the factor of two comes from spin independence. Now for our stationary case, f will be a Fermi-Dirac distribution (i.e equilibrium one). With the knowledge of the form of the distribution, we can then use charge conservation to determine the chemical potential needed in the functional [31].

In [34], the Kohn-Sham (K-S) equations governing the behavior of the auxiliary non-interacting system (resultant from the mapping of the original system of interacting fermions) were derived. The Hamiltonian present in the K-S equation was of the form of equation 2.2 but without the last term (the system is now non-interacting) and with $V(\mathbf{r}_i)$ replaced by $V_{eff}(\mathbf{r}_i) = V(\mathbf{r}_i) + F_t(n(\mathbf{r}_i))$ with F_t the finite temperature form of the functional in expression 2.4. These equations yield static orbitals $\varphi_i(\boldsymbol{r_i})$ related to the original system by $n(\mathbf{r}_i) = \sum_{i=1}^{N} |\varphi_i|^2(\boldsymbol{r_i})$ and need to be solved self-consistently, i.e., iteratively.

The bottleneck of the DFT method is the determination of the exchange correction part of the functional. In general, and specifically for WDM, the exact form of this functional is not known and depends explicitly on the temperature and density [31]. Moreover, this method is not translatable into non-equilibrium situations, for example during and after irradiation of a sample, i.e., during the heating process. The density functional, defined in 2.5, is only properly defined if the form of the occupancy factor is known. To properly account for the excitation of electrons, time-dependent DFT would be needed but it is too computationally demanding at the time scales and levels of perturbation we are interested in.

In [35], finite temperature DFT simulations (hot electrons and cold ions) were used to calculate the electronic density of states of several metals. The location in energy of the d band, the number of free electrons, and the chemical potential were then extracted for different electronic temperatures up to 50000K.

In the case of Al, the electronic structure is similar to the free electron gas (FEG) structure, for all the studied temperatures. The number density of conduction electrons remains constant with increasing temperature: 10 electrons occupy core bound states while three are in the conduction band, delocalized. Since the dispersion relation of the FEG is $\epsilon \propto k^2$, the closely related density of state (DOS) can be calculated as $D(\epsilon) \propto \sqrt{\epsilon}$. The constancy of the DOS for different temperatures is an indication that there are no significant ultra-fast properties modifications due to electronic excitation, such as bond hardening.

For Titanium (Ti), a transition metal with a semi-full $3d$ band, the DOS is higher and flatter band resulting from a bigger localization, in energy, of the d electrons and only at higher energies decays to $D(\epsilon) \propto \sqrt{\epsilon}$, characteristic of the s and p free like electrons. The number of conduction electrons in Ti varies little from its cold value and the d band location, in terms of energy location, is also scantly affected: there is only a

slight reduction of the energy of the continuum. For both Al and Ti the chemical potential variation from the Fermi energy, with increasing temperature, is roughly the same. The DOS for both metals at 0 K, 10000 K, and 50000 K of electronic temperature are shown in figure 2.3 as solid lines. Overlaid on the same plot are Fermi-Dirac distributions at for the same T_e and appropriate chemical potentials.

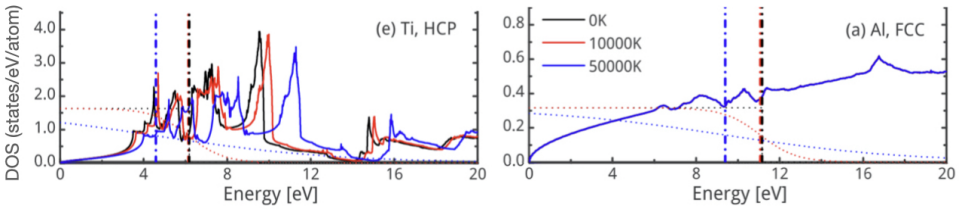

Figure 2.3: Electornic density of states (DOS) for Al and Ti at finite temperatures. The dashed lines are the chemical potentials and the dots overlaid are the corresponding Fermi-Dirac distributions. Adapted from [35].

In the case of noble metals, whose *d* orbital is full and lower than the Fermi level, significant variations of the parameters discussed above can be observed. This can be understood as changes in screening, due to the depletion of the *d* orbitals resulting from electronic excitation. Most changes occur abruptly, after a given temperature threshold (usually the temperature needed for electrons from the *d* orbital to cross to empty energy levels). As the more energy-localized electrons get excited to higher energies, the screening of the charge of the nucleus is reduced (electrons stop bunching together closer to the nucleus and disperse into the lower-density part of the DOS, which is also further away from the core) and the energy of the continuum is lowered. This effect is limited in Ti because the *d* orbital was not full to begin with, and also because, at the studied electronic temperatures, a significant proportion of excited electrons scatters to the empty part of the *d* orbital.

Ab initio simulation of X-ray absorption experiments

Changes in the ionic structure due to heating of the lattice and, at some point, of the ions can not be properly modeled in a DFT simulation, since it concerns only the electronic population. Moreover, finite temperature DFT simulations have as input an electronic temperature and as such, by themselves, they can not model the heating process.

To achieve a full description of the sample, especially when time resolutions are on the order of picoseconds, coupling the simulation of quantum electrons with that of classical ions becomes necessary, in what is typically termed a DFT-MD (density functional theory-molecular dynamics) approach [36]. The TTM is also used, in this scheme, to simulate energy exchange between the populations and define the temperatures at each time step. From this process, it is possible to gauge the different configurations of ions that appear over time, as the sample is being heated to WDM conditions and afterwards. This information is often condensed in an EOS (such as the ones in SESAME data base [37]) that drives hydrodynamical simulations.

For the simulation of optical properties of the isochorically heated metal (in our case, absorption near one of the edges), the above procedure needs to be inverted. To drive the DFT-MD simulations that require electronic temperature and ionic density information, we extract said parameters from TTM-hydrodynamical

simulations and/or experimental benchmarking. Starting from cold ions on a lattice and excited electrons at a given T_e, DFT can be used to calculate the electronic band structure and the forces the electrons apply to the ions (by the Hellman-Feymann Theorem) and then let them move according to classical MD. The procedure can be repeated iteratively, for each time step of the simulation, always recalculating the DOS, until reaching the expected phase state (i.e, level of equilibration expected at a given time, according to the TTM). [29]

Electronic and ionic temperatures need to be attributed independently because truly ab initio simulations with time-dependent DFT can not be run on a scale - time and length-wise - enough to simulate the excitation and equilibration (both e-e and e-i) in the macroscopic metals films starting from a cold state. The less demanding stationary DFT methods provide adequate results as long as time resolutions are of the order of e-e equilibration times. When sufficiently small time scales are achieved, time-dependent DFT will be needed, for the first few steps, to simulate possible non-equilibrium distributions coming directly from excitation effects.

With this method we can calculate the absorption cross section (in linear response theory), for any given **k** point in the electronic continuum [38]:

$$\sigma_{\mathbf{k}}(h\nu) = 4\pi^2 h\nu \sum_n [1 - f(\varepsilon_{n,\mathbf{k}})] \times |\langle \psi_{n,\mathbf{k}} | \nabla | \phi_{core} \rangle|^2 \delta(\varepsilon_{core} - \varepsilon_n - h\nu) \tag{2.6}$$

with $|\phi_{core}\rangle$ electronic core states. The optical properties are, then, consistently determined with $|\psi_n\rangle$ calculated with DFT-MD and the core states are determined separately, as DTF-MD does not consider the quantum nature of the ions. To take into account the experimental resolution, when it is larger than the state's lifetime, the delta function is replaced by a Gaussian.

In practice, one can not include the infinite near continuum excited electronic orbitals in a computer simulation. The projector-augmented wave method is among the ones that can be used to describe both the near continuum and core states. Care is needed to include sufficiently many excited states in the continuum and to include the state with a hole in the core (that can be created by the probe itself) if this effect is not completely screened out by valence electrons. [29]

Quantum Boltzmann Statistics

The method summarized above assumes equilibrium within the electronic population along with an ad hoc method of absorption. To truly account for non-equilibrium dynamics, a kinetic quantum equation is required with detailed collision terms describing both e-e interaction and interaction of the "free-like" electrons with the IR ultrafast laser pulse. This can be done via the Boltzmann equation, as introduced in section 1.2.2. The remaining problem pertains to writing the collision term explicitly.

Focusing on the two particle collisions with momentum $\mathbf{p}_1$ and $\mathbf{p}_2$, the total number of out-scattered particles into momentum states $\overline{\boldsymbol{p}}_1$ and $\overline{\boldsymbol{p}}_2$, assuming that the colliding particles are uncorrelated (molecular chaos assumption), as a function of $\mathbf{p}_1$ is given by [11]:

$$I^{\text{out}}(\boldsymbol{p}_1) = \int d\boldsymbol{p}_2 d\overline{\boldsymbol{p}}_1 d\overline{\boldsymbol{p}}_2 W(\boldsymbol{p}_1 \boldsymbol{p}_2 \overline{\boldsymbol{p}}_1 \overline{\boldsymbol{p}}_2) f(\boldsymbol{p}_1) f(\boldsymbol{p}_2) \times (1 \pm f(\overline{\boldsymbol{p}}_1))(1 \pm f(\overline{\boldsymbol{p}}_2)) \tag{2.7}$$

with $W(\boldsymbol{p}_1\boldsymbol{p}_2\overline{\boldsymbol{p}}_1\overline{\boldsymbol{p}}_2)$ the transition probability per unit time. Note that the factor $f(\boldsymbol{p}_1)f(\boldsymbol{p}_2)$ encodes the assumption of molecular chaos and the $\pm$ symbol reflects the fact that while fermions can only scatter into unoccupied states, bosons tend to scatter into the most occupied states. Naturally the I^{out} factor has the same form but $\mathbf{p}_1$ switches places with $\overline{\mathbf{p}_1}$ and the same for $\mathbf{p}_2$. The total two-body collision term can then be written as: $(\partial f/\partial t)_{\text{coll}} = I^{\text{in}}(\boldsymbol{p}_1) - I^{\text{out}}(\boldsymbol{p}_1)$.

If the interaction potential between the particles can be considered weakly time-dependent, perturbation theory from standard Quantum Mechanics can be used to derive the Fermi Golden Rule [11]:

$$W(\boldsymbol{p}_1\boldsymbol{p}_2\overline{\boldsymbol{p}}_1\overline{\boldsymbol{p}}_2) = \frac{1}{(2\pi\hbar)^6}\left|V_{12}(\boldsymbol{p}_1-\overline{\boldsymbol{p}}_1)\right|^2\delta(\boldsymbol{p}_1+\boldsymbol{p}_2-\overline{\boldsymbol{p}}_1-\overline{\boldsymbol{p}}_2)\times\frac{2\pi}{\hbar}\delta\left(E_{12}-\bar{E}_{12}\right) \tag{2.8}$$

where $V_{12}(\boldsymbol{p}_1-\overline{\boldsymbol{p}}_1)$ is the Fourier transform of the two particle interaction potential and the energy and momentum conservation are explict. In the simplest case of free particles, it is possible to write $E_{12} = p_1^2/2m_1 + p_2^2/2m_2$.

The Boltzmann equation (1.8), presented with the proper collision term, describes the relaxation of an arbitrary initial distribution into an equilibrium state conserving the mean kinetic energy, instead of the total one that includes the potential energy. Moreover, if the molecular chaos assumption is used, the kinetic equations are only valid for timescales large enough so that the initial correlations of the systems have decayed.

Boltzmann statistics: IH heating of metals

In [23], a much-used Boltzmann equation model for thin metal sheets being irradiated by femtosecond IR and optical laser light was developed. Several simplifying assumptions are laid out first since the computational problem of solving the Boltzmann equation with detailed collision integrals quickly becomes intractable.

Firstly, the material is assumed homogeneous and isotropic. This is justified by the fact that the metal sheet is composed of micro-crystals oriented differently from one another and it allows us to take an average of all polarization directions of the incident laser light. Furthermore, spatial variations of the intensity of the laser pulse, as it is being absorbed transversely, can be neglected, for films with thickness on the order of the absorption depth of the metal. Other transverse spatial effects, such as diffusion and energy transport were also neglected. This last assumption is consistent with a thin layer approximation and a focus on time-dependent effects such as energy absorption and thermalization amongst the electrons (first) and of electrons with the lattice (later).

Taken together, these impositions make the distribution function only dependent on time and energy and, as such, reduce the left-hand side of equation 1.8 to the partial temporal derivative. The dynamics of the systems are then encapsulated in the collision terms, caused by different microscopic processes. The relevant terms are e-e, e-i, and electron-phonon collisions (the latter are included in the original model, but are of questionable use for pump intensities above the damage threshold). As was previously discussed in section 1.5.1, the main process for deposition of energy, at these fluences and wavelengths is IB, i.e. e-i/electron-phonon collisions that allow for momentum conservation while absorbing one or multiple photons.

All these considerations lead to a system governed by two kinetic equations:

$$\frac{\partial f(k)}{\partial t} = \frac{\partial f(k)}{\partial t}\bigg|_{\text{el}-\text{el}} + \frac{\partial f(k)}{\partial t}\bigg|_{\text{el}-\text{phon}} + \frac{\partial f(k)}{\partial t}\bigg|_{\text{absorb}} \tag{2.9}$$

$$\frac{\partial g(q)}{\partial t} = \frac{\partial g(q)}{\partial t}\bigg|_{phon-el} \tag{2.10}$$

with $f(q)$ the electronic distribution function and $g(q)$ the distribution functions of the phonons. No ionic equation is present due to the electronic-to-ionic mass ratio, which makes e-i collisions approximately elastic. Here the focus shall be on equation 2.9, disregarding the el-phon term, since detailed calculations are mainly required to determine the dynamics of e-e thermalization, after being excited by the laser pulse. After the electronic population is distributed according to a Fermi-Dirac, the conditions of validity of the TTM are met. This simplified version of the original model is then expected to work for up to hundreds of fs only, before electron-phonon/e-i thermalization becomes significant.

Two detailed collision terms need to be determined: the e-e and the absorption (electron-ion-photon) terms. Both will have probabilities per unit time proportional to expression 2.8 where the $|V_{12}(\boldsymbol{p}_1 - \overline{\boldsymbol{p}}_1)|^2$ term can be identified with expression 1.14, i.e., the statically screened Coulomb potential. Assuming a single parabolic conduction band the dispersion relation of the free electrons is given by $\epsilon(\boldsymbol{k}) = \hbar^2 k^2/2m_e$. It is then possible to write, in the two-body scattering approximation:

$$\begin{aligned}\frac{\partial f(\boldsymbol{k})}{\partial t}\bigg|_{\text{el}-\text{el}} = \frac{2\pi}{\hbar}\sum_{\boldsymbol{k}_1}\sum_{\boldsymbol{k}_3}\left(\frac{e^2}{\varepsilon_0\Omega}\frac{1}{\Delta k^2+\kappa^2}\right)^2 \delta\left(\epsilon\left(\boldsymbol{k}_3\right)+\epsilon\left(\boldsymbol{k}_1\right)-\epsilon\left(\boldsymbol{k}_2\right)-\epsilon(\boldsymbol{k})\right) \\ \times\left[f\left(\boldsymbol{k}_3\right) f\left(\boldsymbol{k}_1\right)\left(1-f(\boldsymbol{k})\right)\left(1-f\left(\boldsymbol{k}_2\right)\right)-f(\boldsymbol{k}) f\left(\boldsymbol{k}_2\right)\left(1-f\left(\boldsymbol{k}_3\right)\right)\left(1-f\left(\boldsymbol{k}_1\right)\right)\right]\end{aligned} \tag{2.11}$$

where $\Delta\boldsymbol{k} = \boldsymbol{k}_1 - \boldsymbol{k}_2 = \boldsymbol{k} - \boldsymbol{k}_3$ is the exchanged momentum and $\boldsymbol{k}_2 = \boldsymbol{k}_1 - \boldsymbol{k} + \boldsymbol{k}_3$ to ensure conservation of momentum. The Fourier Transform operation performed on the screened Coulomb potential leads to the appearance of a volume term Ω, corresponding to the total volume of the crystal being modeled, but is inconsequential as it cancels out further along when the sums are transformed to integrals. The inverse screening radius can be obtained from equation 1.13, valid for arbitrary degeneracy, encompassing different temperature and density regimes. With the quasi-free dispersion relation being assumed, the expression can be written as:

$$\kappa^2 = \frac{e^2 m_e}{\pi^2\hbar^2\epsilon_0}\int_0^\infty f(k)dk. \tag{2.12}$$

As for the absorption term, the aim is to accurately model the IB process, in a microscopic and kinetic fashion. As derived in [39] and used in [23], the probability of absorption of n photons by an atom departs for the usual form - expression 2.8 -, for the collision of two particles. To calculate the probability of transition from a state with energy ϵ to a state with energy ϵ' the authors wrote the time-dependent Schrödinger for free electrons disturbed by classical E-M radiation (the quantum nature of the photons can be disregarded as there is a great many of them in a given energy state). Afterward, first-order perturbation theory was applied to calculate the desired transition probability (taking the nucleus potential as the perturbation), resulting in:

$$W(\epsilon \to \epsilon') = |V_{12}(\boldsymbol{\Delta k})|^2 \sum_{\ell=-\infty}^{+\infty} J_\ell^2 \left(\frac{e\boldsymbol{E_L} \cdot \boldsymbol{\Delta k}}{m_e w_L^2} \right) \delta(\epsilon' - \epsilon + \ell\hbar\omega_L) \tag{2.13}$$

where ℓ is the number of absorbed or emitted photons, $\boldsymbol{E_L}$ is the electric laser field, V_{12} is still the screened Coulomb potential that mediates e-e interaction, but in this case for e-i interaction, and J_ℓ is the ℓth order Bessel function of the first kind. If it is also assumed the ions are classical particles and that they have infinite mass (such that there is no energy transfer to the ions), the absorption term for the Boltzmann equation can then be written as:

$$\begin{aligned} \left.\frac{\partial f(\boldsymbol{k})}{\partial t}\right|_{\text{el-ion-phot}} &= \frac{2\pi}{\hbar} \sum_{\boldsymbol{\Delta k}} \left(\frac{e^2}{\varepsilon_0 \Omega} \frac{1}{\Delta k^2 + \kappa^2} \right)^2 \sum_{\ell=-\infty}^{\infty} J_\ell^2 \left(\frac{e\boldsymbol{E_L} \cdot \boldsymbol{\Delta k}}{m_e w_L^2} \right) \\ &\times \delta\left(\epsilon(\boldsymbol{k} + \boldsymbol{\Delta k}) - \epsilon(\boldsymbol{k}) + \ell\hbar\omega_L\right) \left[f(\boldsymbol{k} + \boldsymbol{\Delta k})(1 - f(\boldsymbol{k})) - f(\boldsymbol{k})(1 - f(\boldsymbol{k} + \boldsymbol{\Delta k})) \right] \end{aligned} \tag{2.14}$$

where in this case Ω will not cancel out, since there is a single sum that will be transformed to an integral, and can be identified with the volume of the unit cell Ω_0, as in [23].

While in general phonons also contribute to the IB process, calculations performed in [40] for IH of an Al thin film showed that the term $|V_{12}(\boldsymbol{q})|^2$ for phonons is two orders of magnitude lower than for ions, assuming a Debye dispersion relation $\epsilon_{pn}(q) = c_s q$, as can be seen in figure 2.4. This channel of absorption will be disregarded as, for experimental analysis purposes, second-order effects are both too costly computationally and unlikely to offer any significant benefits.

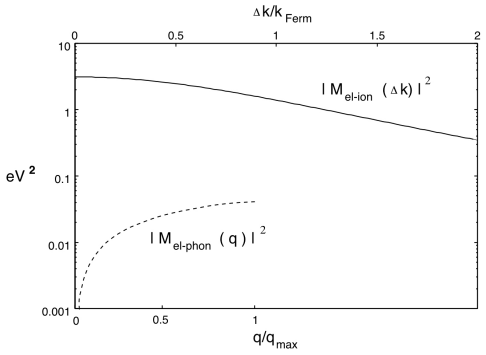

Figure 2.4: Modulus squared of the screened two-particle interaction potential for e-i and electrons-phonon interactions. From [40].

To summarize, the two terms here detailed, introduced into equation 2.9, while neglecting phonon contributions, provide a model for the behavior of nearly free electrons in thin metal sheets based on a single master equation, that needs to be solved in time. This model is expected to work on reduced time frames only because it assumes both that the lattice remains intact and that the transfer of energy from electron to ions or phonons is negligible (which will probably be true enough, at our experimental resolution - chapter 3, for a few hundreds of fs).

2.2.3 The TTM and e-i coupling

Section 2.2.2 covered computationally expensive simulations. In this section, we will discuss how these fundamental theories can be incorporated into the temperature dependency of the parameters of the TTM. This

has the distinct advantage of computational simplicity and has been amply shown to describe the pre-ablation moments of a thin irradiated metal sample after the electronic population is in equilibrium, within itself, and can be said to have a temperature. Note that, since we are interested in the first few ps after irradiation of a thin film, thermal dissipation effects will be neglected in the TTM. Changes in the electronic density will also be disregarded, as there is little to no ionization of core electrons expected at our irradiation intensities. Equation 1.20 can then be simplified to:

$$C_e\left(T_e\right)\frac{\partial T_e}{\partial t} = S_{abs}(\boldsymbol{r},t) - G\left(T_e\right)\left(T_e - T_i\right) \text{ and } C_i\frac{\partial T_i}{\partial t} = G\left(T_e\right)\left(T_e - T_i\right) \tag{2.15}$$

$S_{abs}(\boldsymbol{r},t)$ is the absorbed laser power density and $G(T_e)$ is the electron-phonon/ion coupling factor.

In [41] (Lin), the heat capacities of electron populations with finite temperatures in a cold metal lattice as well as the e-i coupling coefficient were determined, for different metals. The authors considered the electronic energy distribution as well as the DOS of the different metals. No deviations from the cold DOS due to electron heating were considered, however. The electronic heat capacity was calculated from the definition, i.e, the derivative of total electron energy with respect to T_e, as such:

$$C_e\left(T_e\right) = \int_{-\infty}^{+\infty}\frac{\partial f\left(\epsilon,\mu,T_e\right)}{\partial T_e}D(\epsilon)\epsilon d\epsilon \tag{2.16}$$

where $D(\epsilon)$ is the DOS that the authors calculated for cold metals, using ab initio DFT simulations and assumed constant for different electronic temperatures.

The parameter $G(T_e)$ is calculated from a rate equation (Boltzmann-like) reflecting the Fermi golden rule. The two-particle interaction potential (matrix element) was replaced by the zero temperature Eliashberg function, which is the product of the phonon density of states with the frequency-dependent coupling parameter that incorporates all the allowed scattering processes at a given frequency [42]. After some calculations, this process results in the following expression:

$$G\left(T_e\right) = \frac{\pi\hbar k_B\lambda\left\langle\omega^2\right\rangle}{D(\epsilon_F)}\int_{-\infty}^{+\infty} -\frac{\partial f\left(\epsilon,\mu,T_e\right)}{\partial\epsilon}D^2(\epsilon)d\epsilon \tag{2.17}$$

where λ is the mass enhancement parameter and $\left\langle\omega^2\right\rangle$ is the second momentum of the phonon spectrum which represents the integrated contributions of the Eliashberg spectral function. This function, commonly used in superconductivity theory, is a description, within Green's function formalism, of the probability of scattering of electrons with a transfer of crystal momentum to a phonon, of a given frequency. Originally developed from electrons near the Fermi surface and cold lattice, it can be extended to higher temperatures, with dubious results in the case of loss of crystal structure. In practice $\lambda\left\langle\omega^2\right\rangle$ was measured experimentally, for these calculations, and differed for each metal considered in [41]. Expression 2.17 was used to calculate the T_e-dependent e-i coupling coefficient with the results for Al shown in figure 2.5a and for Ti in figure 2.5b. Notably, the G coefficient for Ti is one order of magnitude higher than that of both Al and the Rethfeld free electron gas approximation. A decrease in the coupling also starts at around 6000 K, for Ti. In extended tabular calculations provided by the author, this decrease continues for at least up to 50000 K.

The Rethfeld calculations [23], previously described in section 2.2.2, also contained a electron-phonon

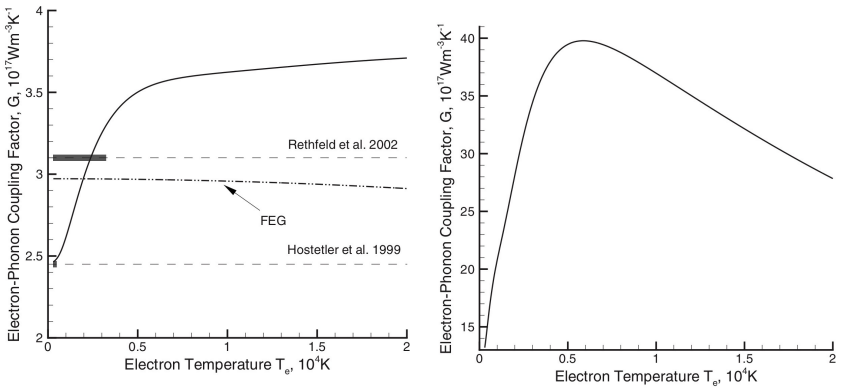

(a) Results for Al. The Rethfeld et al 2002 result pertains to results from [23].

(b) Results for Ti.

Figure 2.5: Electron ion coefficient G as a function of T_e obtained in [41].

collision term, with a simplified matrix element based on Debye models for phonons and on static screening of the Coulomb potential. It is then possible to model the behavior of both phonons and electrons, specifically the electron and phonon population energies, and from there extract a constant G coefficient plotted in figure 2.5a. For these calculations, the free dispersion relation was assumed, with m_{eff} set to the free electron mass.

In [43] (Petrov et al), a similar Boltzmann approach with static screening of the Coulomb potential and Debye phonon dispersion relation was followed, but different effective masses were considered for the s and d electrons, with their contributions to the e-i collision frequency calculated separately. The screening length was calculated from the Lindhard dielectric function [44]. Considerably corrections were shown to appear when the single band assumption is a poor one. In the case of transitions metals, for example, the overlapping shapes of d and s/p orbitals make inter-band excitation possible and render the single-band assumption a poor one, for moderate intensities. In the case of Al, due to its free electron dispersion relation and DOS, the predictions match up with the earlier results in [41], while there are no Ti results to compare.

In [45] (Muller et al), a Boltzmann approach was also used to write down a rate equation. Here the electron-phonon interaction potential was assumed the same as in [23], but instead of a free dispersion relation, a more realistic one was extracted from the DOS obtained from DFT simulations. The results were averaged in an isotropic one-band dispersion relation, enabling the uncovering of differences in the coupling coefficients between metals. Refinement of earlier results was achieved for Al, with broad agreement with the previous results from Rethfeld [23]. For lower temperatures, the coupling is below the prediction in [23], with the results quickly converging to the estimated value after that. For other metals, namely Ni, a transition metal with the Fermi edge at the end of the d orbitals, significant discrepancies are reported, compared to Lin's results.

In [42] (Waldecker et al), a procedure similar to Lin's was followed. After the by now ubiquitous rate equation was written, the two-particle interaction potential term of the Fermi Golden Rule was replaced by the Eliashberg function, but this time the dependence on the electronic and lattice temperature was maintained. To solve the system of equations, two inputs from ab initio DFT simulations were needed: the DOS function and the temperature-dependent Eliashberg function. The resulting calculations were performed within the accuracy of the DFT approach and did not have any experimentally determined parameters. The calculation

for Al suggests an underestimation of the coefficient by Lin et al, at somewhat low temperatures. Their experimental results, based on ultra-fast electron diffraction, seem to agree with Lin's calculations, however. The authors argue that this comes from the fitting of the $\lambda \langle \omega^2 \rangle$ parameter to experimental values. A non-thermal lattice model that considers three different non-thermalized phonon populations that they propose also produces agreement between their data and their first-principles calculations.

Finally, in [10] (XTANT-3), a hybrid model specific for material response under femtosecond irradiation was produced. The photoabsorption by the metal was modeled by a Monte Carlo, along with the dynamics of high-energy electrons. The band structure was calculated through a tight binding (TB) description, while the atomic motion was modeled by molecular dynamics. Boltzmann collision integrals (using the TD calculated band structure, which naturally varies with temperature and density) were used to couple the lower energy continuum electrons to atomic motion. The G parameters were extracted from the knowledge of this Boltzmann collision integral along with the electronic and ionic temperatures. The authors ran simulations for a considerable amount of different metals. More often than not, when comparison was possible, an overestimation of the G parameter by Lin et al was found.

The G coefficients as a function of electronic temperature, for Al, are shown in figure 2.6a, for all the different calculations discussed. The black points are experimental results, using ultrafast electron diffraction as a lattice temperature diagnostics. For Ti the results are shown in figure 2.6b, with simulations only available for the Lin et al and XTANT-3 case.

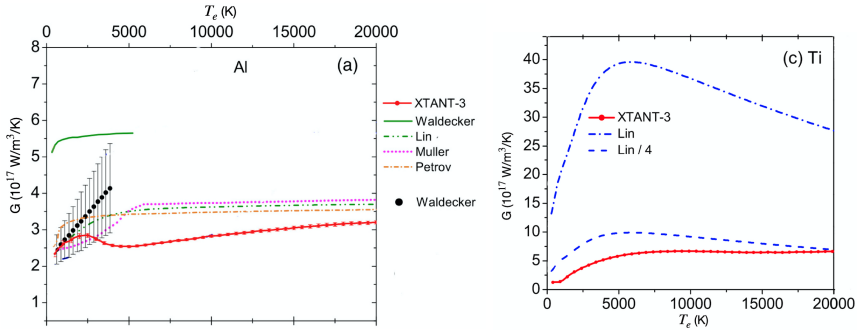

(a) Results for Al. The Rethfeld et al 2002 pertains to results from [23].

(b) Results for Ti.

Figure 2.6: Electron ion coefficient G as a function of T_e obtained from the different references mentioned above. Adapted from [10].

2.3 X-ray Absorption Near Edge Spectroscopy: XANES

This section will be dedicated to the exploration of experimental results in metal samples isochorically heated to warm dense conditions. The focal points of interest will be near-edge absorption experiments, that either take a full absorption spectrum or XUV/X-ray measurements at some finite number of frequencies where the sample is heated by a femtosecond optical or infra-red laser. X-ray Free Electron Lasers are excluded as sources for IH (pump pulses) because the absorption and relaxation pathways they entail are substantially different and require different models when electronic populations are driven far out of equilibrium.

XANES offers us the possibility of studying the effects of excitation of the electrons in tabletop setups or high-powered facilities. The experimental limiting factor is the X-Ray probe pulse that allows for the measurement of the absorption spectrum. On the side of large facilities, synchrotrons provide the necessary bright, broadband radiation but have a usual pulse duration of ~ 100 ps, which severely limits time resolution. Several methods for obtaining lower time resolution have been successfully applied, like using a streak camera [29]. X-ray free electron lasers, on the other hand, offer high brightness along with femtosecond pulse duration, overcoming many challenges of previous sources, but also a narrow spectral range requiring a large number of shots to recover an absorption spectrum. As for tabletop X-ray sources, considerable progress has been achieved with thermal emission from laser-produced plasmas and Bremsstrahlung emission produced from a water target (that is collected afterward) [29]. X-ray betatron radiation, produced from a laser-generated plasma from a tabletop setup, was used in [46] to probe the transition to a warm dense state of Cu, with fs time resolution. High Order Harmonic Generation (HHG), achieved by focusing an ultra-fast optical laser onto a gas cell [47], also produces XUV radiation with a duration of tens of fs that can prove useful to study the transition from upper core states to the continuum such as M shell transitions.

Despite the discussed time resolution limitation and limited control of hydrodynamic gradients in position space due to the lack of spatial resolution (complicated by the need for multiple shots to obtain the spectra, taken in different parts of the sample), XANES offers us a direct view into the behavior of the electronic population. To simulate the absorption rate, for different XUV and X-ray energies, on a picosecond timescale (compatible with the time resolutions of XANES experiments), the method used is typically the one described in section 2.2.2.

2.3.1 Aluminium

As previously mentioned in section 2.2.2, the Al DOS is free electron gas like up to high T_e. This result also holds for up to three times the solid density. Bellow it, however, a transition is observed from a conduction band to localized atomic orbitals [48]. Given the nature of its DOS, the interpretation of Al absorption spectra after IH heating, at least before the density drops, is fairly straightforward. Figure 2.7 reports XANES spectra from ab initio simulations. The modulations above the edge are progressively attenuated, for higher temperatures, which reveals their direct relation with short-range atomic order. As for the edge itself, since the electronic structure is not significantly affected by electronic excitation, it can be interpreted directly as the frontier between occupied and unoccupied states according to the Fermi distribution. The decrease of its slope with temperature is related to the thermal broadening of the Fermi level.

In [38], time-resolved XANES measurements of the K-edge of an isochorically heated thin Al film were reported ($\tau_L = 120$fs, $\lambda_L = 800$nm, $F = 6 \times 10^4$ J/cm^2, p-polarized light at 60° incidence) as shown in figure 2.8. The macroscopic evolution of the heated sample was also estimated with a TTM-Hydro code (temperatures and density), revealing e-i equilibration in all time steps except for the 2.5 ps one. The first spectrum at -7.5 ps is identical to the cold Al one. At 2.5 ps the modulations above the edge have completely disappeared revealing a solid-to-liquid transition (a fit of the slope of the edge indicates a T_e compatible with

the TTM prediction). For 22.5 ps and longer, a progressive transition to the 1*s*-3*p* atomic line appears.

While the experiments and simulations reported here are mostly in equilibrium conditions, these methods are promising for non-equilibrium situations as well, as in exemplified in figure 2.9. The slope of the edge changes while the ions are cold but the modulations above the edge only disappear for higher-temperature ions.

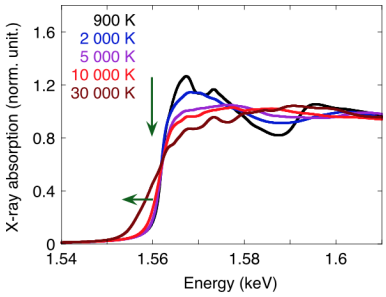

Figure 2.7: Ab initio QMD simulations of Al-K edge XANES spectra, for different (equilibrated) temperatures and solid density. Adapted from [29].

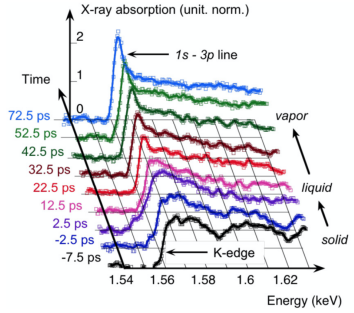

Figure 2.8: Time evolution of XANES near the K-edge for a 100nm isochorically heated Al sample. From [38].

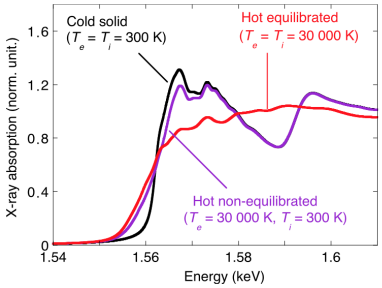

Figure 2.9: Ab initio QMD simulation of Al-K edge XANES spectra for non-equilibrium at solid density. From [29].

2.3.2 Molybdenum

Molybdenum is a transition metal that exhibits significantly different DOS in liquid and solid form and non-equilibrium electronic structure modifications. It is a somewhat close example to Ti, despite the way the DOS changes with excitation, being strongly dependent on which material is being considered. The near Fermi energy structure of Mo is dominated by the behavior of the 4d band which for cold solid conditions is defined by two peaks, one on each side of the Fermi level. The band broadens and flattens for liquid densities and electronic temperatures of a few eV. When the liquid phase expands, a significant downward shift of the Fermi level and the *d* band takes place [29].

The L3 absorption edge of Mo is controlled by the coupling of 2*p* core level states with ones just above E_f [29]. XANES spectra near this edge essentially reveal the occupancy of the dominant 4*d* band. Because of the localization in energy of d electrons, the spectra are expected to be dominated by an absorption line of finite width. This can be seen in figure 2.10 where ab initio QMD simulations of the XANES spectra were performed for equilibrium situations. The line does not change position despite the Fermi level shifting with lowering density because this effect is compensated by a lowering of the 2p levels. As the ab initio simulation approach taken is not possible for core states, this energy shift with density has to be calculated separately.

In non-equilibrium situations, but with well-defined hot electronic and cold ionic temperatures, the Mo DOS remains mostly unchanged [29]. As a result, the absorption spectra present in figure 2.11 are a direct result of electron excitation: the increase in electron temperature promotes some electrons to above E_f, these unoccupied states are responsible for the pre-edge structure that forms with increasing temperature.

In [49], time-resolved XANES measurements of femtosecond laser-heated Mo were reported, along with

the absorption spectra for cold Mo, at 5 ps and 1 ns after heating with $\tau_L = 300$ fs, $F = 4 \times 10^4$ J/m^2, $\lambda_L = 800$ nm laser light at 12$^{\text{o}}$ incident angle. The thermodynamical conditions determined by a TTM model - with the G coefficient of [41] used, suggest thermalization after 2 ps (the density however seems to remain constant for up to $\approx$ 20 ps). At the 5 ps mark, a pre-edge is evident from the data, suggesting that actually thermalization has not been achieved yet and that the e-i coupling coefficient was overestimated.

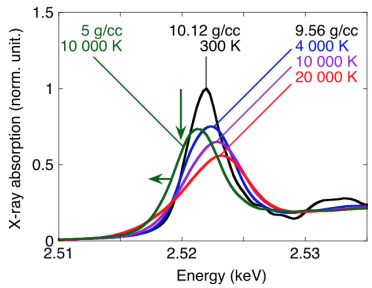

Figure 2.10: Ab initio QMD simulation of XANES spectra for the L3 Mo edge calculated in equilibrium. From [29].

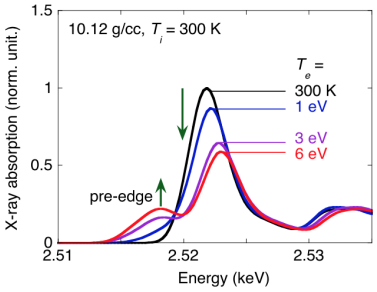

Figure 2.11: Ab initio QMD simulation of XANES spectra for the L3 Mo edge calculated in the non-equilibrium situations, at solid density. From [38].

2.3.3 Long lived non-thermal electrons: Copper

In [50], time-resolved XANES measurements of isochorically heated copper with resource to a $\tau_L = 40$ fs $\lambda_L = 400$ nm laser with a fluence of $F = 3.3 \times 10^3$ J/cm^2 were reported. The probe pulse was sourced from a free electron laser to measure the absorption coefficient at four distinct photon energies, both before and after the L absorption edge. The temporal resolution afforded by the setup was 200 fs.

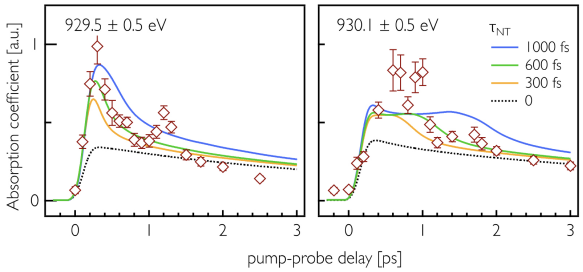

Figure 2.12: Evolution of x-ray absorption at selected energies. Experimental results are compared with calculations for different non-thermal lifetimes τ_{nt}. The experimental results are convoluted with the time resolution. From [50].

The authors first attempted to describe the measured absorption peaks, which remain visible until 1600 fs, with the standard TTM equation 1.20: with G calculated as in [41] and the assumption that the DOS remains the cold one. They found that the calculated peak abated too quickly and shifted rightwards in energy too quickly. To obtain better agreement, between the model and the data, the authors considered two additional effects: the lowering of the d-band energy with an increase in electronic temperature and the non-immediate thermalization of the hot electron population excited by the pump pulse. An effective lifetime approach was taken, allowing the 11 electrons in the $3d$ and $4s/p$ bands, initially excited at a one-to-one rate with the

number of absorbed photons, to gradually transfer to the thermal electron population. The result from the simulations compared to experimental measurements can be observed in figure 2.12. It could be concluded that 500-600 fs provides reasonable agreement with both energies presented.

2.4 Bayesian Inference: tackling uncertainty

Replicating experimental outcomes obtained in controlled settings is the cornerstone of verifying theoretical models against empirical data. The models used for this purpose are called forward models as they rely on a set of inputs (typically related to the experimental conditions) to generate the experimental observables. To process of analyzing the data typically amounts to varying the inputs of the physical forward model until the output matches the experimental data, within its uncertainty. This "fitting" process can be seen as an inversion problem, where we wish to discover the expected value of the input parameters (in general designated **x** and in vector form) from some known experimental data (written as **d**). A scheme illustrating this process is present in figure 2.13.

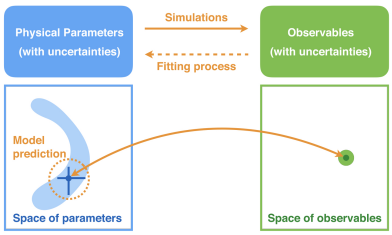

Figure 2.13: The fitting process to compare forward model and experimental data. From [51].

Two main problems arise when dealing with the inversion problem: brute force is intractable, and inversion instabilities exist. The former relates to the dimensionality curse common in all machine learning problems. The brute force approach would entail running different simulations for different combinations of input parameters, typically laid out as a grid in parameters space. As the number of parameters in the model increases, however, the volume of the space that needs to be searched increases even faster, quickly rendering this approach unusable. The latter relates to the forward model being used. In lots of cases, different combinations of input parameters can produce similar outputs (for example when some input parameters are highly correlated with one another), making the inversion problem itself not well defined.

These problems typically plague warm dense matter experiments and models since there are a lot of unconstrained experimental variables (due to the difficulty of creating homogeneous warm dense conditions) that increase the dimensionality of the problem. There are also competing models with high degrees of flexibility and, as such, inversion instabilities.

These shortcomings can be tackled by a probabilistic approach. Instead of the often-used frequentist interpretation, in which probabilistic statements can only be made about random variables occurring in identical repeats of an experiment, a Bayesian interpretation of probability can be used. In this scheme, probabilistic statements are viewed as measures of the plausibility of a given hypothesis, conditional on the truth value of some other information, typically obtained through experiment [52]. Within this interpretation we can write

the Bayes theorem:

$$P(\mathbf{x}|\mathbf{d}) = P(\mathbf{d}|\mathbf{x})\frac{P(\mathbf{x})}{P(\mathbf{d})}. \tag{2.18}$$

Here $P(\mathbf{d}|\mathbf{x})$ is the probability of obtaining a given data set if the input parameters are true, also called the likelihood function, $P(\mathbf{x})$ is the prior distribution of parameters, that encodes prior knowledge about the experiment, such as known physical constraints on the input parameters, and $P(\mathbf{d})$ is the marginal likelihood of the observed data set. The last quantity is treated as a scaling constant since it is independent of $\mathbf{x}$ and is usually hard to calculate. The posterior and the likelihood distributions need to be specified. Finally, $P(\mathbf{x}|\mathbf{d})$ is known as the posterior probability distribution and represents the probability of a given set of input parameters being the true ones, given the observed data and prior knowledge.

The inversion problem can then be solved, even in the face of instabilities or lack of uniqueness, by knowing the posterior probability function, which will give us, for all of input space, the likelihood that a given set of inputs is the right one. The posterior will be wide or multipolar if the forward model can produce similar outputs over a wide range of inputs, reflecting the uncertainties of the model itself that can not be resolved by acquired data, and it will be narrow and well-defined for a model that offers little flexibility on the produced outputs. All there is left now is to specify the prior distribution and how to calculate the likelihood, along with a sampling or approximation method that removes the brute force component of knowing the posterior distribution.

2.4.1 Priors and Likelihood

The choice of prior distribution highly depends on the amount of knowledge previously accrued about a given phenomenon. Oftentimes, however, a situation of relative initial ignorance needs to be tackled. As such, our attention will turn to two types of "uninformative priors", used for two different types of parameters, following a discussion in [52].

A location parameter is always measured against a specified origin and scale, and it can be positive or negative. If we are completely ignorant about the true value of a location parameter, this must be expressed in the probability density function as shift (or origin) invariance, that is $P(\mathbf{x}')d\mathbf{x}' = P(\mathbf{x})d\mathbf{x}$ where $\mathbf{x}' = \mathbf{x} + \mathbf{r}$ and $\mathbf{r}$ is a shift-vector. If the probability density function is defined as $f(x)$, we then have $f(x+r)d(x+r) = f(x+r)d(x) = f(x)d(x) \iff f(x) = \text{constant}$. When hard boundaries on the parameters are known this constant can be normalized to $f(x) = 1/(x_{max} - x_{min})$, otherwise an improper prior - defined up to a normalizing constant - can be used, for parameter estimation.

A scale parameter behaves differently as it is not measured against a variable origin and can only take positive values (e.g., a lifetime parameter). If we are completely ignorant about the scale variable, a shift in the measuring scale of the problem must leave the prior unaffected, which can be written as $P(\boldsymbol{\tau}')d\boldsymbol{\tau}' = P(\boldsymbol{\tau})d\boldsymbol{\tau}$ where $\boldsymbol{\tau}' = \beta\boldsymbol{\tau}$. For a probability density function defined as before, $f(\beta\tau)d(\beta\tau) = \beta f(\beta\tau)d(x) = f(\tau)d(\tau) \iff f(\tau) = \text{constant}/\tau$. If parameter bounds are known we can obtain $f(\tau) = 1/(\tau \ln \tau_{max}/\tau_{min})$, although the normalization is only necessary if Bayesian model selection is required and not for parameter

estimation.

A likelihood function, written as $\mathcal{L}(\mathbf{x}) = P(\mathbf{d}|\mathbf{x})$ to emphasize that $\mathbf{d}$ is fixed by observation, is the joint probability distribution of actually measuring the data $\mathbf{d}$, given that $\mathbf{x}$, i.e, the model inputs, are true. As such, it depends on knowledge about the process being modeled as well as a degree of confidence that the physical model can indeed generate accurate predictions. In the simplest case, the physical model itself is unique and deterministic (as well as the independent variables it depends on). For a given value of the model parameters, then, the measured data $\mathbf{d}$ is not fully determined due only to possible experimental measurement error. Uncertainty about which physical model would correctly describe the phenomena being studied or intrinsic to the forward model itself would not be considered.

The nature of experimental errors in measurements is often approximated as Gaussian noise. Each point in an experimental data set is then obtained by independently sampling a multivariate Gaussian with average value μ_i equal to the true value one wishes to measure and width equal to the level of experimental noise of our measurement apparatus σ_i, where i indexes the different data points that comprise a data set. In a deterministic framework, this "true value" is given by the physical model, with the appropriate parameters, and can therefore be rewritten as a function of the model inputs $\{\mu_i\} \rightarrow \mu(\mathbf{x})$. If the data points are sampled independently (such as when we are dealing with a time series, for example), the joint likelihood function is the product of the sampling likelihood functions for each of the data points:

$$\mathcal{L}(\mathbf{x}) = \prod_{i=1}^{n} \frac{1}{\sqrt{2\pi}\sigma_i} \cdot \exp\left\{-\frac{(d_i - \mu(\mathbf{x}))^2}{2\sigma_i^2}\right\} \Rightarrow \log \mathcal{L}(\mathbf{x}) = \ell(\mathbf{x}) = -\frac{1}{2}\sum_{i=1}^{n}\left(\frac{d_i - \mu(x)}{\sigma_i}\right)^2 + \text{constant} \quad (2.19)$$

where ℓ is the log-likelihood function, often used when computationally sampling.

2.4.2 Markov Chain Monte Carlo (MCMC)

Being able to write down the joint posterior distribution $P(\mathbf{x}|\mathbf{d})$ still leaves the open question of how to acquire knowledge about its general form. Once known, parameter estimation in Bayesian Inference reduces to calculating the marginalized distribution of the posterior over all but one parameter, and knowledge of 2-dimensional correlations is also an exercise in marginalization.

An efficient estimate of the posterior distribution can be obtained through Markov Chain Monte Carlo algorithms. The basic principle consists of creating a random walk procedure of moving through the model input space such that the probability of being in a region of space is proportional to $P(\mathbf{x}|\mathbf{d})$. One, or several, parallel Markov Chains are then employed where the new sample $\mathbf{x}_{t+1}$ dependents on the previous one $\mathbf{x}_t$ through $P(\mathbf{x}_{t+1}|\mathbf{x}_t)$. This often converges to the posterior distribution as $t \rightarrow \infty$ if the chains are irreducible, aperiodic, and reversible (follow detailed balance) [52]. The range of cases for which convergence occurs, and the speed of such convergence (usually measured as the burn-in period or number of ensemble iterations until convergence occurs) is highly dependent on the MCMC algorithm employed.

A commonly used algorithm for sampling posteriors is the Metropolis-Hasting (M-H) [53]:

- Given a current position in input space $\mathbf{x}_t$ draw a proposal $\mathbf{y}$ from a know proposal distribution $q(\mathbf{x}_t|\mathbf{y})$, draw $u \sim \text{uniform}(0, 1)$.

- Calculate $r = P(\mathbf{y}|\mathbf{d}) \cdot q(\mathbf{x}_t|\mathbf{y}) / \left(P(\mathbf{x}_t|\mathbf{d}) \cdot q(\mathbf{y}|\mathbf{x}_t)\right)$
- if $\min(1, q) > u$ then $\mathbf{x}_{t+1} = \mathbf{y}$; otherwise $\mathbf{x}_{t+1} = \mathbf{x}_t$.

One of the common proposal distributions $q(\mathbf{x}_t|\mathbf{y})$ is a multivariate Gaussian centered on $\mathbf{x}_t$ and with a covariance matrix tuned, case by case, for faster convergence. The main problem with this algorithm is the sheer amount of parameters of the proposal distribution that need to be predetermined and the fact that proper adjusting these often requires advanced knowledge of the posterior distribution, such as possible bimodalities of the distribution or regions of high correlation. Without the proposal distribution being shaped to reflect these attributes, the convergence often requires a lot more time steps. [53]

An affine invariant MCMC algorithm was developed by [54] and implemented for *python* by [53], that significantly outperforms the M-H, especially for highly correlated posteriors. It achieves this while not needing any preset parameters to adjust for the proposal distribution. The method involves updating an ensemble of walkers altogether. In the simplest case, a proposal for a walker in the ensemble is generated by the transformation $\mathbf{y} = \mathbf{x}_j + Z[\mathbf{x}_k(t) - \mathbf{x}_j]$, where $\mathbf{x}_k$ is the walker being updated, $\mathbf{x}_j$ is a walker randomly drawn from the remaining ensemble and Z is a random variable drawn from a distribution, usually, one proposed in [54]. A ratio for acceptance of the probability, similar to the M-H one can then be written that ensures the detailed balance condition is fulfilled.

Over time, other affine invariant "moves" or ways to evolve the ensemble of walkers have been developed, more suitable to deal with different posterior distribution topologies and different initializations of the problem. Since they retain the affine invariance (that is, the proposal formula remains invariant to all transformations that preserve planes and straight lines, including translations, rotations, and scale transformations), they can all be expected to perform better than M-H in situations where there are strong correlations between the forward model's parameters.

Figure 2.14 shows the results of an MCMC search, performed with the simple affine invariant move described above, which we will call the "stretch move". The likelihood function is of the form of equation 2.19 was sampled and the toy data set was created from the equation below:

$$f(x) = A_s \cdot \sin(\omega_s x) + A_c \cdot \cos(\omega_c x) \tag{2.20}$$

superimposed on Gaussian noise, drawn from a normal distribution, for each data point. The values used were $A_s = 1$, $\omega_s = 1$, $A_c = 1$, $\omega_c = 3$ with the noise level at 0.5. Equation 2.20 was also used as a forward model when calculating $\mathcal{L}(\mathbf{x})$. The initial ensemble of parameters was drawn from a very narrow distribution ($\sigma = 0.1$), around the global minima.

Theoretically, initialization of the Markov Chain would be more robust if it were well spread out across the credible range of the parameters. Empirically, however, if the function being sampled has several high-probability local minima, there is a significant chance that walkers get stuck for a long time in one of these regions. This can be seen in figure 2.15, where a similar experiment was performed but with parameters initialized randomly over a $[0, 5]$ interval. Comparison between the two sets of results shows a diminished efficiency of sampling in the second case, with walkers initially stuck in local minima, sometimes taking a long time to converge to the known optimal solution. Usually, then, walkers are initiated close to either a known or

estimated robust candidate to global minima [53]. Often prior knowledge can give us good initial estimates, otherwise, optimization algorithms equipped to deal with inversion problem instabilities, are often used.

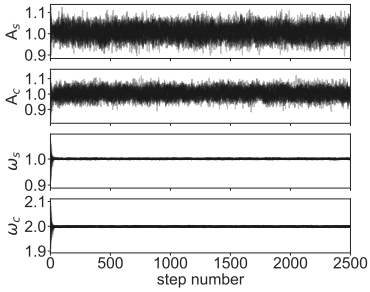

(a) Position of each walker of the ensemble, at a given time step, for each of the free parameters of the model.

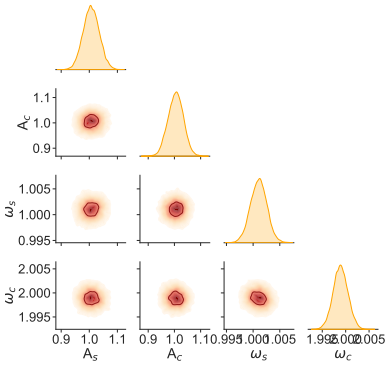

(b) 2D correlations and marginalized posterior distributions of the model parameters. The first 1250 ensemble steps were discarded.

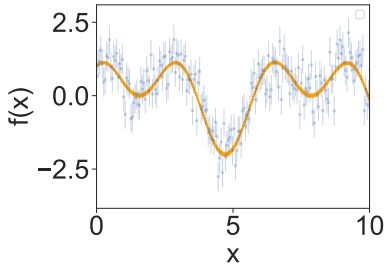

(c) A subset of 100 forward model results using input configurations taken from the ensemble of positions of the walkers with the first 1250 ensemble steps discarded; plotted against the toy data.

Figure 2.14: Results for an MCMC sampling of the likelihood function, using the "stretch move. An ensemble of 40 walkers and a total of 2500 ensemble steps were used. Initialization of the walker was done in a tight ball around the true value.

The chains plotted in figure 2.14a, each representing the path of a different walker of the ensemble, in a given free parameter, are a good example of a sampling that has converged to a stationary state. After an initial burn-in period, the walkers no longer cover new ground but randomly repeat steps in the same region of parameters. Looking to figure 2.14b, the 2D correlations allow us to conclude that the model parameters are uncorrelated from one another. Although in two different length scales, each is allowed to vary in whichever direction from the central estimate, and the other can do the same.

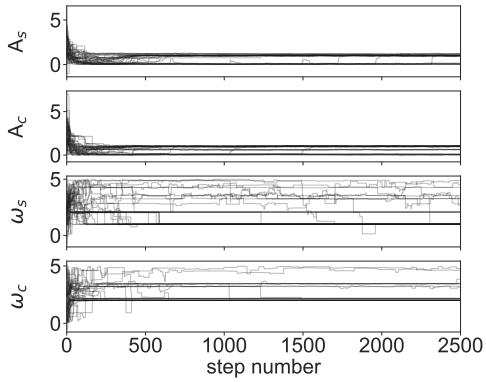

(a) Position of each walker of the ensemble, at a given time step, for each of the free parameters of the model.

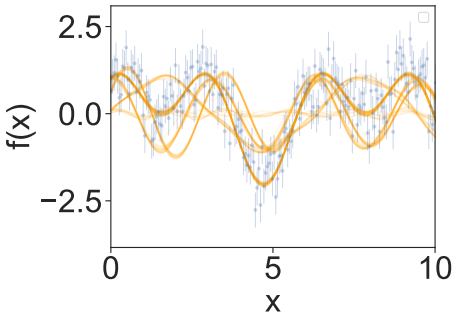

(b) A subset of 100 forward model results using input configurations taken from the ensemble of positions of the walkers with the first 1250 ensemble steps discarded; plotted against the toy data.

Figure 2.15: Results for an MCMC sampling of the likelihood function, using the "stretch move. An ensemble of 40 walkers and a total of 2500 ensemble steps were used.

Chapter 3

Experiment and Data

This chapter aims to describe the experimental process of data acquisition and analysis. Having established the experimental framework that serves as the basis for further data analysis, the rest of the chapter is dedicated to getting us from that raw state to statistically significant data series, with the background effects taken care of as well as an appropriate error estimate.

3.1 Experimental Set Up

The experimental setup is shown in figure 3.1. A Near-Infrared fs laser with wavelength $\lambda_l = 800$ nm, pulse duration $\tau_l = 50$ fs, a spot size of $W_l = (90 - 140)$ μm and a Gaussian spatial profile was used. The initial beam was split using a polarizing beam splitter into a pump (marked IR in figure 3.1) and a probe pulse (marked XUV).

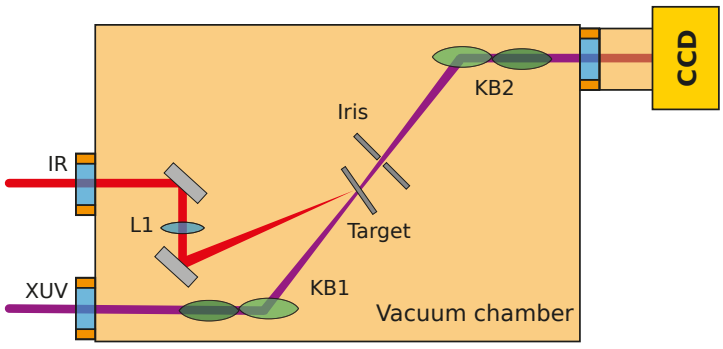

Figure 3.1: The experimental setup. Marked IR is the 800 nm pump laser of variable intensity $\sim 10^{14}$ W/cm^2, while the XUV laser pulse is the probe pulse obtained through HHG, of much lower intensity and with a mean photon energy of 26.2 eV. The target being irradiated is a 100 nm thick Ti foil and the transmitted probe pulse is recorded with a CCD prepared for XUV radiation.

The pump pulse's total energy was varied between 50 μJ and 1 mJ, which represents a range of laser intensities $I_{pp} \approx (10^{13} - 2.5 \cdot 10^{14})$ W·cm^{-2} . The probe pulse was focused onto a gas cell to create an XUV spectrum through HHG. After the HHG gas cell, filters remove any remaining NIR and we are left with an ultrashort XUV pulse.

The HHG process created a low intensity pulse with fluence $F_{pb} = 5$ nJ/cm^2 and pulse duration $t_{pb} = 25$ fs, corresponding to an intensity $I_{pb} = 2 \cdot 10^5$ W/cm^2. As such, this pulse needed to be kept in primary vacuum so that it would not be attenuated by air. The generated spectrum was measured at the exit of KB2, through a slit and gradient combination, and is shown in figure 3.2. Taking into account the several harmonics present, the weighted average of the probe is 26.2 eV.

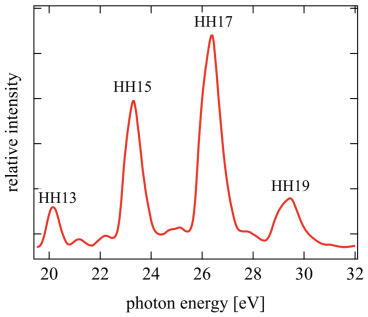

Figure 3.2: The HH spectrum.

Both the pump and the probe pulses were focused onto a thin (100 nm) Ti film, with Kirkpatrick–Baez (KB) mirrors being used for the probe. The spatial imprint of the radiation transmitted through the film was recorded by a CCD with an Al filter that only allows radiation in the (17-80) nm or, approximately, (15.5-73) eV range. Using a translation stage, the optical path of the probe pulse was altered and, thus, the time delay between the arrival of the pump and the probe was indirectly varied. This allowed for the collection of temporal data series composed of several transmitted XUV spatial imprints.

The temporal resolution of the collected data was at best 50 fs due to the probe pulse's duration, while the spacial resolution is constrained by the overall resolution of the system: each pixel of the final image translates to (7×7) μm^2 of the foil.

At the pump intensity range achieved by this setup, the metal ablates away some time after the initial excitation, as was discussed in section 1.5.2. As such, after each shot, the target's position needed to be changed so that a new portion of the film was irradiated. The shot-by-shot nature of the experiment was the main limitation in terms of the number of data points that could be measured.

3.2 Collected Data

For each of the translation stage's position (representing a time delay between the arrival of the pump and the probe to the Ti film) and each of the pump pulse's total energy chosen values (50, 150, 250, 500, 1000) μJ, three different types of images of the transmitted XUV radiation were recorded.

First, an image of just the XUV pulse was taken, shown in figures 3.3a, 3.4a and 3.5a; immediately after, and because the metal did not ablate, both pulses were sent in and a second image was taken - figures 3.3b, 3.4b and 3.5b. A final shot was acquired, with the pump switched off, as exemplified in figures 3.3c, 3.4c and 3.5c. These last ones were designed to image the ablated portion of the metal film, due to the pump sent in the previous shot.

The grid that can be seen in all the acquisitions are images of the support bars for the metal film. The area of each square is (360×360) μm^2. It is not orthogonal due to optical aberrations, namely astigmatism caused by the grazing optics nature of the KB mirrors utilized. The acquired images can have both positive or negative time stamps. It is positive if the pump arrived before the probe, and vice-versa.

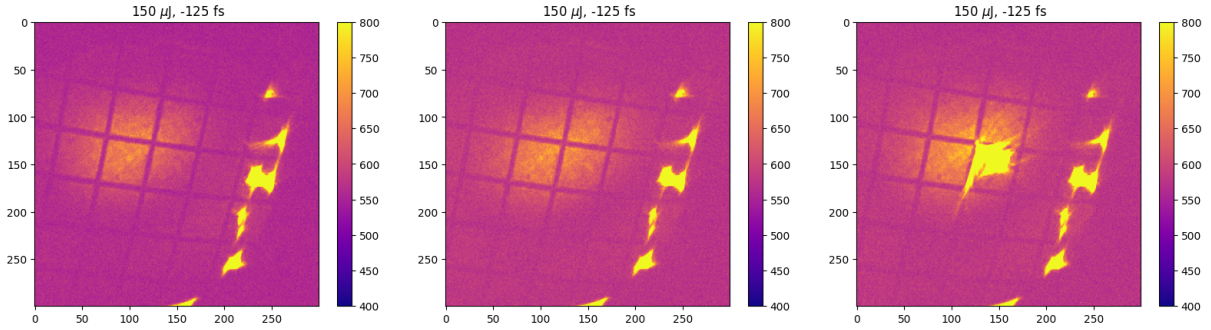

(a) Image of pump and probe signal. (b) Image of pump and probe signal. (c) Image of pump and probe, $t = \infty$.

Figure 3.3: Images of the transmitted XUV radiation. Shots concerning a pump pulse with 150 μJ of pulse energy, at -125 fs of pump-probe delay.

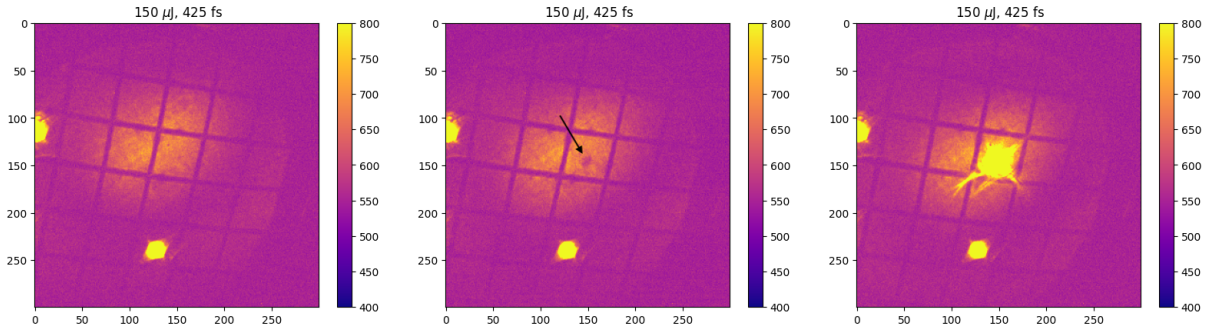

(a) Image of just the probe signal. (b) Image of pump and probe signal. (c) Image of pump and probe, $t = \infty$.

Figure 3.4: Images of the transmitted XUV radiation. Shots concerning a pump pulse with 150 μJ of pulse energy, at 425 fs of pump-probe delay.

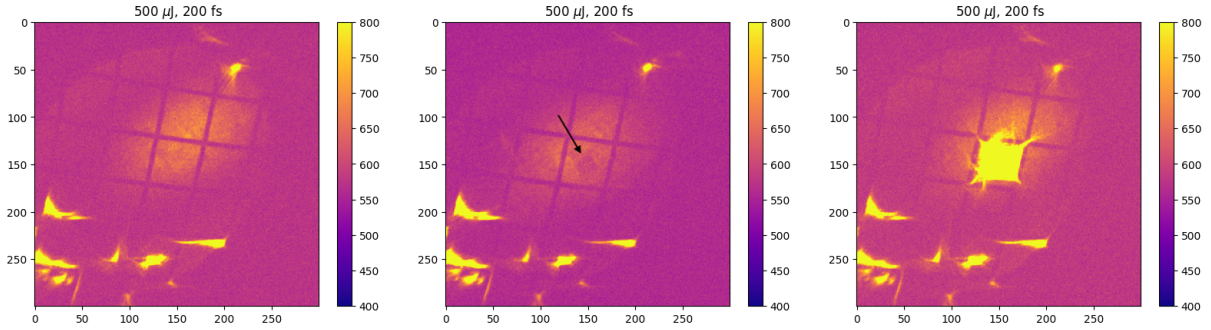

(a) Image of just the probe signal. (b) Image of pump and probe signal. (c) Image of pump and probe, $t = \infty$

Figure 3.5: Images of the transmitted XUV radiation. Shots concerning a pump pulse with 500 μJ of pulse energy, at 200 fs of pump-probe delay.

Analyzing the transition from figures 3.3b to 3.4b, it can be seen that at negative times the pump and probe signal resembles that of the XUV pulse only (figure 3.3a) since the probe was still passing through undisturbed Ti; at positive times, a dip in intensity appears where the black arrow is. It can be concluded that the pumped metal has a lower XUV transmission coefficient, at the probe's energy, than that of the undisturbed sample. It was also observed that at later times this dip gradually becomes less pronounced, specifically in the picosecond regime.

Finally, comparing 3.4 to 3.5, i.e., shots at different pump energies, the same overall feature set can be

observed, and this remains the case for the other temporal series. The main difference between them is the size of the area where the XUV transmission depression occurs, which increases with the total pump energy. The increase in area can also be observed when comparing figures 3.3c and 3.4c to 3.5c; in the latter the area ablated away by the pump is increased. This effect is related to the increase in energy deposited in the sample, which makes the size of the area exposed to laser fluences above the damage threshold increase.

3.3 Feature Extraction

The collected data needed proper treatment so that it could be directly compared to theoretical models. The relative change of the XUV transmission coefficient, from the undisturbed solid to the pumped one, for the different temporal delays, was the desired data set, to be extracted from each of the acquired data series.

The data acquired was spatially resolved, this transmission change was recorded for different absorbed pump fluences in each picture taken. Each CCD pixel in the pumped zone of the metal absorbed a different amount of energy, due to the Gaussian spatial profile of the pump beam. As such, for each data series, we have access to a myriad of temporal responses (of the XUV transmission) that correspond to different conditions of the Ti sample. The amount of data obtained is greatly increased because multiple series were acquired, for different total pump energy.

Since the need for more data, without increasing the number of images acquired, has to be balanced against the need for that data to be statistically significant, only three "spatial regions of interest" were used, whereas in the limit we could use one per pixel. The significantly reduced number of zones chosen has to do with the level of variation in intensity measurements of side-by-side pixels, in a given shot, which indicated high temporal noise levels, attributable to dark current on the CCD.

Taking advantage of the reproducibility of the spatial imprint of the absorbed pump pulse, the three XUV transmission time series that were extracted from each original data series could be categorized by absorbed laser fluence. This approach offers a data expansion opportunity without the need for more data acquisition, while also allowing spatial gradients of the pump and probe to be properly taken into account.

What follows is a detailed description of the steps taken to get from the data presented in section 3.2 to the final desired data sets, three for each acquired data series, in the framework just discussed.

3.3.1 Background removal

CCD Background

The temporal Gaussian noise of our CCD, coming from the dark current, is overlaid by spatial inhomogeneities. To avoid discrepancies in the data due to differences in the location of our pumped area relative to the CCD frame, the averaged background was subtracted from every image. As some of the time series were acquired on different days from the background images, this subtraction did not always result in the average intensity of the dark parts of the CCD (outside the illuminated XUV spot) averaging out to zero. The dark current temporal noise is not immediately corrected by this subtraction but can be estimated from the side-by-side

pixel variations of what should be an almost continuous, if inhomogeneous, background.

In figure 3.6, the yellow points represent line outs of a dark zone of all the shots in a given family. Figure 3.6a concerns a time series of images taken on the same day as the background acquisitions and exhibits the expected and desired behavior of stochastic noise hovering around zero. Figure 3.6b, on the other hand, concerns a time series of images taken on a different day and shows a systematic deviation along with residual spatial variation.

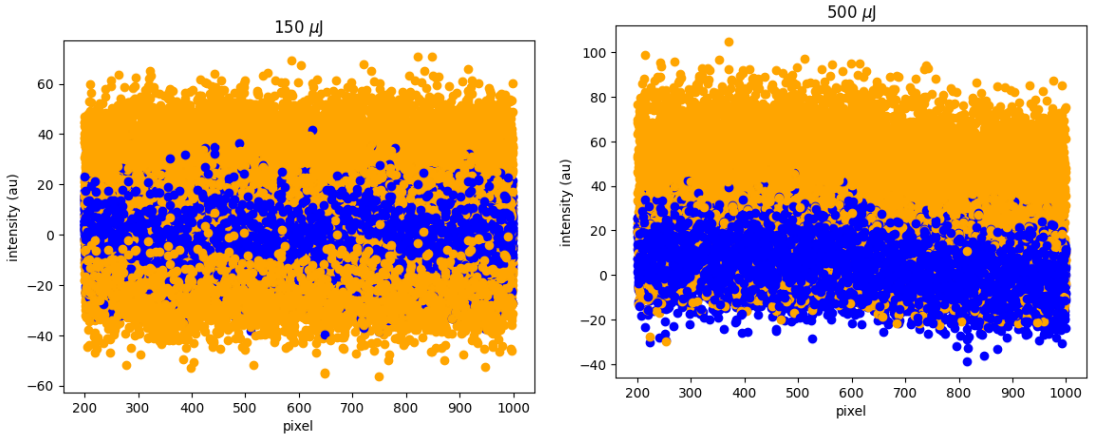

(a) For 150 μJ the dispersion is reduced.

(b) For 500 μJ a systematic deviation is corrected out and the remaining spatial variance is abated.

Figure 3.6: Line outs of a dark part of the CCD image, after subtracting figure the average background. Taken for all the images in a given time series. Yellow points are from before setting the average noise level to zero and blue points are from after.

These deviations needed to be corrected, to be able to compare on an equal footing all the images. To do so, a 200×800 pixels cut-out of the dark zone was used to calculate the average noise level of each image. This level was subsequently subtracted from every pixel in every image. A lineout of the result, again in a dark region, is shown as the blue points in figure 3.6. Figure 3.6b shows reduced spatial systematic variance and an average level closer to zero for the blue points, compared to the yellow, as desired. Both figures also show a reduced spatial variance of the blue points, also a positive effect for ease of comparison between different time series and, in this case, even for different shots of the same family.

Spatial Features Background

From figures 3.3 to 3.5, it became apparent that besides the zone with the transmission dip, which will be called zone of interest, several other spatial features are present in each image. Since the film is 100 nm thick, slight tears can appear causing bright spots; over big enough length scales the probe pulse's spatial shape becomes visible; and, since the same film is used more than once, other ablated zones might also be present. Properly defining and zooming in on the zone of interest was then a necessary next step to keep the relevant information of each picture only.

To do so, all the superfluous information was disposed of, i.e., the zones away from the one of interest were cropped. A square region was used to define what pixels would be kept, with sizes ranging from (25×25) pixel to (40×40) pixel, increasing with increased total pump energy of the laser. The increase in area mimics

the size of the area of interest, which varies similarly. The center of the square region was defined by user click, approximately in the middle of the hole visible in the $t = \infty$ shot.

As previously ablated zones are also present, for every time step in our time series we compare the pumped and probed shot to the $t = \infty$ acquisition, to discover the new bright spot that appears from the latter to the former. The $t = \infty$ acquisition was, then, important to remove ambiguity and serve as an independent indicator of the true position of the pumped region of the sample. This was especially significant for negative time shots and shots in the several picoseconds, as in both of these cases the signature of the pump in the pumped and probed images becomes faint to indistinguishable.

Figures 3.7 and 3.8 exemplify the obtained results after cropping. They also show the increase in area of the zone of interest with a depressed XUV transmission coefficient, for higher pump energies.

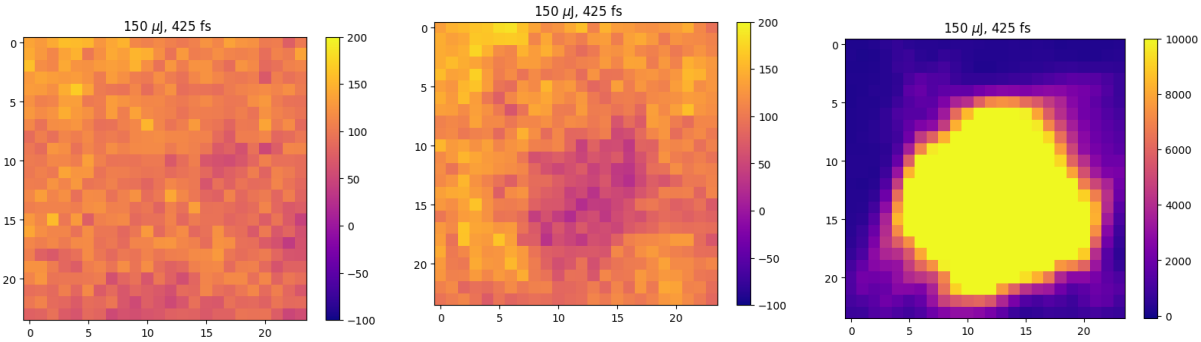

(a) XUV only shot.

(b) Shot probed with and XUV pulse and probed with a NIR pulse.

(c) Shot at $t = \infty$.

Figure 3.7: 25×25 zoom in of XUV transmission images concerning a pump pulse with 150 μJ of pulse energy, at 425 fs of pump-probe delay.

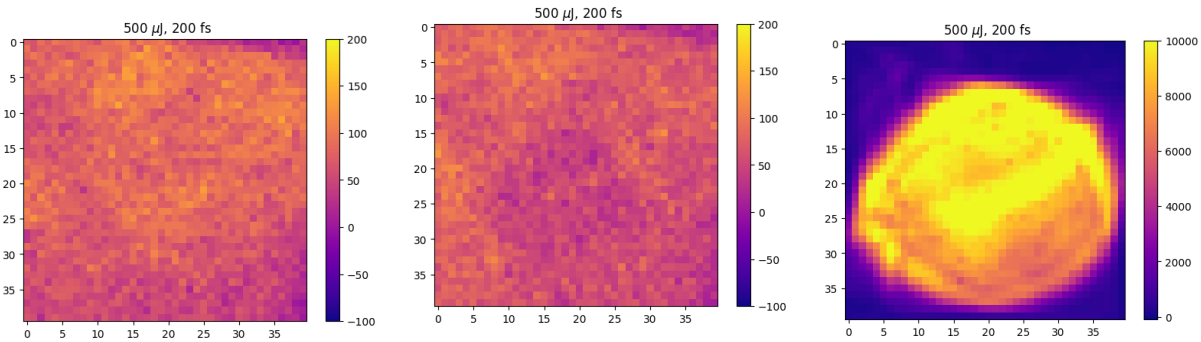

(a) XUV only shot.

(b) Shot probed with and XUV pulse and probed with a NIR pulse.

(c) Shot at $t = \infty$.

Figure 3.8: 40×40 zoom in of XUV transmission images concerning a pump pulse with 500 μJ of pulse energy, at 200 fs of pump-probe delay.

To unambiguously define the zone of interest, we turned to figures 3.7c and 3.8c. The ablated area could be defined as the zones where the CCD counts are significantly higher, i.e. where the XUV pulse of the $t = \infty$ acquisition, is not attenuated by the Ti film. To obtain matrices, or masks, like the ones shown in figure 3.9 (ones inside the zone of interest and zeros outside) a threshold method was applied.

Pixels above the threshold values were put to one, while all others were kept at zero. For the 50 μJ and

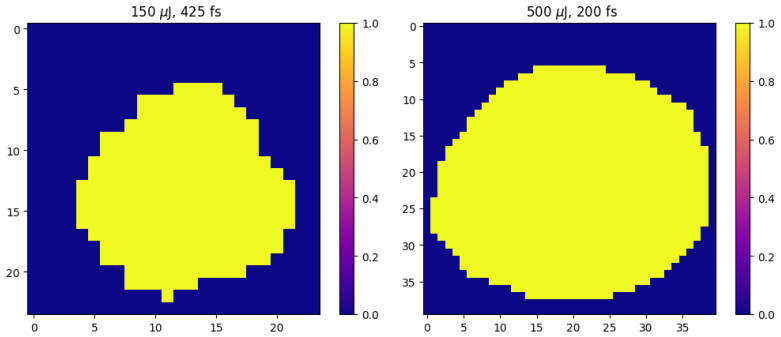

Figure 3.9: Masks of the zone of interest, obtained with a threshold method. Pixels set to one correspond to ablated regions, that went through a warm dense state while pixels set to zero correspond to regions that remained solid Ti. Based on the zoomed-in shots at $t = \infty$.

150 μJ series, the threshold value was chosen as the average of all pixels in the image, $th = av$. As the size of the ablated region of the sample grows, however, refraction patterns of the XUV radiation imaging it also do so. The condition was then slightly relaxed to $th = av - 500$ for the 250 μJ series and $th = av - 1500$ for the 500 μJ and 1000 μJ series. The values were chosen as the ones that maintained an approximately circular area of interest, throughout the series.

Thermal Self Emission signal

For shots taken at higher pump energy, i.e, at 500 μJ and in a more pronounced manner for 1000 μJ, a spatially non-homogeneous signal appears in the pumped and probed shot that does not appear in the one that is only probed, as shown in figure 3.10. This was attributed to plasma self-emission, which for sufficiently high temperatures (achieved for higher deposited energies) emits a non-neglectable portion of its thermal radiation in the UV regime.

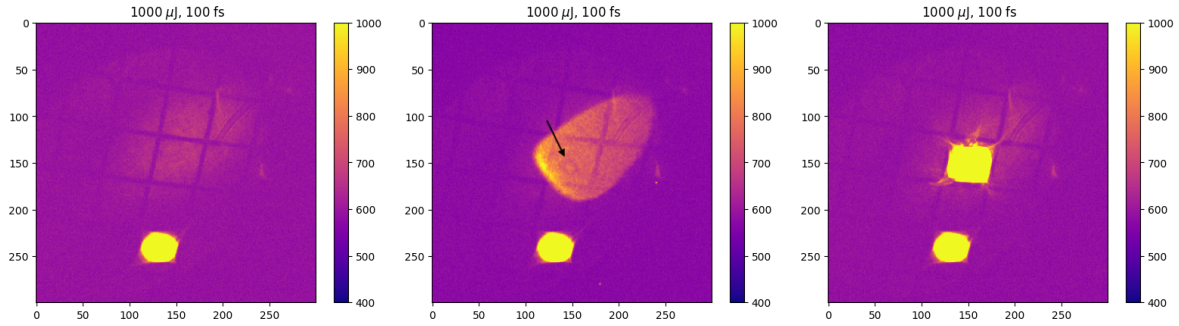

(a) XUV only shot. (b) Pumped and probed shot. (c) Shot at $t = \infty$.

Figure 3.10: Images of the transmitted XUV radiation. Shots concerning a pump pulse with 1000 μJ of pulse energy, at 100 fs of pump-probe delay.

The presence of this signal pollutes the desired measurement, i.e., the relative XUV transmission coefficient, both by affecting different zones of the plasma differently and by not being present in the benchmark (probe only) shot. It was therefore necessary to correct for it.

It was impossible to acquire the shape of the signal without the transmission dip, for non-negative times,

since the thermal signal is created by the pump. As for the negative time acquisitions, there are few of them and the existent ones are subject to significant noise fluctuations. The averaging of those signals was also made difficult by the different positions of shots of the same family, relative to the supporting grid. A different method for estimating the self-emission signal was, as such, needed. We took an approach relying on the fact that the thermal emission signal is, spatially, much larger than the XUV dip, thus varying little inside the zone of interest. For the zoomed-in versions of the images, as in figure 3.15a, the thermal emission can be approximated by a slanted plane.

The thermal emission's imprint was then corrected for by employing a 2-dimensional least-squares regression (using *sicpy*'s *curvefit* [55]) of the probed-only image to the expression:

$$S_{pb}(t) = S'_{pp}(t) - (a \cdot x + b \cdot y + c) \tag{3.1}$$

where $S_{pb}(t)$ is a matrix containing the pixel-by-pixel counts of the acquired probe-only images corrected for the background and zoomed in, for a given time delay t, and $S'_{pp}(t)$ is a similar matrix but for the pumped-and-probed images (named pumped image from now on). The x and y are coordinate matrices, i.e, each row of x and each line of y are composed of vectors with all coordinates set to that row/line count. The shape of the coordinate matrices is the same as that of $S_{pb}(t)$ and $S'_{pp}(t)$.

The only regions of the zoomed-in shot where the slanted plane correction was expected to bring the pumped-and-probed shot to approximately the same as the probed-only one were outside the pumped zone of interest. And, so, the fit was only performed there, i.e., for the pixels marked zero in the matrices like the ones in figure 3.9. Since the estimate of the thermal emission spatial profile was required to be unbiased relative to the drop, this is a desirable feature as well, not just a necessity.

For consistency, the correction was applied for all time series, even the lower energy ones, where no significant self-emission signal was observed. Some representative results of the described algorithm can be seen in figures 3.11 and 3.12. The overall trend is represented there with significantly larger and less spatially homogeneous corrections for the higher pump energies.

With the thermal radiation corrected for, $S_{pp}(t)$ is defined as the matrix of the pumped image, zoomed-in, corrected for all the effects discussed so far, namely the CCD fluctuations and the thermal emission signal, for a given time delay t.

3.3.2 Subdividing the zone of interest

To fully take advantage of our spatial resolution, the zone of interest was subdivided into multiple sub-zones. Since a significant experimental constraint was the need to alter the region of the film being hit (shot-by-shot acquisition), this allowed for the increase in the number of time series by a factor equal to the number of sub-zones, without the need for more experimental beam-time. For the noise levels of the acquired data and the overall size of the zone of interest, consequence of the CCD spatial resolution, a division into three sub-zones was judged appropriate.

The main hurdle of dividing the zone of interest was related to the fact that, from image to image, even in

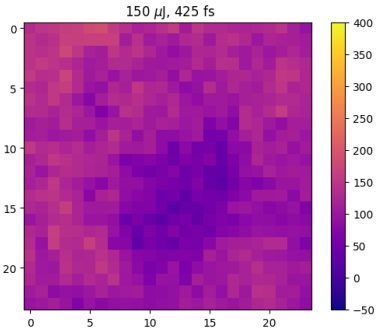

(a) Area of interest uncorrected for thermal emission S'_{pp}.

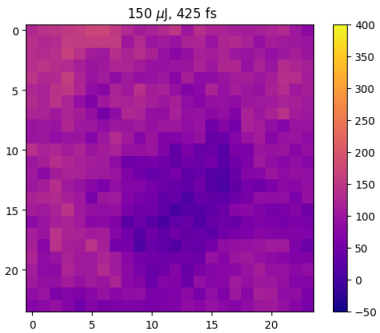

(b) Corrected area of interest S_{pp}.

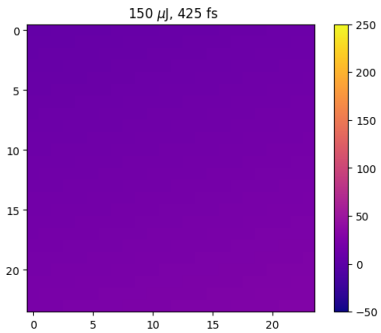

(c) Correction plane $a \cdot x + b \cdot y + c$.

Figure 3.11: Correcting pumped shots for thermal emission, 150 μJ series at t=425 fs, by fitting expression 3.2 to the unpolluted XUV-only shot.

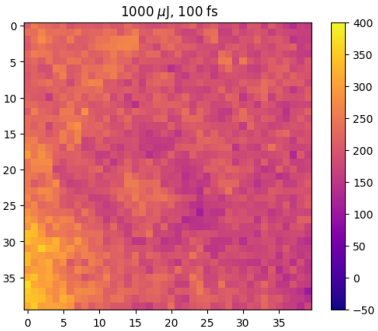

(a) Area of interest uncorrected for thermal emission S'_{pp}.

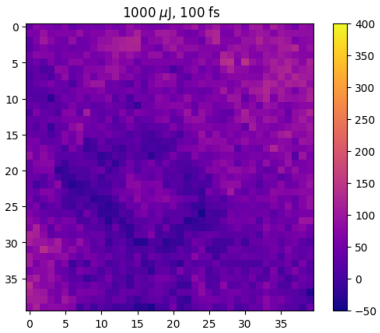

(b) Corrected area of interest S_{pp}.

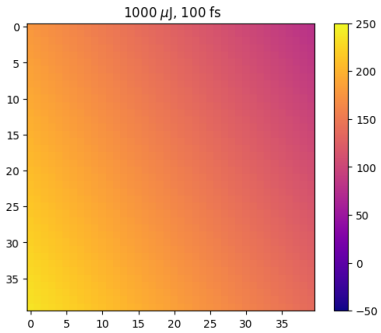

(c) Corrected are of interest S_{pb}

Figure 3.12: Correcting pumped shots for thermal emission, 1000 μJ series at t=100 fs, by fitting expression 3.3 to the unpolluted XUV-only shot.

the same time series, the depression in transmission moves from ine place to another and it also moves relative to the geometric center of the defined area of interest. To accurately track the center of the depression, a new 2-dimensional least-squares regression was performed, using the same least-squares regression method as before [55], for each shot in all the different time series. The lower and higher energy time series were fitted to different expressions since the shape of the depression was observed to be changing from a connected shape to a "ring" one.

For the lower energy series (50 to 250 μJ), the pumped image was fitted to an expression of the form:

$$\begin{gathered} S_{pp}(t) = S_{pb}(t) \cdot (1 - A \cdot \exp[a \cdot (x - x_0)^2 + c \cdot (y - y_0)^2 + b \cdot (x - x_0) \cdot (y - y_0)]) \\ \text{and } a = \frac{\cos^2(\theta)}{2\sigma_x^2} + \frac{\sin^2(\theta)}{2\sigma_y^2}, b = -\frac{\sin(2\theta)}{4\sigma_x^2} + \frac{\sin(2\theta)}{4\sigma_y^2}, c = \frac{\sin^2(\theta)}{2\sigma_x^2} + \frac{\cos^2(\theta)}{2\sigma_y^2} \end{gathered} \tag{3.2}$$

with x_0 and y_0 the center of the transmission depression, which was assumed to be a two-dimensional Gaussian overlapping the probed-only image. The other parameters control the spatial features of the Gaussian and thus their particular numerical values are not of interest. Figures 3.13a and 3.13b show representative results of this least-squares fit, where good agreement was found between the zoomed-in and corrected data and the reproduction based on the best fit of the expression 3.2 to the same data. This fact provides confidence in

the estimation of the center coordinates.

As for the higher pump energy series (500 and 1000 μJ), the pumped image was fitted to an expression of the form:

$$S_{pp}(t) = S_{pb}(t) \cdot \left[1 - \left(\frac{(x-x_0)^2 + (y-y_0)^2}{A^2} + b\right) \cdot \left(\exp\left[-\frac{(x-x_0)^2 + (y-y_0)^2}{2\sigma^2}\right]\right)\right] \tag{3.3}$$

where x_0 and y_0 are, again, the desired center coordinates. This function was designed to smoothly parameterize, without too many degrees of freedom, the transition from a Gaussian-shaped hole to a shape with a smoother top and eventually a "ring" shaped depression. It was also required that the function varies between 0 and 1 and to be asymptotically 1 when $r \to \infty$. The variable b controls the intensity of the depression and its center, while σ approximately controls the overall ring radius and A approximately controls the intensity at the center of the ring. Again, the accuracy of the signal replication only mattered in so far as it improved the accuracy of the center point estimation, and the other parameters' numerical values were not of use.

The flat top behaviour of 3.3 can be made out in figure 3.14b and its ring-like behavior in figure 3.15b. In both cases, with adequate agreement to the corrected experimental data in figures 3.14a and 3.15a, respectively.

Both equations 3.2 and 3.3 still had significant amounts of parametric freedom and, so, when fitting with them there is a risk of convergence to a local minimum, which in this case could be some change between S_{pb} and S_{pp}, other than the transmission depression being studied, due to noise fluctuations. To prevent this, the center coordinates were constrained to remain inside this zone of interest.

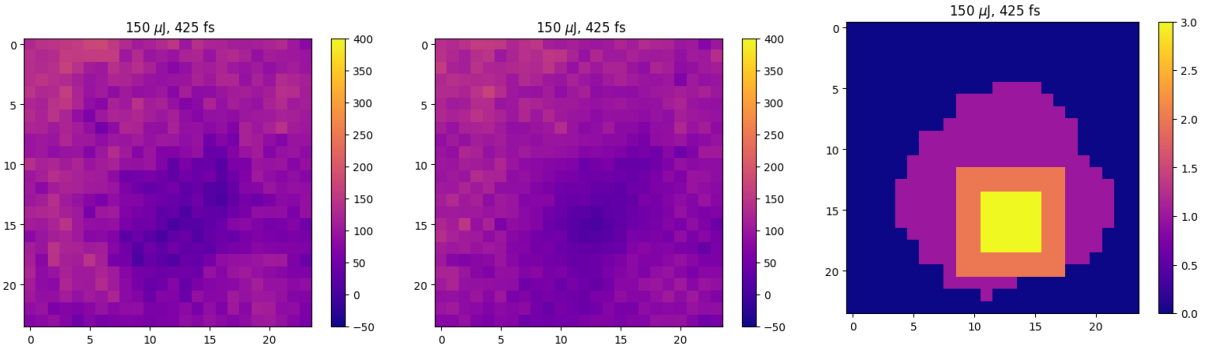

(a) Corrected area of interest.

(b) Fit to 3.13a with equation 3.2.

(c) Desired division of the zone of interest.

Figure 3.13: Subdividing zone of interest, 150 μJ series at t=425 fs. 3 different zones are defined, after the center of the pulse is found, based on a fraction of the radii of the total zone of interest, defined in figure 3.9.

For sufficiently negative times in a given temporal series and for very long times, ≈20 ps, there is no discernible depression. As a result, the fit could not be expected to result in the proper center coordinates. Since the center point could not be better chosen by hand, due to the same problem, it was defined, for each of these images, as the center of mass of the area of interest.

With the center coordinates of the depression uniquely determined for all temporal times stamps, in each data series, circular and concentric subdivisions of the zone of interest could be drawn, for given radii values

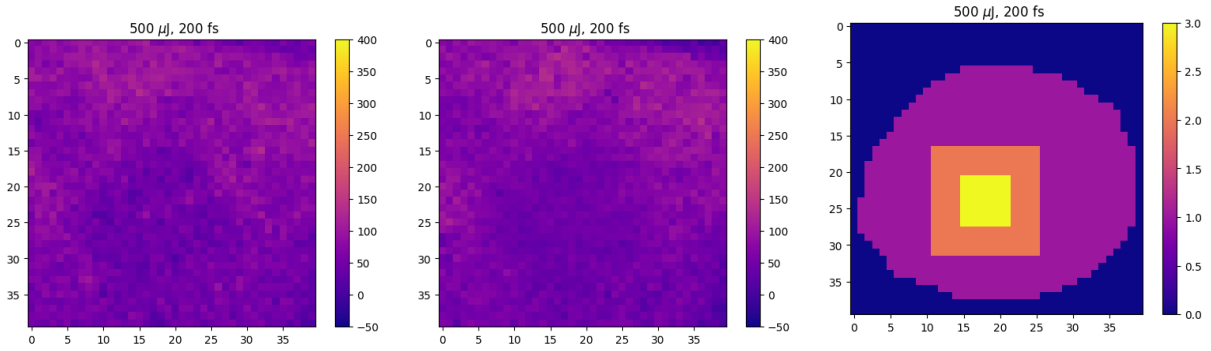

(a) Corrected area of interest. (b) Fit to 3.14a with equation 3.3. (c) Desired division of the zone of interest.

Figure 3.14: Subdividing zone of interest, 500 μJ series at t=200 fs. 3 different zones are defined, after the center of the pulse is found, based on a fraction of the radii of the total zone of interest, defined in figure 3.9.

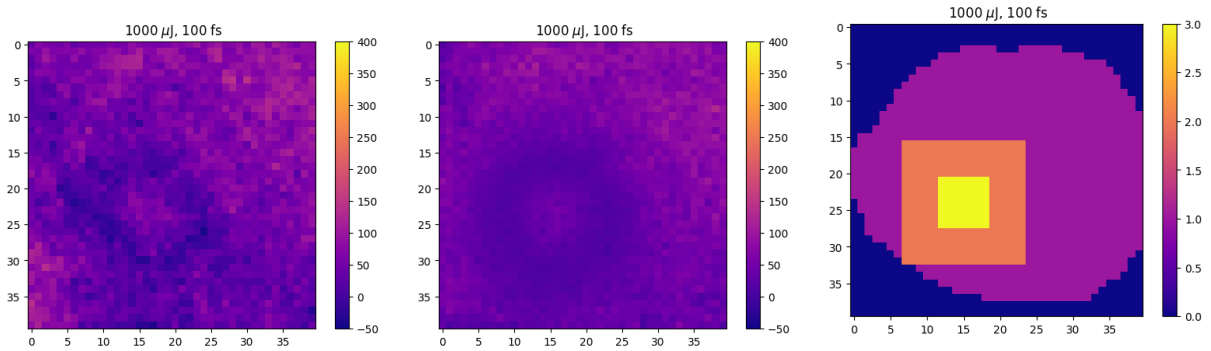

(a) Corrected area of interest. (b) Fit to 3.15a with equation 3.3. (c) Desired division of the zone of interest.

Figure 3.15: Subdividing zone of interest, 1000 μJ series at t=100 fs. 3 different zones are defined, after the center of the pulse is found, based on a fraction of the radii of the total zone of interest, defined in figure 3.9.

defining two inner zones. These values were calculated as a fraction of the radii of the zone of interest. As such, the radii of the sub-zones vary from image to image, in the same series, just as the radius of the overall zone of interest. These differences, however, are not more than one to two pixels inside the same temporal data series, while being considerably larger for different series. The fraction of the total radii used was manually adjusted, between different series, to guarantee that the area of the sub-zones did not differ too much, which was important for statistical experimental error determination, described in section 3.4.

In figures 3.13c, 3.14c and 3.15c, examples of the resulting subdivisions can be seen. While the size of the outer zones changes significantly, along with the size of the ablated zone, the inner zone's size changes much less. In the case of the 1000 μJ series, the inner zone roughly corresponds in size and location to the bright spot in the center of the transmission depression and the middle one to the darker ring surrounding it.

3.4 Results

With the zone of interest properly located and subdivided and with the $S_{pp,E}$ and $S_{pb,E}$ matrices corrected for the different spatial background effects (here the subscript E refers to the total energy of the pump pulse used

in the corresponding data series), the calculation of the relative transmission for each zone could be tackled. This was done by a straightforward calculation of the form:

$$T_E(z,t) = \sum_{(i,j)\in z} \mathrm{S}_{ij}^{\mathrm{pp,E}}(t) \Big/ \sum_{(i,j)\in z} \mathrm{S}_{ij}^{\mathrm{pb,E}}(t) \tag{3.4}$$

where $T_E(z,t)$ represents the relative (to the probe only image) XUV transmission of zone z, indexed by its temporal series' pump energy E and relative position of the sub-zone being calculated ($z = \{\text{inner, middle, outer}\}$), at a time delay between the pump and the probe t. The sum was performed pixel by pixel, subject to the restriction that they belong to the appropriate sub-zone.

Due to averaging out of the CCD background noise, a "dark" pixel in the CCD can now result in a negative intensity, as can be seen by the lineouts of dark regions in figure 3.6. This would have had a perverse effect on the expression above. In the cases where the dip in transmission being studied is more intense, numerical values below zero would appear and artificially reduce the transmission value. To correct for this effect, every time expression 4.1 was applied, a search for the minimum value of $\mathrm{S_{pp}}$ in the overall zone of interest was performed. If the minimum was below zero, a correction of the form: $\mathrm{S_{pb}} = \mathrm{S_{pb}} - m$ and $\mathrm{S_{pp}} = \mathrm{S_{pp}} - m$, where m is the minimum, was applied to the data matrices, before calculating $T(z,t)$ with expression 4.1.

The data series, resulting from the described process, are shown in figure 3.16, along with trend lines calculated as the moving average with a window size appropriate to each series. The error bars that are present only differ for the different zone positions, remaining the same for different temporal series. They are meant to encapsulate the random errors and as such were estimated statistically by:

- searching through every time stamp in every series and singling out the cases where three or more measurements were taken for the same timestamp;
- for each of these time stamps, three standard deviations of the data sampled were taken - one for each of the defined sub-zones;
- an average overall all standard deviations for the inner, middle, and outer zone was taken, resulting in 3 different error measures (inner: ± 0.06, middle: ± 0.04, outer: ± 0.03).

The tagging of the series with the total pump energy and spatial position of the sub-zone is, however, not useful, since they do not properly encapsulate the physical information needed for a forward model to simulate our data sets. As such, the average absorbed fluence on each sub-zones was calculated by reconstruction of the spatial profile of the laser and knowledge about the ablation threshold from multi-pulse ablation studies on Ti with an 800 nm 40 fs laser pulse [56].

As the measurements were taken a few days apart, the waist of the laser possibly changed from series to series. Changes in the aperture of the pump beam also contributed to this effect. To quantify such changes, an inverse problem was solved, consisting of determining the waist, w, of the pump laser pulse that would create an ablated zone equal in area to the average area of the zone of interest of a given series. The ablation threshold, measured as an absorbed fluence, was reported in [56] to be $F_{th} = (74 \pm 13)$ mJ/cm^2. Their central

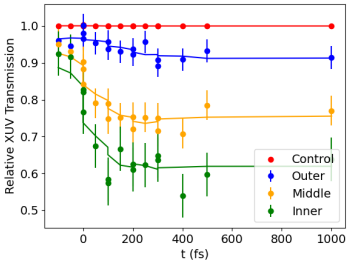

(a) 50 μJ family of data series.

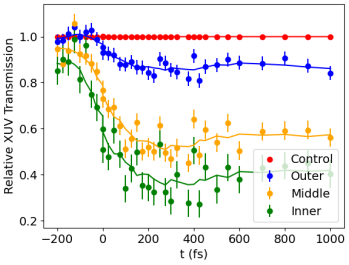

(b) 150 μJ family of data series.

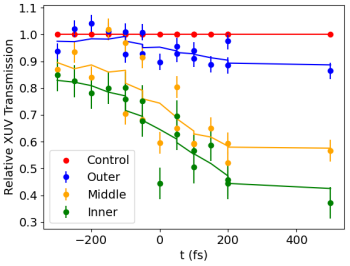

(c) 250 μJ, first family of data series.

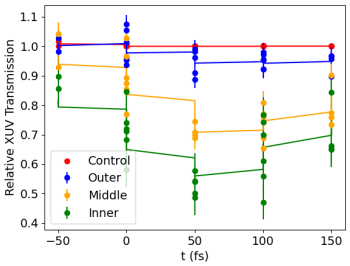

(d) 250 μJ, second family of data series.

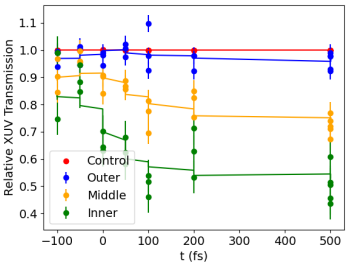

(e) 250 μJ, third family of data series.

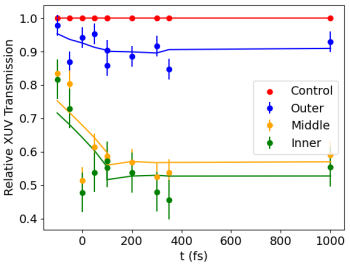

(f) 500 μJ family of data series.

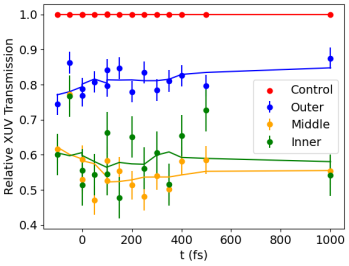

(g) 1000 μJ family of data series.

Figure 3.16: Relative (to probe only) transmission, as a function of time, calculated for all the sub-zones of all the acquired series (with varying total pump energy). Data showed up to 1 ps pump-probe delay. Laser pulse peaks at 0 s.

estimates, along with the knowledge of the pump's total energy, were used to construct a spatial profile of the absorbed laser fluence, assumed to be shaped like a radially symmetric Gaussian function:

$$F_i(w, E, x_0, y_0) = A(E) \cdot \exp\left[-\frac{(x - x_0)^2 + (y - y_0)^2}{w^2}\right] \tag{3.5}$$

where $A(E) = E_{pp} \cdot N \cdot R$ and N is the normalization constant of a similar Gaussian function with magnitude one, E_{pp} is the total absorbed energy of the pump pulse, and $R = 0.558 \pm 0.001$ the measured reflectivity of the sampling.

For every temporal series, the laser waist size, at the film plane, (w) was determined from the average radii of our overall zone of interest. This amounted, computationally, to a process of discreetly varying w and using expression 3.5 and F_{th} to determine, for each w value, the ablated area's radius and keeping the one closest to the experimental averaged value. In table 3.1 w, defined as the distance where the laser intensity falls to I_0/e^2 in the Ti film plane, of each data series is shown.

Zones	50 μJ	150 μJ	250 μJ, 1st	250 μJ, 2nd	250 μJ, 3rd	250 μJ, 1th	500 μJ	1000 μJ
w (μm)	60	44	44	73	70	70	77	80

Table 3.1: Average w (where intensity decays to I_0/e^2) of the laser taking, in the Ti film plane, for each of the data families.

Using expression 3.5, it was possible to calculate a spatial average of the absorbed fluence by each of the sub-zones of each series. Since average radii values of the sub-zones in a given series were used, each temporal series of a single sub-zone is stamped with a unique "data tag".

In figure 3.17, the same series as presented before in figure 3.16 are shown, now organized by average absorbed laser fluence, a meaningful physical parameter. The series with similar average absorbed fluence were grouped for better understanding, as in total there are 21 different temporal series, each referring to a different sub-zone, i.e., a different fluence and final state.

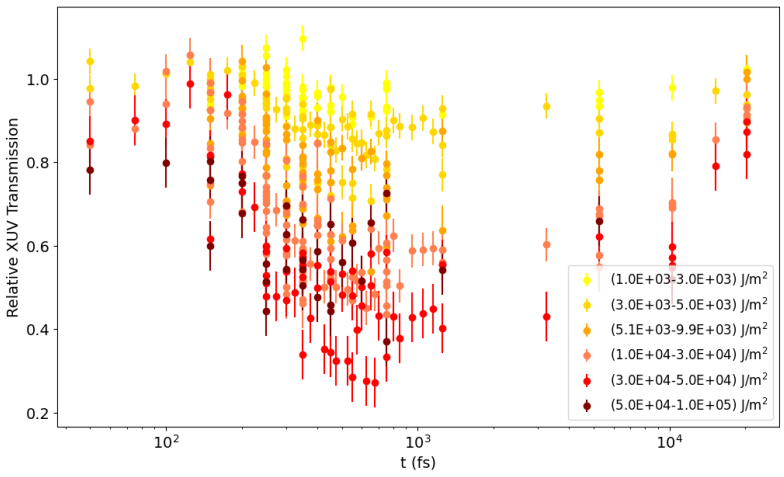

Figure 3.17: Relative (to probe only) transmission, as a function of time, grouped by absorbed fluence of the respective sub-zone. Laser pulse peaks at 250 fs. Log scale.

In the plot the initial drop in the XUV transmission coefficient can be seen, approximately at the same time as the laser is peaking (t=250 fs), with a possible small delay relative to the pump pulse, to positive times. This was interpreted as the fast electronic response to the laser pulse of the electrons in the skin depth of the material, as discussed in section 1.5. In general, it can be concluded that the higher the absorbed fluence, the higher the XUV opacity (lower transmission coefficient), with the notable exception of the higher fluence group, exemplifying the "ring" effect discussed in section 3.3.2. After the (200-300) fs mark, there is stabilization and even a slight recovery of the transmission.

The picosecond response can also be observed, with all the data collected plotted, i.e., up to t=20 ps, depending on the series. Given it takes picoseconds to be noticeable, this trend is necessarily ionic. Since the probe pulse was XUV and, thus, only sensitive to changes in the electronic distribution, this response can be identified with the release of thermal energy from the electronic to the ionic population. In this regime, the XUV transmission coefficient can be seen to recover along a similar time scale for all the fluence groups, with its value approaching the cold measurements in all cases.

3.5 Summary and Conclusions

- Using XUV light to image a thin, solid-density plasma, we can spatially resolve areas of different conditions and thereby access a range of conditions in a single acquisition (shot);
- By correct selection of the XUV photon energy to match energy levels, we can access the bound-to-free transitions in titanium, thereby probing the free electrons as they are heated;
- Several 2D data series were acquired for different total laser energies;
- The spatial imprint of the pulse laser was divided into 3 sub-zones of interest, for each shot;
- The final extracted data corresponds to these three sub-zones, for the different total energies of the pump pulse;
- These sub-zones can be tagged by average incident fluence, on that sub-zone, after a correction to the total laser energy of each shot, obtained from the damage threshold and the ablated area.

Chapter 4

Algorithms, Results and Discussion

This chapter will be dedicated to two different physical models developed as forward simulations of the experimental setup described in the previous chapter. That is, they aim to get to the physical observable - the data series of figure 3.17 - from experimental inputs.

We will start with the TTM initially developed and well-suited for simulating e-i energy exchange while using macroscopic energy conservation considerations to model the absorption of the NIR laser energy by the target. The second model employed does not consider e-i energy exchange but does use a detailed light absorption mechanism, in this case, IB. The absorption of energy is, then, not ad hoc but based on microscopic rate equations, as shall be described in detail.

4.1 Forward Modelling the Relative XUV Transmission

Both physical forward models used rely on calculating the electronic distribution function $f(\mathbf{k}, \mathbf{x}, t)$, in different ways. From that point onward, an estimation of the relative to cold XUV transmission can be reached based on the spectral HHG profile - represented in figure 3.2 -, the knowledge of $f(\mathbf{k}, \mathbf{x}, t)$, and the DOS for Titanium - $D(k)$. Here, we approximate the latter by its cold values calculated from DFT, with the VASP package [57–61]. The cold DOS approximation is justified as long as only the electrons are significantly excited, as is patent in the results from figure 2.3, where little change is reported near the Fermi energy, for excited electrons and cold ions.

A schematic representation of the pumping and probing process, complete with the electronic distributions and the cold DOS of Ti, is present in figure 4.1. The only allowed transitions, at the probe pulse's average energy, are the $3p \rightarrow$ continuum ones. Since the probe is of low intensity, linear response theory applies and we can assume the absorption cross section to be of the form of equation 2.6. Crucially, $\sigma_{\mathbf{k}} \propto (1 - f(\varepsilon_{\mathbf{k}}))$ and the electric dipole term remains approximately constant for the different excitation levels of the electronic population in the cold DOS. As such, the variation in time of the absorption of the probe is, to first order, dependent on the distribution function of the pumped continuum electrons.

As the $3p$ core states are very localized in energy, the pump will induce electronic transitions to the

continuum with an energy distribution in the shape of the HHG spectrum (figure 3.2). This happens because the number of XUV-excited electrons that transition to the continuum is proportional to the intensity of the radiation (linear response regime), at a frequency matching the energy gain of those electrons. The transitions will only be allowed if there are free continuum states for the core electrons to occupy, according to the Pauli exclusion principle.

The absolute energy levels the XUV-excited electrons will try to occupy in the continuum are difficult to pinpoint, since the absolute energy difference between the core state ($3p$) and the beginning of the continuum (or, more practically, between the core state and the Fermi energy) is hard to estimate, in a DFT framework. This is due to a different treatment being applied to the core states, whose properties are usually obtained through separate atomic code simulations and fed to the DFT. The energy levels that the probe-induced transitions are trying to occupy in the continuum will, therefore, span a range of possibilities. Two different factors allow us to pace bounds on this parameter space.

First, the fact that the data sets, for all excitation fluences, show a drop in transmission, recovering only in time scales compatible with electronic cooling, confirms that, on average, the harmonic spectrum transitions must excite electrons to states below the Fermi energy. Note that a decrease in the relative transmission is equivalent to a proportional increase in abortion, as XUV reflectivity remains roughly constant in the conditions studied here. Given that the absorption of XUV photons increases while the continuum electrons are being excited, we can conclude that, over time, more empty spaces became available for the core electrons to transition to, meaning that, on average, they reached a zone in the continuum that gets depleted by electronic excitation.

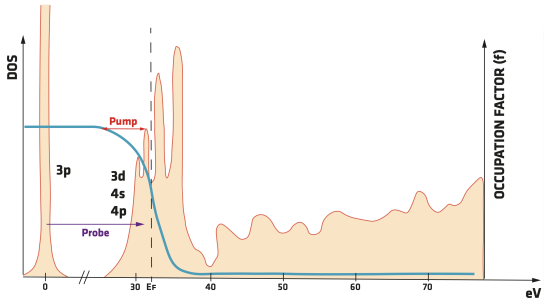

Figure 4.1: A schematic representation of the pumping and probing process complete with the electronic distributions and the cold DOS of Ti.

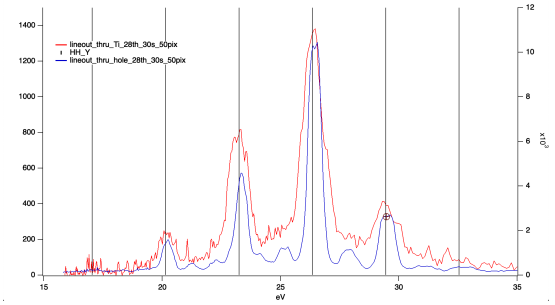

Figure 4.2: Spectrum of the HHG pump pulse after going through a cold Ti film (red) and through the whole in the film (blue).

Second, a set of acquired spectra (figure 4.2) adds that all the harmonics peaks that compose the pulse, even the most energetic, excite electrons to states below the Fermi energy. Comparing the spectrum of the pulse traveling unimpeded to the detector and the one that goes through the cold Ti film, one can conclude that the peaks maintain their relative heights. This means that either all the energies induce transitions to above or below the Fermi level; otherwise there would be a relative difference in the absorption of different harmonic peaks. Finally, taking into account the ionization energy of solid titanium - 32 eV -, we can conclude that we are probing the occupation of the DOS of the continuum electrons, and not inducing photoionization transitions.

To obtain the relative to cold XUV transmission time series from the knowledge of the electronic distribution function, it can be stated that:

$$A(f,\varepsilon_t) \propto \frac{\int(1-f(\varepsilon,t))\cdot HHG(\varepsilon,\varepsilon_t)d\varepsilon}{\int HHG(\varepsilon,\varepsilon_t)d\varepsilon} \Rightarrow T(f,\varepsilon_t) \propto 1 - \frac{\int(1-f(\varepsilon,t))\cdot HHG(\varepsilon_t)}{\int HHG(\varepsilon,\varepsilon_t)d\varepsilon}d\varepsilon \tag{4.1}$$

with A being the absorption coefficient, T being the transmission coefficient (both averaged in energy over all the XUV spectrum), and $HHG(\varepsilon,\varepsilon_t)$ being the XUV-excited electronic distribution, in the shape of the HHG spectrum. The ε_t model parameter defines the position of this spectrum in the energy scale of the continuum electrons. It is the distance, in energy, between the location of the highest harmonic peak and the Fermi energy. For the forward model simulation run henceforth, this ε_t parameter will be allowed to vary in the range $[-10,-4]$ eV, meaning that, on average, electrons are being excited to states below the Fermi energy and the harmonic excitation can indeed induce bound-free transitions in our sample. This acts as a prior since it is encoding our knowledge.

Figure 4.3 shows the integrand of equation 4.1, plotted against energy, with the zero energy level being the beginning of the continuum states. Plotted also is an inverse Fermi-Dirac distribution and an XUV-excited electronic spectrum, for a given ε_t. As $1-f$ comes from a TTM simulation where the DOS is assumed to be the free electron gas one and the effective electronic mass is allowed to vary, the Fermi energy is higher than the observed cold Ti Fermi energy. From figure 4.3a to 4.3b, energy has been deposited in the electronic distribution and, so, the Fermi-Dirac tilted. Since most of the harmonic spectrum was below the Fermi level, this tilting contributes to an opening of vacancies for transitions, observable in the increase in the area below the total integrand function. This will translate into increased absorption and decreased transmission.

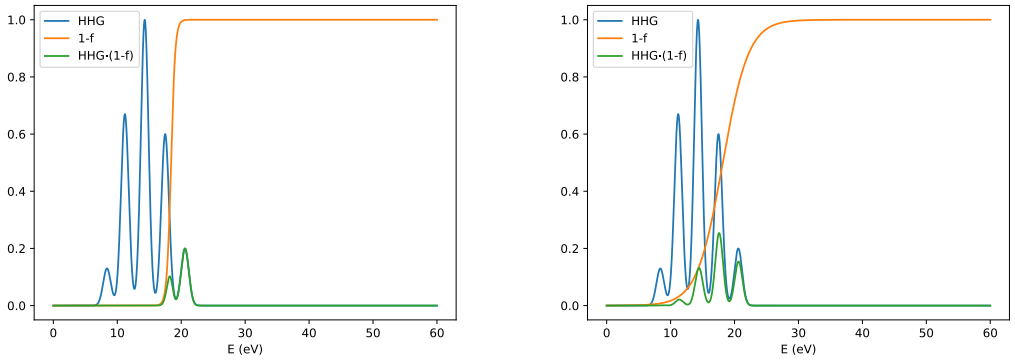

(a) Plot of $(1-f)$ calculated at the beginning of the simulation, for cold Ti.

(b) Plot of $(1-f)$ calculated 150 fs after the peak laser energy was deposited.

Figure 4.3: Integrand of equation 4.1, as a function of energy and its two components for $\varepsilon_t = 4$ eV. $(1-f)$ was calculated from a TTM simulation.

Finally, the relative to cold XUV transmission can be obtained, from these proportionality relationships, by a simple normalization procedure: $T_r(\varepsilon_t,t) = T(f,\varepsilon_t,t)/T(f,\varepsilon_t,0)$. The remaining challenge is then to forward model, from the initially known conditions (energy deposited by the pulse, time of deposition, and pump laser wavelength), the electron distribution as a function of time.

4.2 Two-Temperature Model

The TTM is a relatively simple way of modeling the e-e equilibration in a metal after irradiation by a femtosecond laser that relies on an ad hoc source term and assumption of instantaneous e-e equilibrium. It has been discussed in section 1.5.3 and 2.2.3.

The TTM will be applied as stated in its simplified form - equation 2.15 -, where heat conduction is neglected. It is important to note that lateral heat conduction can be disregarded because the spot size of the laser is much bigger that the absorption depth, making it such that energy deposited in a given zone of interest does not escape to another in a relevant timescale. From the diffusion coefficient, calculated with equation 1.21, it is possible to extract a heat diffusion time as $\tau_{\text{heat}} \sim d^2/D$, where d is the traversed distance. For Ti near the ablation threshold where the e-e collision frequency is at its broad and flat maximum (figure 1.4), the diffusion coefficient can be estimated as $D \sim 0.0001$ m/s^2. Considering a typical zone of interest distance of $d \sim 10$ μm, the heat diffusion time is $t_{heat} \sim 1$ μs, orders of magnitude above the scales we are interested in.

As for longitudinal heat conduction, the same calculations produce $t_{heat} \sim 0.1$ ns, for our 100 nm foil, which is still significantly larger than the tens fs to tens of ps time scales over which absorption and equilibration take place. Within the skin-depth of Ti - measured to be $\delta_s = 27$ nm in [56], for a wavelength and pulse duration similar to ours, significantly faster transport is expected, with $\tau_{heat} \sim 7$ ps, within the e-i equilibration time scale. Because this implies that smoothing out over the skin depth starts taking place quickly after absorption, a simplifying assumption can then be deployed regarding the absorbed power density term $Q_{abs}(x, r, t)$ (equation 1.19): a constant power density is assumed, over the skin-depth, with the same total power as the exponentially decaying distribution.

Since the ablated region was divided into three sub-zones, we assumed that the laser intensity does not vary spatially, within each one. That is, a single average fluence (corresponding to the same total absorbed energy per zone, as with the Gaussian distribution) is considered for each of the zones, as referenced in section 3.4. The source term expression is then written as:

$$S_{abs}(t) = \frac{I_a(t)}{\delta_s}, \text{ with } I_a(t) = \sqrt{\frac{4\ln(2)}{\pi}} \frac{F(1-R)}{\tau_p} \exp\left\{-4\ln(2)\left[\frac{(t-t_0)}{\tau_p}\right]^2\right\} \tag{4.2}$$

with I_a being absorbed intensity, F being the average incident fluence of a given zone of interest and $R = 0.558 \pm 0.001$ the measured reflectivity coefficient.

Finally, with all the terms in equation 2.15 properly defined, a computational algorithm can be deployed to solve it for the time evolution of the distribution function. Note that, since an equilibrium electronic distribution is assumed and the model only evolves temperature, the chemical potential μ has to be determined separately. This can be accomplished with equation 1.6, which ensures particle number conservation - consistent with the fact that no ionization of core electrons is expected. The condition can be re-written as:

$$n_e = \int f(\varepsilon, \mu, T_e) \cdot D(\varepsilon) d\varepsilon \tag{4.3}$$

with n_e the electronic density. The electronic heat capacity was calculated as in equation 2.16, while the ionic

heat capacity was set to $C_i \approx 3k_b/2$. The algorithm comprising the TTM forward model is presented below.

In algorithm 1, F and t_f are data series specific, while m_{eff}, ε_t, δ_s and G or λ are free parameters. The parameter m_{eff} is only necessary when working under a nearly free electron DOS assumption, such that:

$$D(\varepsilon, m_{eff}) = \frac{\sqrt{2 \cdot \varepsilon \cdot m_{eff}} \cdot m_{eff}}{\pi^2 \hbar^3}. \tag{4.4}$$

In some of the model runs, this was replaced by a room temperature Ti DOS calculated from DFT. In these cases, the DOS is fully defined without any free parameter and needs only to be interpolated in energy, to be used.

Algorithm 1 The algorithm for the TTM physical forward model. * means this variable is not always utilized and or represents two different ways of calculating the coupling parameter.

TTM(F, t_f, m_{eff}*, ε_t, δ_s, G or λ)

$t_1 \leftarrow [0, 5, 10, ..., 200]$ fs
$t_2 \leftarrow [225, 250, ...t_f]$ fs ▷ $t_f :=$ timestamp of the last acquisition in a given data family.
$T_i, T_e \leftarrow \{300, 300\}$ K
$\varepsilon \leftarrow [0.001, 0.011, 0.021, ..., 1000]$ eV
$e_{test} \leftarrow [0, 0.2, 0.4, ..., 25]$ eV ▷ $e_{test} :=$ range of energies to be tested for the Fermi Energy.
$L \leftarrow S_{abs}(t_1, F, \delta_s)$ ▷ $L :=$ laser profile vector, peaking at 100 fs. $F :=$ average fluence of the zone being tested.

$i \leftarrow 0$
while $\int f(\varepsilon, e_{test}[i], T_e) \cdot D(\varepsilon, m_{eff}) d\varepsilon \neq n_e$ **do** ▷ $f(\varepsilon, \mu, T_e)$ always corresponds to the Fermi-Dirac function.
    $i \leftarrow i + 1$
end while
$\mu \leftarrow e_{test}[i]$

for k in len(t_1) **do**
    $dt_1 \leftarrow t_1[2] - t_1[1]$
    $e_{test} \leftarrow [\mu - 3, \mu - 3 + 0.12, \mu - 3 + 0.24, ..., e_f + 3 - 0.12, e_f + 3]$
    $i \leftarrow 0$
    while $\int f(\varepsilon, e_{test}[i], T_e) \cdot D(\varepsilon, m_{eff}) d\varepsilon \neq n_e$ **do** ▷ Calculation if the chemical potential, at each time step.
        $i \leftarrow i + 1$
    end while
    $\mu \leftarrow e_{test}[i]$
    $C_e \leftarrow C(\varepsilon, m_{eff}, T_e, \mu)$ ▷ With the Fermi-Dirac of a given time step fully determined we can calculate C_e and G_{ei}, that depend on its derivatives, calculated analytically (equation 4.5).
    $G \leftarrow G$ or $G \leftarrow G(\varepsilon, m_{eff}, T_e, \mu, \lambda)$
    $f \leftarrow spline(f(\varepsilon, \mu, T_e))$
    $M[k'] \leftarrow T_r(\varepsilon_t, f)$ ▷ XUV transmission with improved k resolution.
    $T_e \leftarrow T_e + (L[k] + G \cdot (T_i - T_e)) \cdot dt_1/C_e$ ▷ Update of the temperatures, for next step.
    $T_i \leftarrow T_i + (L[k] + G \cdot (T_i - T_e)) \cdot dt_1/C_i$
end for

for k in len(t_2) **do**
    $k \leftarrow k + len(t_1)$
    Repeat the previous "for" cycle but without L.
end for
Return M

As for the G or λ dichotomy, present in algorithm 1, it arises from two different ways of calculating G parameters being deployed. One uses equation 2.17, with λ being allowed to vary since it is an experimental parameter, providing model flexibility, in an otherwise completely predetermined calculation. The other one considers a constant G, in time, that is a free parameter, differing for each sub-zone. Since different sub-zone attained different peak electronic temperatures, this method still allows us to extract the T_e dependence of G, without assuming an analytical expression.

The code itself was written in *Python3* with resource to the *NumPy* [62] and *SciPy* [55] packages. The integration required for the C_e and G calculations were performed within the *SciPy*'s Simpson method and the splines under the *InterpolatedUnivariateSpline SciPy* method.

Both the C_e and G calculations, when using the Lin et al (equation 2.17) formula, require derivatives of the Fermi-Dirac function, which varies abruptly, possibly creating problems with overflows. To prevent this, the derivatives were analytically calculated and restructured, taking the form:

$$\frac{\partial f}{\partial T_e} = \frac{\varepsilon-\mu}{k_B \cdot T_e^2} \cdot \frac{1}{\exp\left(\frac{\varepsilon-\mu}{k_B \cdot T_e}\right) + 1/\exp\left(\frac{\varepsilon-\mu}{k_B \cdot T_e}\right) + 2}, \quad \frac{\partial f}{\partial \varepsilon} = \frac{-1}{k_B \cdot T_e} \cdot \frac{1}{\exp\left(\frac{\varepsilon-\mu}{k_B \cdot T_e}\right) + 1/\exp\left(\frac{\varepsilon-\mu}{k_B \cdot T_e}\right) + 2}. \quad (4.5)$$

With the exponential factors only in the denominators, even for energies distant from the chemical potential, the exponential factor overflows go safely to zero.

As can be seen from algorithm 1, the temperature time evolution was solved within a finite differences framework, with the time step carefully studied to be the largest that still allows for proper convergence.

Now that the physical forward model is well defined we will show results for Bayesian Inference samplings of the posterior distribution relying on the collected data. These searches were performed with using the likelihood function, priors, and affine MCMC techniques described in section 2.4. Regarding the non-informative priors, all of the scale parameters (m_{eff}, δ_s, and λ or G) were normalized to their expected value, as they were found in the literature. The utilized values and references are present in table 4.1. The *Python3* package used for the affine invariant MCMC was *emcee* [53] and the optima used for the Monte Carlo initiation were extracted form an evolutionary algorithm implemented in the package *cma* [63]. All 40 walkers deployed in each MCMC run were initialized on a small ball around the optima.

Parameter	Theoretical Value	Reference
m_{eff}^0	9.101×10^{-31} kg	–
δ_s^0	27 nm	[56]
$\lambda^0 \langle \omega^2 \rangle$	350 meV^2	[41]
G_{ei}^0 (FEG)	3×10^{17} W·m^{3}K^{-1}	[41]

Table 4.1: Theoretical (and normalizing) values of the free scale parameters of the TTM.

4.2.1 MCMC searches with Lin's G_{ei}

In this section, MCMC searches of the posterior distribution using physical forward models based on the TTM will be presented, where the coupling coefficient was calculated according to Lin's equation 2.17. Two different

types of models were deployed, within this framework, one with a nearly free electron DOS and the other with a DFT-calculated cold Ti DOS. Only the former has an effective mass-free parameter and, so, the latter provides less parametric freedom.

For the nearly free DOS model, two different MCMC searches were run: one considering the three different zones of interest in the 150 μJ series (figure 3.16b, which is our cleanest and most complete series) and the other considering all the different data series and sub-zones except for the second 250 μJ family (figure 3.16d) and the 1000 μJ one (figure 3.16g). The former was excluded because it only pertains to the first 150 fs after the pumping (before significant e-e equilibration takes place), and the latter because of the unusual ring-like pattern, which makes the middle sub-zone the least bright, instead of the inner one. This is inconsistent with our theoretical considerations and might be due to a mirror defect created by the high fluence of the pump in the central region of the beam. In both cases, the free parameters discussed above will be shared by all data series, while the series-dependent ones (F and t_f) will vary according to the sub-zone being simulated.

Free electron DOS

Figure 4.4 displays results from two different MCMC searches of posteriors performed for the same forward model - a free electron DOS TTM model with Lin-like e-i coupling. One of them only sampled the joint posterior of the three sub-zones from the 150 μJ family, while the other sampled the posterior of all data but the above-mentioned families. Since 3 or 4-dimensional plots are not possible, the results of these searches are presented in the form of marginalized posterior distributions (the diagonal plots), and 2D correlations between parameters. The marginalized posteriors can be used to calculate the most likely value of each parameter and the associated 1σ error bars. To this end, the value of the $\{0.16, 0.5, 0.84\}$ quantiles of the marginalized distribution of each parameter are presented in table 4.2, corresponding to the region where 68% of the walker steps are concentrated, for a given free parameter, and its central estimate.

On a macro level, the results appear in broad agreement with each other, that is, between the two different searches considering the 150 μJ data set and the extended one. Focusing on the central estimate in table 4.2, the scale parameters are close to one another and have broadly compatible uncertainty ranges. These are also the parameters with the most physical significance, while the harmonic peak's distance to the Fermi energy (ε_t), the more problem-specific parameter, seems to be the most discrepant. The 1σ error bars are significantly increased for this parameter along with the ones for δ_s. Looking at the shape of the marginalized posteriors themselves, in figure 4.4, strong but uneven bi-modality is observed, cautioning that presenting the data as in table 4.2 might be somewhat misleading.

Parameter	150 μJ series	All series
λ/λ^0	$0.83^{+0.15}_{-0.19}$	$0.85^{+0.10}_{-0.42}$
ε_t (eV)	$-6.75^{+1.10}_{-0.63}$	$-8.57^{+3.91}_{-0.22}$
δ_s/δ_s^0	$0.52^{+1.38}_{-0.06}$	$0.46^{+3.14}_{-0.01}$
m_{eff}/m_{eff}^0	$1.89^{+0.12}_{-1.38}$	$1.57^{+0.04}_{-1.00}$

Table 4.2: Most likely value and 1σ errors of the MCMC searches performed for a physical forward model of a TTM, with Lin-like coupling parameter and DOS as in equation 4.4.

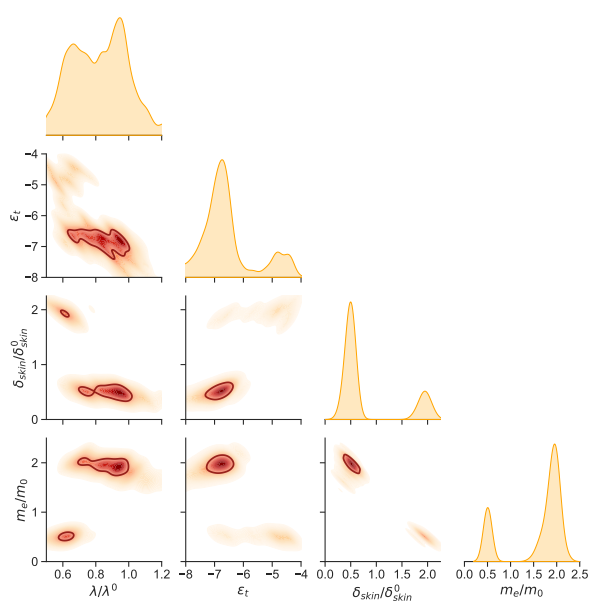

(a) Search with only the sub-zones of the 150 μJ series as data points. 25000 total model evaluations were performed with 15000 discarded as burn-in.

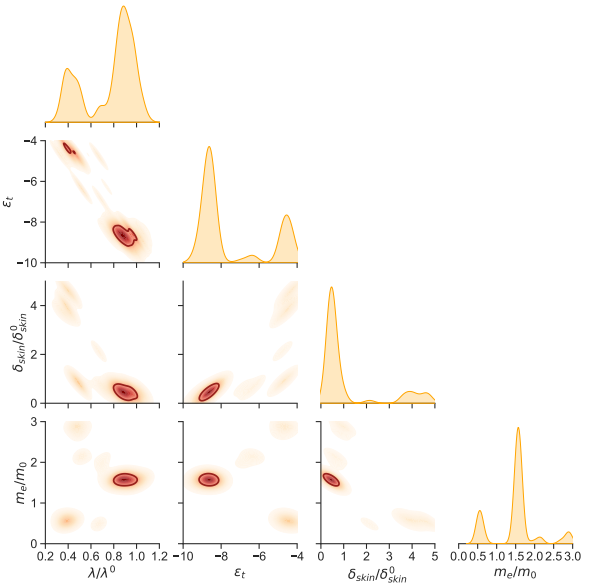

(b) Search with all sub-zones except the second 250 μJ and 1000 μJ series as data points. 20000 total model evaluations were performed with 10000 discarded as burn-in.

Figure 4.4: 2D correlations and marginalized posterior distribution of the free parameters of a physical forward model based on the TTM, with Lin-like coupling parameter (equation 2.17) and DOS as in equation 4.4. The estimations were performed with MCMC searches, over the free parameter space, with an ensemble of 40 walkers and a least squares likelihood function. The darker line on the 2D correlation is the 1σ band.

Considering, now, the 2D correlations between the parameters displayed in figure 4.4, we shall focus first on the ones involving the skin depth, as this is the parameter that directly controls the power density absorbed by a given sub-zone of interest (the average fluence and τ_p are fixed). The energy density deposited in the Ti film determines, in turn, the physical regime we are dealing with. In the δ_s correlations the bi-modality is clear but the relative position of the two local minima allows for further interpretation.

First, it is important to note that since the simplified TTM employed disregards the transverse absorbed energy gradient (section 4.2) a longer skin depth is associated with a lower energy density for a given sub-zone. This is due to the fact that the volume over which the same fluence is attenuated/absorbed is bigger. From here, the direct correlation between ε_t and δ_s becomes apparent: the further the HHG spectrum is from the Fermi energy, the higher T_e needs to reach, to achieve the same $\min(T_r(\varepsilon_t, t))$ - our observable. Since a higher T_e, all else being equal, requires more energy density - that is a smaller skin depth -, the direct correlation between the parameters, present in the two MCMC runs of figure 4.4, is then explained.

The inverse correlation between δ_s and m_{eff} can be explained similarly: heavier electrons take more energy to achieve a given T_e than lighter ones. As such, the higher the electronic mass, the higher the skin depth needs to be to achieve the same XUV transmission. It is also worth noting that this correlation weakens from figure 4.4a to figure 4.4b as one of the bi-modality modes is suppressed, probably due to higher amounts of data adding certainty about which of the two modes is the best.

Regarding δ_s vs λ, an inverse correlation between the parameters is found in both searches, again weakened in the one over the extended data set, probably due to similar reasons. In this case, more deposited energy,

in the form of a lower δ_s, leads to a higher e-i coupling. Having reached higher energy, to recover to the same final XUV transmission, in an amount of time determined by the experimental data, electrons need to exchange energy with the ions at a faster rate, explaining the correlation.

Finally, the inverse correlation between λ and ε_t appears as strong and persistent between the two figures. It can be interpreted in a similar fashion to the other ones: an HHG spectrum further away still requires higher T_e to achieve the same transmission. It also requires more rapid thermalizing when recovering to the same higher level of XUV tansmission.

To evaluate the efficacy of the MCMC searches, the results of the forward model runs are typically projected into the space of the observed data. To do that, 100 samples were chosen, independently, from the MCMC-generated ensemble with the burn-in period discarded. The plots for both searches are presented in figures 4.5 and 4.6.

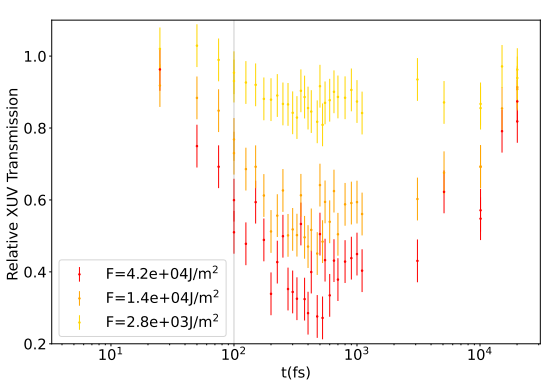

(a) For the search with only the sub-zones of the 150 μJ series as data points.

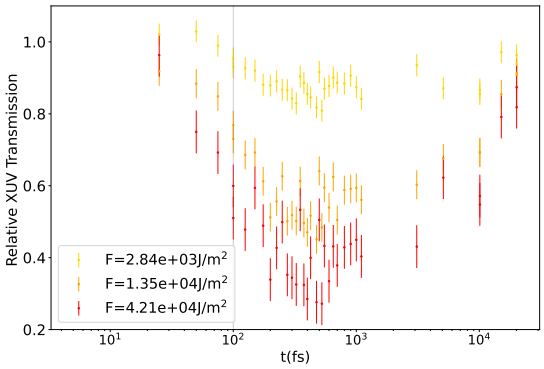

(b) For the search with all sub-zones except the second 250 μJ and 1000 μ J series as data points. Only 150 μJ were plotted for direct comparison.

Figure 4.5: 100 model runs with parameters sampled independently from the ensembles generated by the MCMC searches, for a physical forward model of a TTM, with Lin-like coupling parameter (equation 2.17) and DOS as in equation 4.4, plotted on top of the experimental data. In log scale with the laser fluence peaking at 100 fs.

Observing figure 4.5a, it can be concluded that the model had enough parametric freedom to match, in all 3 sub-zones, the low plateau of the $T_r(\varepsilon_t, t)$ data. The interplay between achieved maximal T_e (controlled by the power density, mainly related to δ_s and heat capacity, mainly related to m_{eff}) and ε_t is enough to achieve proper agreement, in these timescales, with the several data series. The ps recovery to values close to the cold ones, however, is more discrepant, for the higher fluency region, in red. Since the recovery is slower than the data suggest it should be, we conclude that the e-i coupling coefficient is underestimated for higher fluences. At the same time, for the lowest fluence region, an overestimation is apparent, which rules out longitudinal thermal conduction as the cause of the previous underestimation. These mismatches suggest that the formula being used to calculate G_{ei} (equation 2.17) does not apply to all the regimes of excitation, at least in the nearly free electron gas approximation. Since the MCMC search was performed for all three sub-zones simultaneously, a compromise is then struck between how well the parameters adjust to each series.

Figure 4.5b was plotted from the MCMC results of the combined search over all data series, but only displays the three 150 μJ sub-zones results, to allow for direct comparison between the searches. The overall

features are very similar, with some slight differences: less dispersion of the model results and less agreement, in the series of intermediate fluence, at the point of minimal $T_r(\varepsilon_t, t)$. The former is reflected in the weaker bi-modality of the marginalized posteriors in figure 4.4, itself a consequence of more experimental data allowing for a better decision to be made between different regimes; the latter is related to the compromise already discussed having to be struck between more data series than before.

Figure 4.6 was plotted along similar lines, for the complete MCMC search. This time, more data series are plotted so a fuller picture can be grasped. Specifically, we plot one data series for each of the five fluence ranges presented. It is clear that the model results and the data sets agree less than when a narrower search was performed. As was discussed for figure 4.5b, here the plateau of minimal simulated $T_r(\varepsilon_t, t)$ agrees with the experimental data as often as not. Furthermore, the relaxation time of the electronic temperature is somewhat underestimated for the series with the least fluence and overestimated for the highest absorbed fluence ones, leading to similar conclusions about the unsuitability of Lin's formula (equation 2.17) for the different regimes at play, within a nearly free electron DOS assumption.

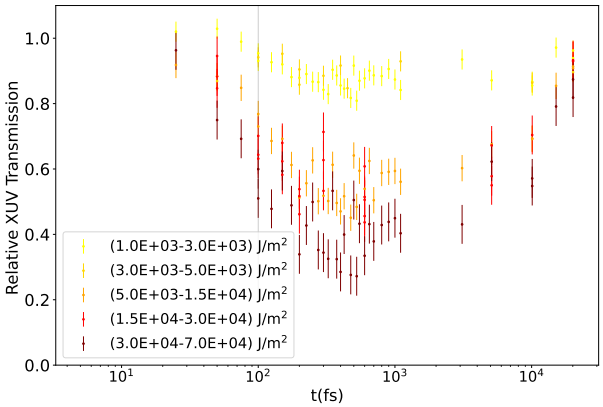

Figure 4.6: 100 model runs with parameters sampled independently from the ensemble generated by the MCMC search, considering all sub-zones, for a forward model comprised of a TTM with Lin-like coupling parameter and DOS as in equation 4.4, plotted on top of the experimental data. In log scale with the laser fluence peaking at 100 fs.

From the MCMC searches here presented, it is also possible to extract estimates of other variables of interest, not only the model parameters themselves. To do so, one calculates the desired observable in each of the 100 model runs used to construct figure 4.5 and 4.6 and takes the mean and standard deviation of the generated ensemble, to get a central estimate and 1σ error bars. This process is illustrated only once, further down in 4.17.

The first such variable of interest is the G_{ei} and how its time-averaged value depends on electronic temperature. To grasp what the input parameters estimated by the MCMC can tell us concerning this, figure 4.7 was constructed. It plots the central estimate and 1σ error bars of the temporal average of the G_{ei} parameters against the maximum achieved T_e in the given data series. It does so for each of the considered sub-zones, resulting in a single data point for each of them. Both figure 4.7a and 4.7b depict the same overall trend of a gently declining slope with increased T_e. Comparing the results with different calculations from literature, presented in section 2.2.3, the agreement between the calculated G_{ei} and the XTANT-3 estimated one is quite

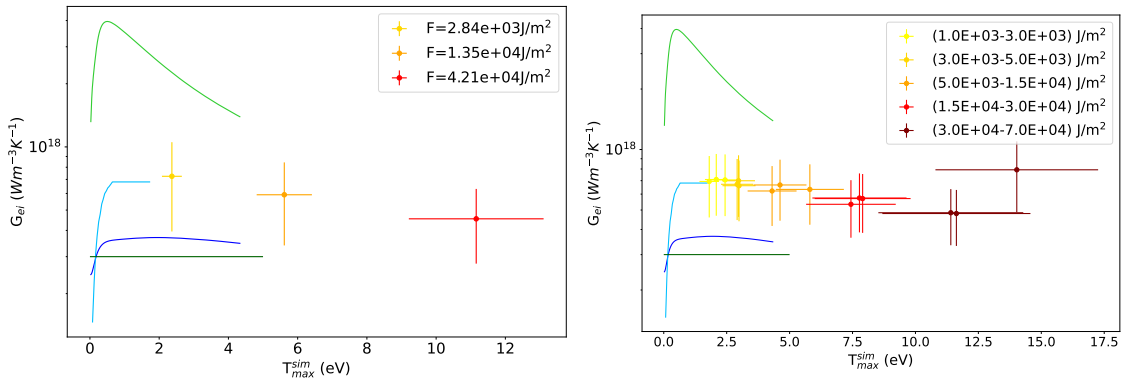

(a) For the search with only the sub-zones of the 150 μJ series as data points.

(b) For the search with all sub-zones except the second 250 μJ and 1000 μ J series as data points.

Figure 4.7: Temporally averaged G_{ei} vs maximum T_e, for each sub-zone considered. Central estimate and error bars obtain by sampling 100 model runs, from MCMC search results for a forward model comprised of a TTM with Lin-like coupling parameter and DOS as in equation 4.4. The light green line is Lin's result ([41]) for a cold Ti DOS and the dark blue line refers to calculations with the same formula but an Al (or FEG-like) DOS. In dark green the result of Rethfeld ([23]) for a FEG and in light blue the XTANT-3 code predictions for Ti [10].

good, although the calculations were only performed up to 2 eV.

Lin's aluminum results and Rethefeld's FEG present a similar behavior but consistently underestimate the absolute value of the parameter. This probably reflects the posterior of m_{eff}, which for both searches vanishes at around $m_{eff} \approx 1$. The most discrepant theoretical prediction is Lin's Ti one. In this case, since a different DOS is introduced in equation 2.17, the shape of the curve was expected to differ from the data. Even with the additional degree of freedom (m_{eff}), it is striking that the absolute values of the data points and the curve are incompatible, with a consistent and significant overestimation of the theoretical values compared to the MCMC extracted data.

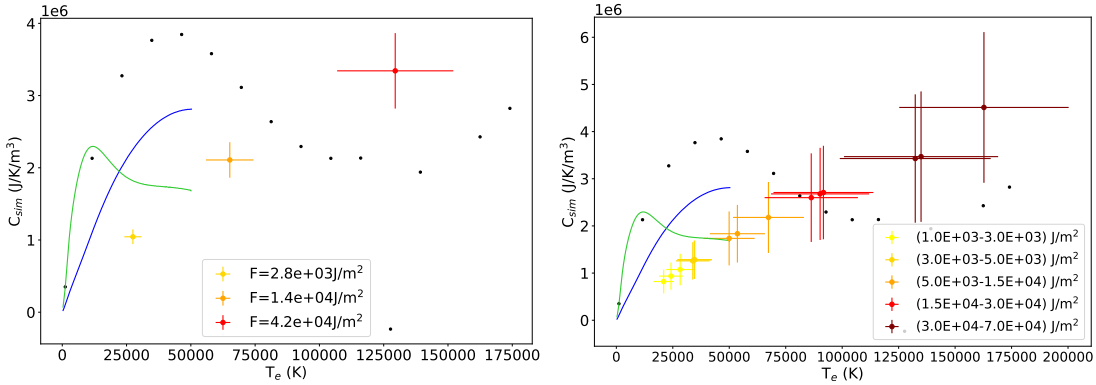

(a) For the search with only the sub-zones of the 150 μJ series as data points.

(b) For the search with all sub-zones except the second 250 μJ and 1000 μ J series as data points.

Figure 4.8: C_e simulated vs maximum T_e, for each sub-zone considered. Central estimate and error bars were obtained by sampling 100 model runs, from MCMC search results for a forward model comprised of a TTM with Lin-like coupling parameter and DOS as in equation 4.4. The light green line is Lin's result ([41]) for a cold Ti DOS and the dark blue line refers to calculations with the same formula but an Al (or FEG-like) DOS. The black dots are the heat capacity estimates from a finite temperature DFT simulation with a cold lattice.

Figure 4.8 shows the heat capacity, estimated with the method described above, of each of the sub-zones considered in a given MCMCM search. In this case, the observable C_e was not calculated from equation 2.16 but was approximated along simpler lines:

$$C_e(T_e^{max}) \sim \frac{F}{T_e^{max} \cdot \ell_f} \tag{4.6}$$

with $\ell_f = 100$ nm the thickness of the film, and F the observed fluence of a given sub-zone. This was done to compare these C_e results with those from section 4.3. Both figures 4.8a and 4.8b exhibit a linear growth trend, with similar slopes, more compatible in shape with the Al Lin's calculation, than with the Ti ones. The absolute values of the heat capacities are within the range of magnitude of both theoretical calculations. A significant mismatch in the shape of the curve is also present when comparing the data points with the black ones, obtained from a finite temperature DFT simulation, performed in the VASP package [57–61], that assumes a cold ionic structure and excited electrons - along the lines drawn in section 2.2.2. Broad agreement in the orders of magnitude can be observed, with the relative error being close or smaller than 1σ for T_e above 7500K, especially in figure 4.8b.

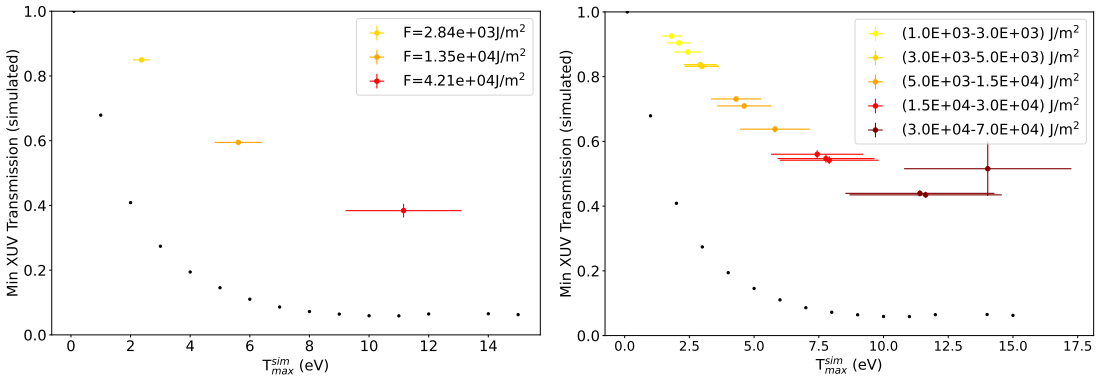

(a) For the search with only the sub-zones of the 150 μJ series as data points.

(b) For the search with all sub-zones except the second 250 μJ and 1000 μ J series as data points.

Figure 4.9: Minimum XUV transmission vs maximum T_e, for each sub-zone considered. Central estimate and error bars were obtained by sampling 100 model runs, from MCMC search results for a forward model comprised of a TTM with Lin-like coupling parameter and DOS as in equation 4.4. The black dots are the optical response properties estimates from a finite temperature DFT simulation with a cold lattice.

Finally, figure 4.9 displays the minimal XUV opacity versus the maximum T_e, plotted with the process described earlier in this section. The black dots are theoretical predictions from the same finite temperature DFT code described above. The overall trend in the data is similar to the predictions, although the magnitude of it is significantly different. This might be due to the fact that DFT does not provide good estimates of the core state energy. In the DFT simulations presented, the $3p$ state energy was -24.5 eV, for a cold lattice. Using the central photon energy in figure 3.2, this would imply a parameter $\varepsilon_t \sim -5.5$ eV. Our physical forward model allows for variation of such parameters, allowing us to obtain its posterior distribution, exactly to account for this DFT uncertainty. Our more data-driven estimation of this parameter yields significantly different results, as can be seen in table 4.2. Since the XUV transmission is highly sensitive to ε_t, this might,

in large part, explain the observed difference.

Ti DOS

In this section, we discuss the results of an MCMC search of the posterior distribution, for a forward model consisting of a TTM with fixed, cold Ti DOS, calculated from DFT. The coupling coefficient G_{ei} and the electronic heat capacity C_e were calculated from equations 2.17 and 2.16, respectively. Figure 4.10 displays the marginalized posteriors of each of the model parameters alongside the 2-dimensional correlations. The corresponding central estimate and error bars are: $\lambda/\lambda^0 = 0.93^{+0.17}_{-0.10}$, $\varepsilon_t = -4.51^{+0.10}_{-0.12}$ and $\delta_s/\delta_S^0 = 0.31^{+0.01}_{-0.02}$.

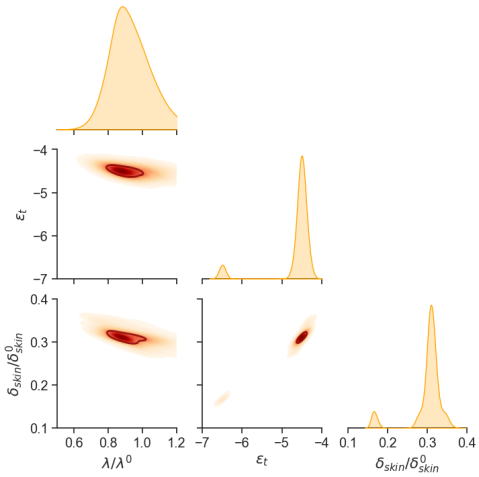

Figure 4.10: 2D correlations and marginalized posterior distribution of the free parameters of a physical forward model based on the TTM, with Lin-like coupling parameter (equation 2.17) and Ti DFT-calculated DOS. The estimations were performed with MCMC searches, over the free parameter space, with an ensemble of 40 walkers and a least squares likelihood function. The darker line on the 2D correlation is the 1σ band. 40000 total model evaluations were performed and the first 20000 were discarded.

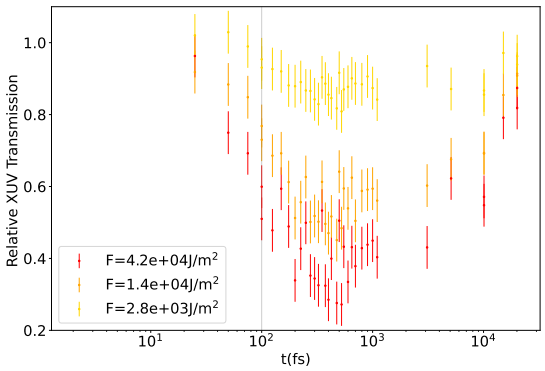

Figure 4.11: 50 model runs with parameters sampled independently from the ensemble generated by the MCMC search, for a physical forward model of a TTM, with Lin-like coupling parameter and TI DFT-calculated DOS, plotted on top of the experimental data. In log scale with the laser fluence peaking at 100 fs.

Looking at the marginalized posteriors, the main difference to note, compared to 4.4, is the very narrow peak in the skin depth - δ_s. The little bi-modality that remains still allows us to make out an inverse correlation between this parameter and ε_t. The physical reasoning for this was already given above and should be expected to remain a strong feature of the searches, as the two parameters are so closely linked. The other correlation observed in figure 4.4 that could also be present in the current corner plot is the δ_s to λ inverse correlation, very muted in this search. This might be due to the relative stiffness of the model and lack of ability to properly simulate the recovery period of the transmission, as we shall see next.

Focusing on figure 4.11, this inability to model the recovery immediately becomes apparent. While the zone of intermediate fluence is properly simulated, the model overestimated the recovery rate of the lower fluence zones and, concurrently, underestimates the recovery rate of the zone of higher fluence to a high degree. This attempted compromise, between different sub-zones, results from the inability of equation 2.17

(when coupled to a DFT calculated DOS) to provide either adequate results in our fluency range or enough parametric freedom to adjust to this "theoretical knowledge gap".

In figure 4.12, the estimates for the coupling coefficient produced from the MCMC search are plotted against the theoretical predictions already discussed. These show great compatibility with Lin's Ti calculations, which is unsurprising since the same formula was used, with an estimated $\lambda \sim 1$ and an otherwise rigid model.

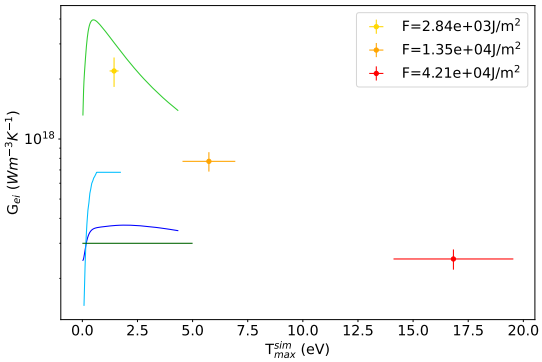

Figure 4.12: Temporally averaged G_{ei} vs maximum T_e, for each sub-zone considered. Central estimate and error bars obtain by sampling 100 model runs, from MCMC search results for a forward model comprised of a TTM with Lin-like coupling parameter and DFT calculated Ti DOS. The light green line is Lin's result ([41]) for a cold Ti DOS and the dark blue line refers to calculations with the same formula but an Al (or FEG-like) DOS. In dark green the result of Rethfeld ([23]) for a FEG and in light blue the XTANT-3 code predictions for Ti [10].

Results from figure 4.13 are somewhat more noticeable since they do not seem to follow Lin's Ti prediction, although their order of magnitude is the same. This might be due to the approximated way the heat capacity was obtained (equation 4.6). The substitution of the temperature derivative by a simple division gives an overall approximation of the heat capacity but might miss some more subtle behavior (since it gives a more cumulative estimate). Again, in this case, the shape of the heat capacity curve more closely resembles that of a FEG (or Al).

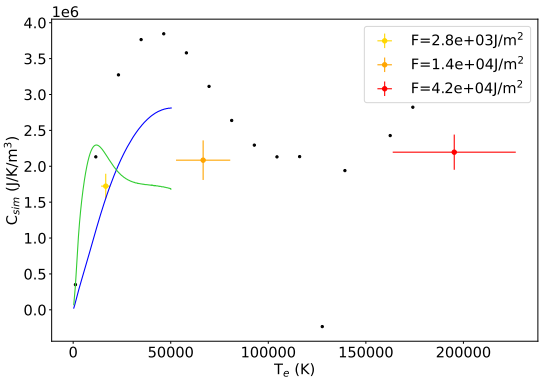

Figure 4.13: C_e vs maximum T_e, for each sub-zone considered. Central estimate and error bars obtain by sampling 100 model runs, from MCMC search results for a forward model comprised of a TTM with Lin-like coupling parameter and DFT calculated Ti DOS. The light green line is Lin's result ([41]) for a cold Ti DOS and the dark blue line refers to calculations with the same formula but an Al (or FEG-like) DOS. Heat capacity estimates from a finite temperature DFT simulation with a cold lattice (black dots).

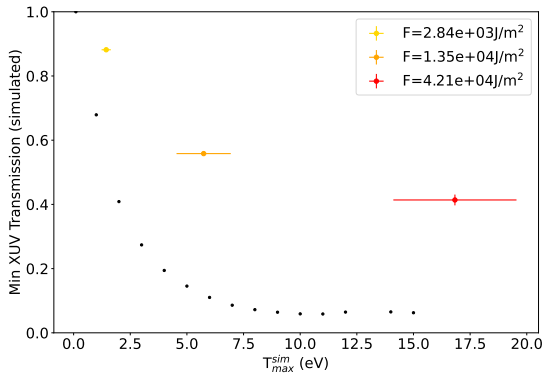

Figure 4.14: Minimum XUV transmission vs maximum T_e, for each sub-zone considered. Central estimate and error bars obtain by sampling 100 model runs, from MCMC search results for a forward model comprised of a TTM with Lin-like coupling parameter and DFT calculated Ti DOS. The black dots are the optical response properties estimates from a finite temperature DFT simulation with a cold lattice.

Finally, figure 4.14 is very similar to figure 4.9, with the same shape of the curve as the DFT results but severely underestimating the magnitude of the drop. The reasoning that justified this observed behavior previously remains sound.

4.2.2 MCMC searches for constant G_{ei}

In this section, a different approach is described, regarding how the MCMC searches are performed. In order to provide more parametric freedom an independent MCMC search was run for each of the sub-zones. As a result, a different set of marginalized posteriors and 2-dimensional correlations was obtained for each of the sub-zones studied, namely all the 150 μJ (figure 3.16b) series and the two innermost zones of the third family of series with 250 μJ (figure 3.16e), each represented by a different color in 4.15 and 4.16.

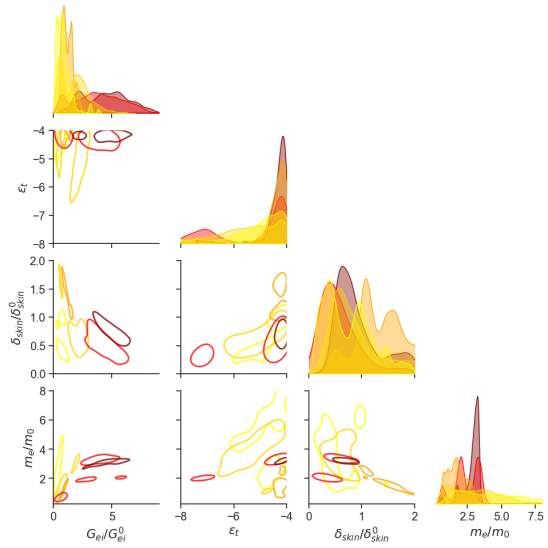

Figure 4.15: 2D correlations and marginalized posterior distribution of the free parameters of a physical forward model based on the TTM, with constant G_{ei} and DOS as in equation 4.4. The estimations were performed with MCMC searches, over the free parameter space, with an ensemble of 40 walkers and a least squares likelihood function. The darker line on the 2D correlation is the 1σ band.

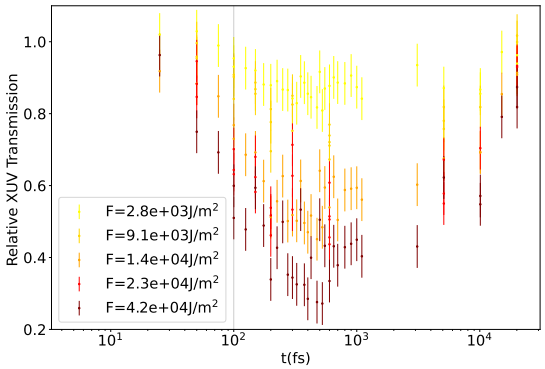

Figure 4.16: 50 model runs with parameters sampled independently from the ensembles generated by the MCMC searches, for a physical forward model of a TTM, with constant G_{ei} and DOS as in equation 4.4, plotted on top of the experimental data. In log scale with the laser fluence peaking at 100 fs.

For these MCMC searches, the G_{ei} coefficient was considered constant, during a given time series, with its value being one of the free parameters. Nonetheless, a nearly free electron DOS approximation was deployed to calculate C_e. The marginalized posteriors distributions of figure 4.15 are plotted alone, for better reading, in appendix A. In table 4.3, the central estimations and 1σ error bars are shown, for all sub-zones and inputs of the physical forward model. Combining these two pieces of information, agreement between the searches can be found for the parameters δ_s and ε_t. Looking at the 1σ intervals, they appear broadly compatible with one another and the posterior distribution of these two parameters have overlaying highest probability regions. Physically, this was expected to be the case, since neither skin-depth nor core-to-continuum energy differences are expected to be dependent on laser intensity, at first order. Their constancy through the different MCMC searches is then a sanity check for the convergence of the algorithm and an indication of the robustness of the estimation of such parameters. The remaining correlations, with some exceptions, are proxies of the physical relations of the δ_s ones, with very similar physical reasonings behind them.

Zone	G_{ei}/G_{ei}^0	ε_t (eV)	δ_s/δ_s^0	m_{eff}/m_{eff}^0
150 μJ, outer	$0.74^{+0.56}_{-0.41}$	$-4.85^{+0.68}_{-2.04}$	$0.67^{+0.53}_{-0.38}$	$4.16^{+3.22}_{-2.32}$
150 μJ, middle	$1.17^{+0.55}_{-0.39}$	$-4.28^{+0.2}_{-0.43}$	$1.38^{+0.47}_{-0.42}$	$1.66^{+0.82}_{-0.66}$
150 μJ, inner	$4.53^{+2.15}_{-2.29}$	$-4.23^{+0.16}_{-0.36}$	$0.80^{+0.76}_{-0.26}$	$3.04^{+0.25}_{-0.67}$
250 μJ, middle	$1.69^{+1.02}_{-1.08}$	$-5.47^{+1.14}_{-2.11}$	$0.83^{+1.14}_{-0.34}$	$2.62^{+2.19}_{-1.40}$
250 μJ, inner	$3.86^{+2.45}_{-2.25}$	$-4.78^{+0.65}_{-2.71}$	$0.52^{+0.95}_{-0.28}$	$2.26^{+1.98}_{-0.60}$

Table 4.3: Most likely value and 1σ errors of the 5 MCMC searches performed, one for each sub-zone, for a physical forward model of a TTM, with a constant coupling parameter and nearly free electron DOS.

Considering the G_{ei} and m_{eff} posteriors and estimates, they appear to change more from zone to zone (or incident fluence). This behavior is expected of G_{ei} since it depends on T_e (as covered in section 2.2.3)), intimately linked with the absorbed fluence of a given sub-zone. The m_{eff} dependency on electronic temperature is subtler in nature and comes from the fact that different deposited energies excite continuum electrons into different parts of the Ti DOS. Looking at figure 2.3, or more schematically at figure 4.1, it is clear that lower excitation energies that do not dislocate the electrons from the d-band have a higher effective mass than the hotter ones that are excited into the $4s$ band. These theoretical considerations are only partially confirmed by the results from the MCMC searches, with the notable outlier being the 150 μJ inner zone, with higher than expected m_{eff}. This deviation from expectations might be the result of the increased parametric freedom of the forward model, as important correlations between the input parameters were expected (such as m_{eff}, a proxy for C_e, vs δ_s, controlling the absorbed power density).

Looking at the 2-dimensional correlations of figure 4.15, the analysis remains similar to that of the first searches presented. A positive correlation exists between ε_t and δ_s/δ_s^0 while negative correlations prevail between δ_s/δ_s^0 and both G_{ei}/G_{ei}^0 and m_{eff}/m_{eff}^0. The physical reasoning between these correlations is expected to be the same as explained above. With added parametric freedom, or, conversely, with each MCMC search running with fewer data points against which to benchmark a given model, the high likelihood regions area naturally increases. This allows for a wider average step of the ensemble walkers and results in a broader 1σ band that, unlike in the previous runs, allows us to envisage the non-linear nature of the correlations in

question.

Figure 4.16 displays 100 forward model runs (for each sub-zone), selected independently from the MCMC-generated ensemble of walker chains, with the burn-in period extracted, plotted over the data of each sub-zone considered. The second and third-highest fluency zones display overlapping model predictions but also somewhat superimposed data points. A good match was achieved between the experimental data and the forward model 1σ band. Most data points, when considered with their uncertainty, fall within the band of results for their respective sub-zone. This is to be expected since significantly more flexibility was allowed in this physical forward model than for the ones used to produce figures 4.4 and 4.5, which already yielded reasonable agreement between model and data.

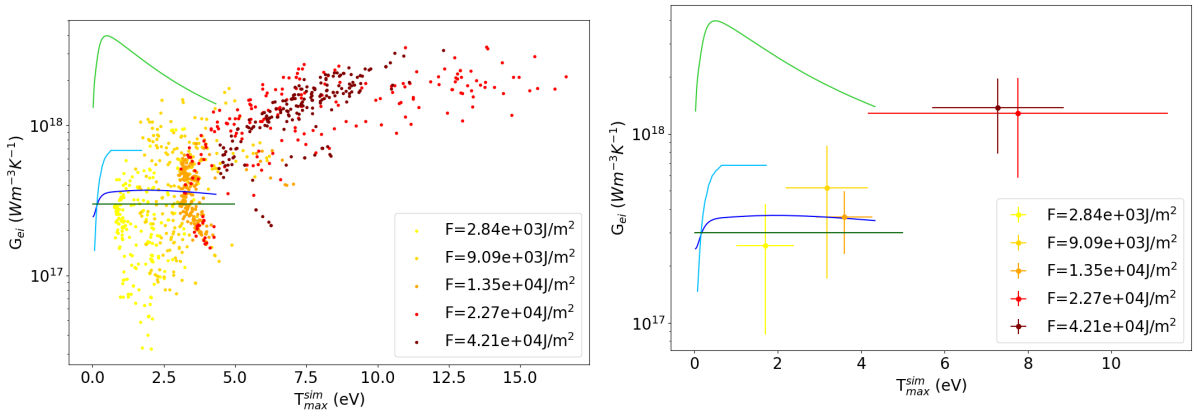

(a) Each point is the result of a model run, from the 100 sampled.

(b) A single data point is produced for each of the sub-zones. Central estimate obtained by averaging and error bars by standard deviation calculation.

Figure 4.17: G_{ei} vs maximum T_e, for each sub-zone considered. Sample comprised of 100 model runs, from MCMC search results for a forward model comprised of a TTM with constant G_{ei} and DOS as in equation 4.4. The light green line is Lin's result ([41]) for a cold Ti DOS and the dark blue line refers to calculations with the same formula but an Al (or FEG-like) DOS. In dark green the result of Rethfeld ([23]) for a FEG and in light blue the XTANT-3 code predictions for Ti [10].

In figure 4.17, no temporal averaging procedure was needed to obtain a single representative numerical value of G_{ei}, for each model run of the different sub-zones, since it was considered a constant. Taken together, however, the results of all the sub-zones, plotted vs the maximum T_e for that sub-zone, allow us to estimate G_{ei}'s temperature dependency. The results seem in agreement with FEG predictions for the three lowest fluency zones and shows a marked increase in coupling for the highest fluency zones. The overall tendency then is that of a sustained increase in G_{ei} with T_e, not predicted by any of the theoretical models considered.

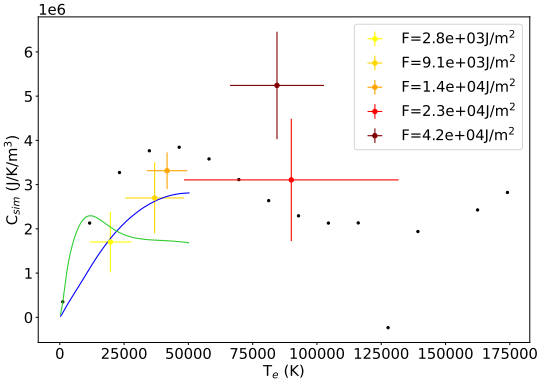

Figure 4.18: C_e vs maximum T_e, for each sub-zone considered. Central estimate and error bars obtain by sampling 100 model runs, from MCMC search results for a forward model comprised of a TTM with constant G_{ei} and DOS as in equation 4.4. The light green line is Lin's result ([41]) for a cold Ti DOS and the dark blue line refers to calculations with the same formula but an Al (or FEG-like) DOS. The black dots are the heat capacity estimates from a finite temperature DFT simulation with a cold lattice.

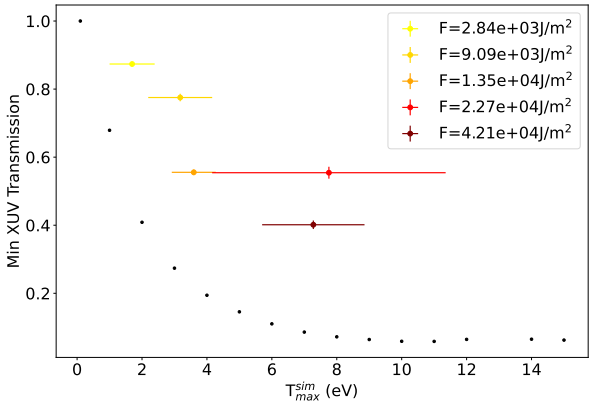

Figure 4.19: Minimum XUV transmission vs maximum T_e, for each sub-zone considered. Central estimate and error bars obtain by sampling 100 model runs, from MCMC search results for a forward model comprised of a TTM with constant G_{ei} and DOS as in equation 4.4. The black dots are the optical response properties estimates from a finite temperature DFT simulation with a cold lattice.

The heat capacity central estimates (calculated from 4.6) and 1σ error bars, are present in figure 4.18. Since each sub-zone had its own effective mass, this parameter, as others presented in this section, offers much more parametric freedom than before. From the Bayesian Inference discussion in section 2.4, one could say that the estimates rely on less prior information than before (encoded in the forward model itself), and, as such, are more closely dependent on the experimental data itself. The heat capacity parameter, despite this high parametric freedom, closely resembles Lin's Al prediction and the time-dependent DFT Ti results, with a notable outlier being the highest fluence sub-zone. Interestingly, this zone also exhibits a difference from the trend in terms of its effective mass. In both cases, the anomaly is positive, which is expected since heavier electrons should take, in general, more energy to reach a given T_e.

Finally, figure 4.19 displays the time-dependent DFT predictions for the XUV transmission, as a function of T_e vs the results of the MCMC search, for each zone. The analysis of this plot stays consistent for the three different TTMs used.

4.2.3 Summary and Conclusions

- Several different MCMC searches were performed for TTM models. The e-i coupling was calculated either from Lin's equation or considered constant in time. The DOS structure was also made to vary from a nearly free one (with varying effective mass) to the Ti DFT calculated one.

- Overall, the models based on a nearly free DOS (both with $G_{ei}(t)$ calculated from Lin's and when $G_{ei}(t) = \text{const}$) produce significantly better agreement with the experimental data. A caveat to this conclusion is that the Ti DOS is pre-determined, removing a degree of freedom from the model.

- When considering searches of just three sub-zones vs searches with all sub-zones of interest (18 in total, since two families of shots were removed), the posteriors of the latter are more strongly peaked. This is an expected effect of increasing the number of experimental data points. This is not particularly visible in the 1σ error bar since remnants of posterior bi-modality sometimes persist.

- The searches for G_{ei}=constant in time offer more parametric freedom, since each sub-zone takes its own free parameters, and produce the best agreement with the data.

- Figure 4.17 thus offers the most data-driven and less constrained estimation of $G_{ie}(T_e)$. Interestingly, while it is in the range of theoretical predictions, it draws its own distinct shape through T_e, although with significant error bars.

4.3 Quantum Boltzmann Statistics

In section 2.2.2, a Boltzmann equation model (Rethfeld) that simulates the absorption process of an ultrafast laser pulse by a thin metal film was described. In this section, we deployed it, as a physical forward model. This model was meant to study the first hundreds of fs after the arrival of the pump laser. Since the lattice and/or ionic response was left out of our considerations, e-i equilibration will not be part of the simulated phenomena.

In stark contrast to the TTM, the quantum Boltzmann equation does not assume instantaneously thermodynamical equilibrium within the electronic population, nor does it assume ad hoc absorption of the non-reflected part of the pump pulse power density. It instead incorporates e-e and electron-ion-photon (e-i-pt) collision terms that model these effects from first principles.

The differential equation 2.9, without the electron-phonon term, and the other two collisions terms described by equations 2.11 and 2.13, was used. The assumptions that lead to a simplified Boltzmann equation were discussed in section 2.2.2. To these, some of the TTM assumptions were added, since the same physical arguments still hold and are given more force by the fact that only hundreds of fs of time evolution will be modeled. As such, the absence of lateral heat conduction and a constant absorbed laser intensity were assumed, for each of the sub-zones of interest. The latter assumption implies that the laser intensity inside the material (necessary in the Bessel function argument of equation 2.13) takes the form of equation 4.2, that is only time and incident fluence dependent, for each of the sub-zones considered.

Since Rethfeld's model is fully deterministic, some parameters were freed, besides ε_t, which is intrinsic to the way the observable (XUV transmission) is calculated from $f_e(\boldsymbol{k})$. The free electron mass was replaced by an effective one m_{eff}, in a nearly free electron DOS approach - to include the differences between the Ti and a FEG DOS -; and the e-e and e-i screening coefficients, k, were allowed to vary by multiplying equation 2.12 by a dimensionless free constant, resulting in two different inverse screening radii κ_{ie} and κ_{ee}.

4.3.1 Analytical simplification of the collision terms

We now wish to solve the Boltzmann equation in time and obtain the evolution of the electronic non-equilibrium distribution function, as it is being excited by the laser. This solution will be the forward model used to calculate the likelihood function. To do so, it is necessary to transform the double and single sum of the detailed collision terms (equation 2.11 and 2.13, respectively) into integrals. To simplify the computational task to tractable levels, symmetry arguments will be used to solve some of them while others will be solved analytically and still others will be left for numerical methods.

The derivations that follow were based on [40]. The usual substitution for the sum of discrete momentum points $\sum_k \rightarrow \Omega/(2\pi)^3$ was performed on equation 2.11 and the variables of integration were changed from

k_1 and k_2 to k_1 and k_3 (the out-scattered momentum vectors) such that it was possible to obtain:

$$\left.\frac{\partial f(k)}{\partial t}\right|_{\text{el-el}} = \frac{2\pi}{\hbar}\frac{\Omega^2}{(2\pi)^6}\int_0^\infty k_1^2 dk_1 \int_0^\infty k_3^2 dk_3 \cdot (2\pi)^2 \int_{-1}^1 d\mu_1 \int_{-1}^1 d\mu_3 \left(\frac{e^2}{\varepsilon_0\Omega}\frac{1}{\Delta k^2+\kappa^2}\right)^2 \\ \left[f_{\boldsymbol{k}_3} f_{\boldsymbol{k}_1}(1-f_{\boldsymbol{k}})\left(1-f_{\boldsymbol{k}_2}\right) - f_{\boldsymbol{k}} f_{\boldsymbol{k}_2}\left(1-f_{\boldsymbol{k}_3}\right)\left(1-f_{\boldsymbol{k}_1}\right)\right]\delta\left(\frac{\hbar^2}{2m_e}\left(k_3^2+k_1^2-k_2^2-k^2\right)\right) \tag{4.7}$$

with $\boldsymbol{k}_2 = \boldsymbol{k}_1 - \boldsymbol{k} + \boldsymbol{k}_3$, $\Delta k = |\Delta\boldsymbol{k}| = |\boldsymbol{k}_1 - \boldsymbol{k}_2| = |\boldsymbol{k} - \boldsymbol{k}_3|$, $\mu_3 = \cos\angle(\boldsymbol{k}, \boldsymbol{k}_3)$, $\mu_1 = \cos\angle(\boldsymbol{\Delta k}, \boldsymbol{k}_1)$ and $\Omega = 1.058\times10^{-28}$ m^3 the volume of the Ti unit cell. For ease of reading $f(\boldsymbol{k_i}) \to f_{\boldsymbol{k}_i}$. Note how the azimuthal angles were summed over and the choice of μ_3 and μ_1 corresponds to choosing a z-axis, for the polar angle of $\boldsymbol{k_3}$ (θ_3), oriented as $\boldsymbol{k}$ and a z-axis oriented as $\boldsymbol{\Delta k}$ for θ_1.

These definitions of the polar angle allow us to write $\Delta k^2 = (\boldsymbol{k} - \boldsymbol{k_3})^2 = k^2 + k_3^2 + 2kk_3\mu_3$ from where $d\mu_3 = \Delta k/(kk_3)d\Delta k$ and analogously $d\mu_1 = k_2/(\Delta k k_1)dk_2$. Both μ_1 and μ_3 can now be replaced by Δk and k_2, respectively. Noting that integrating with μ_3 between -1 and 1 is equivalent to integrating between where $\boldsymbol{k_1}$ and $\boldsymbol{k_3}$ are parallel to where they are anti-parallel we can obtain the corresponding Δk interval $[|k-k_3|, k_3+k]$. A similar argument can be applied to find the extremes of the k_2 integral resulting in:

$$\left.\frac{\partial f(k)}{\partial t}\right|_{\text{el}-\text{el}} = \frac{2\pi}{\hbar}\frac{\Omega^2}{(2\pi)^6}(2\pi)^2\frac{1}{k}\iint k_1k_3dk_1dk_3\int_{|k-k_3|}^{k+k_3} d\Delta k\left(\frac{e^2}{\varepsilon_0\Omega}\frac{1}{\Delta k^2+\kappa^2}\right)^2 \\ \times\int_{|k_1-\Delta k|}^{k_1+\Delta k} dk_2k_2\left[f_{\boldsymbol{k}_3}f_{\boldsymbol{k}_1}(1-f_{\boldsymbol{k}})\left(1-f_{\boldsymbol{k}_2}\right) - f_{\boldsymbol{k}}f_{\boldsymbol{k}_2}\left(1-f_{\boldsymbol{k}_3}\right)\left(1-f_{\boldsymbol{k}_1}\right)\right]\delta\left(\frac{\hbar^2}{2m_e}\left(k_3^2+k_1^2-k_2^2-k^2\right)\right). \tag{4.8}$$

The last integral can be solved with the Dirac-δ resulting in $m_ek_2/(\hbar^2k_2)\mathcal{F}$ (with $\mathcal{F}$ the Pauli blocking terms) subject to $k^2 = k_3^2 + k_1^2 - k^2$ and $|k_1 - \Delta k| \le k_2 \le k_1 + \Delta k$, which is equivalent to $|k_2 - k_1| \le \Delta k \le k_1 + k_2$, introduced as new constraint on the Δk integral. Writing it alone, it will be possible to analytically solve it:

$$\int_{\max\{|k-k_3|,|k_2-k_1|\}}^{\min\{k+k_3,k_2+k_1\}} d\Delta k\left(\frac{e^2}{\varepsilon_0\Omega}\frac{1}{\Delta k^2+\kappa_{\text{ab}}^2}\right)^2 = \left(\frac{e^2}{\varepsilon_0\Omega}\right)^2\frac{1}{2\kappa_{\text{ab}}^3}\left[\arctan\frac{\Delta k}{\kappa_{\text{ab}}} + \frac{\Delta k\kappa_{\text{ab}}}{\Delta k^2+\kappa_{\text{ab}}^2}\right]_{\max\{|k-k_3|,|k_2-k_1|\}}^{\min\{k+k_3,k_2+k_1\}}. \tag{4.9}$$

The integral we are left with to solve numerically is then:

$$\left.\frac{\partial f(k)}{\partial t}\right|_{\text{el}-\text{el}} = \frac{2\pi}{\hbar}\frac{\Omega^2}{(2\pi)^6}\frac{(2\pi)^2}{k}\frac{m_e}{\hbar^2}\left(\frac{e^2}{\varepsilon_0\Omega}\right)^2\frac{1}{2\kappa_{\text{ab}}^3}\iint_{k_1^2+k_3^2\ge k^2} k_1k_3dk_1dk_3\mathcal{F}\left[\arctan\frac{\Delta k}{\kappa_{\text{ab}}} + \frac{\Delta k\kappa_{\text{ab}}}{\Delta k^2+\kappa_{\text{ab}}^2}\right]_{\max\{|k-k_3|,|k_2-k_1|\}}^{\min\{k+k_3,k_2+k_1\}} \tag{4.10}$$

still subject to $k_2^2 = k_1^2 + k_3^2 - k^2$. The condition $k_1^2 + k_3^2 \ge k^2$ comes from the that Δk^2 is positive, used when collapsing the δ integral.

Now regarding the electron-ion-photon collision term, written in equation 2.13, the sum can be first transformed, through the procedure discussed above, in a triple integral. The azimuthal integration can be performed immediately, resulting in:

$$\left.\frac{\partial f(\boldsymbol{k})}{\partial t}\right|_{\text{el}-\text{ion}-\text{phot}} = \frac{2\pi}{\hbar}\frac{\Omega}{(2\pi)^3}\int_0^\infty d\Delta k\Delta k^2\left(\frac{e^2}{\varepsilon_0\Omega}\frac{1}{\Delta k^2+\kappa^2}\right)^2 \sum_\ell J_\ell^2\left(\frac{eE_L\Delta k\mu}{m_ew_L^2}\right) \\ \times\int_{-1}^1 dp\left[f_{|k+\Delta k|}(1-f_k) - f_k\left(1-f_{|k+\Delta k|}\right)\right]\delta\left(\frac{\hbar^2}{2m_e}(\boldsymbol{k}+\boldsymbol{\Delta k})^2 - \frac{\hbar^2}{2m_e}\boldsymbol{k}^2 + \ell\hbar\omega_L\right) \tag{4.11}$$

with $\mu = \cos\angle(\boldsymbol{E}, \boldsymbol{\Delta k})$ and $p = \cos\angle(\boldsymbol{k}, \boldsymbol{\Delta k})$. Having defined the polar angle of $\boldsymbol{\Delta k}$ in such a fashion the equality $(\boldsymbol{k}+\boldsymbol{\Delta k})^2 = k^2 + \Delta k^2 - 2k\Delta kp$ can also be written, from which the last integral becomes:

$$\int_{-1}^{1} dp\left[f_{|k+\Delta k|}(1-f_k)-f_k\left(1-f_{|k+\Delta k|}\right)\right]\delta\left(\frac{\hbar^2}{2m_e}\Delta k^2-\frac{\hbar^2 pk\Delta k}{m_e}+\ell\hbar\omega_L\right)$$
$$=\frac{m_e}{\hbar^2 k\Delta k}\left[f_{|k+\Delta k|}(1-f_k)-f_k\left(1-f_{|k+\Delta k|}\right)\right]_{p\in[-1,1]} \text{ with } p=\left(\Delta k^2+\ell 2m_e\omega_L/\hbar\right)/(2k\Delta k)\in[-1,1]. \tag{4.12}$$

As an average over all laser light polarizations is to be considered (discussed in section 2.2.2), the Bessel function sum in equation 4.11 is averaged over all μ according to:

$$\left\langle J_\ell^2\left(\frac{eE_L\Delta k}{m_e\omega_L^2}\right)\right\rangle_\mu := \frac{1}{2}\int_{-1}^{1} J_\ell^2\left(\frac{eE_L\Delta k}{m_e\omega_L^2}\mu\right)d\mu. \tag{4.13}$$

Thus the collision term modeling IB absorption that needs to be solved analytically takes the form:

$$\left.\frac{\partial f(k)}{\partial t}\right|_{\text{el-ion-phot}}=\frac{2\pi}{\hbar}\frac{\Omega}{(2\pi)^3}2\pi\frac{m_e}{\hbar^2 k}\left(\frac{e^2}{\varepsilon_0\Omega}\right)^2\int_0^\infty d\Delta k\Delta k\left(\frac{1}{\Delta k^2+\kappa^2}\right)^2\times$$
$$\sum_\ell\left\langle J_\ell^2\left(\frac{eE_L\Delta k}{m_e\omega_L^2}\right)\right\rangle_\mu\left[f(|k+\Delta k|)(1-f(k))-f(k)(1-f(|k+\Delta k|))\right]\Big|_{p\in[-1,1]} \tag{4.14}$$

With $|k+\Delta k|^2=k^2+\Delta k^2-2k\Delta kp$ and $p=\left(\Delta k^2+\ell 2m_e\omega_L/\hbar\right)/(2k\Delta k)\in[-1,1]$.

4.3.2 Algorithm

By adding the two analytically simplified terms in equations 4.10 and 4.14, we obtain the time derivative of the distribution function of the electrons. Using a finite differences framework the time evolution of the distribution can be solved. Algorithms 2 and 3 describe the process of solving the Boltzmann equation and obtaining the XUV transmission. The e-i-pt collision term as written in equation 4.14 requires the electric field inside the material, as an input parameter. To calculate it, the average incident fluence of each sub-zone was converted to intensity through equation 4.2 and subsequently the formula $E_L(t)=\sqrt{2I(t)/(c\varepsilon_0)}$ was applied. Note also that $J_\ell^2(x)=J_{-\ell}^2(x)$, which is going to be used below.

3D tensors are required to calculate the integrand: for the e-i-pt term one dimension is required for the different Bessel function orders and two for k and Δk; and for the e-e term three dimensions are required for k, k_1 and k_3, with k_2 pre-determined. As such, all coordinate-dependent tensors, not expected to change in time, were calculated before the time iterations, to ensure the minimal amount of burdensome calculations required. This can be seen in algorithm 2.

The momentum scale was tuned for the lowest possible cut-off point that still allows for particle conservation in the highest fluence zone. The temporal scale, on the other hand, was defined based on a study of the maximum time step possible for a given fluence. Naturally, as the fluence increases the electrons move faster through momentum space, requiring a smaller time step (or higher number of total steps). A linear fit was then performed to the number of time steps needed (obtained from experimentation), as a function of the fluence. The results were used to define the time step.

The number of Bessel function orders to be considered also had to be decided, since our high laser intensity causes multiphoton absorption processes to be non-negligible. To assess where the cut-off should be, the sum of all orders of the Bessel function, integrated in Δk, averaged in μ, and pondered by the number of absorbed photons was plotted, versus the electric field intensity inside the material, for different cut-off values, in figure

4.20. The E_L range was calculated from the average absorbed fluences and adjusted so that it achieves field intensities comparable to the ones received by the highest fluence zone being considered, the inner zone of the 150 μJ family. The pondered sum increases, for higher E_L, as more orders of the Bessel functions are included. As this sum is proportional to the number of absorbed photons, this is a demonstration of the need to include several orders o the Bessel function, not in the least because the number of absorbed photos is not expected to decrease with E_L as in figure 4.20a. Figures 4.20b and 4.20c, on the other hand, have identically behaved sums, linearly increasing with E_L, and the same numerical values. This implies that orders above 30 do not need to be considered, in our case.

Algorithm 2 The Boltzmann equation, used as a physical forward model. The multiplicative constant with * is changed in some circumstances. Here the tensors of constants (in time) are precalculated.

Boltzmann(F, κ_{ei}, κ_{ee}, m_{eff}, ε_t)

$k_{\text{prov}} \leftarrow [0, 0.00008, 0.00016, ..., 8]\ a_B$
$e_{tested} \leftarrow [0.0016, 0.0032, ..., 81.6]\ E_h$ ▷ e_{test} := range of energies to be tested for the Fermi Energy.
$T_e \leftarrow 300$ K
$i \leftarrow 0$
while $\int f_{eq}(k_{\text{prov}}, e_{test}[i], T_e, m_{eff}) \cdot D(k_{\text{prov}}, m_{eff}) \cdot \hbar^2/m_{eff} \cdot dk_{\text{prov}} \neq n_e$ **do**
  $i \leftarrow i + 1$ ▷ $f_{eq}(k_{\text{prov}}, e_{test}[i], T_e, m_{eff})$ corresponds to the Fermi-Dirac function.
end while
$\{e_F, k_f\} \leftarrow \{e_{test}[i], 2e_F m_{eff}/\hbar\}$
$k, k_1, k_3, \Delta k \leftarrow [10^{-21}, (7 \cdot k_f - 10^{-21})/100, 2 \cdot (7 \cdot k_f - 10^{-21})/100, ..., 7^* \cdot k_f]\ a_B^{-1}$
$f(k) \leftarrow f_{eq}(k, e_{test}[i], T_e, m_{eff})$ ▷ This is the initial condition of our distribution function.

$\mu \leftarrow [-1, -0.98, ...1]$
$d\mu \leftarrow \mu[2] - \mu[1]$
orders $\leftarrow 25$ ▷ Number of orders of the Bessel function that will be considered.
$t_1 \leftarrow [0, 200/n, 2 \cdot 200/n, ..., 200]$ fs with $5n/3 = F/(5.385) + 300$.
$t_2 \leftarrow [200 + (1/n), 200 + (1/n) + (500 - 200 - 1/n)/n, ..., 500]$ fs with $5n/2 = F/(5.385) + 300$. ▷ n was studied for proper convergence of the algorithm, as described below.
$\{dt_1, dt_2\} \leftarrow \{t_1[2] - t_1[1], t_2[2] - t_2[1]\}$
$E_L \leftarrow E_L(t_1, F)$ ▷ E_L := Laser electric field array, peaking at 100 fs. F := average fluence of the zone being tested.

for j in [0,1,...,orders] **do**
  $\{p[j], p^-[j]\} \leftarrow \{1/(2k) \otimes \left(\Delta k^2 + 2jm_{eff}\omega_L \cdot I/\hbar\right), 1/(2k) \otimes \left(\Delta k^2 - 2jm_{eff}\omega_L \cdot I/\hbar\right)\}$ ▷ I := vector of ones the size of k_1, k_3, etc. p := variable of integration in equation 4.14.
  $\{p_{\text{bool}}[j], p_{\text{bool}}^{-1}[j]\} \leftarrow \{$True where $p[j] \in [-1, 1]$ False elsewhere.,True where $p^{-1}[j] \in [-1, 1]$ False elsewhere.$\}$
  $\{a[j], a^-[j]\} \leftarrow \{k^2 \otimes I + I \otimes \Delta k^2 - 2 \cdot p[j] \cdot k \otimes \Delta k, k^2 \otimes I + I \otimes \Delta k^2 - 2 \cdot p^-[j] \cdot k \otimes \Delta k\}$ ▷ a, a^- := $|k - \Delta k|^2$ both for the positive and negative Bessel functions orders.
end for

$e \leftarrow -k^2 \otimes I \otimes I + I \otimes k_1^2 \otimes I + I \otimes I \otimes k_3^2$
$e_{\text{bool}} \leftarrow$ True where $e \in [0, +\infty]$ False elsewhere. ▷ e_{bool} := used for the $k_1^2 + k_3^2 \geq k^2$ condition.
$k_2^2 \leftarrow -k^2 \otimes I \otimes I + I \otimes k_1^2 \otimes I + I \otimes I \otimes k_3^2$ where e_{bool} ==True, 0 elsewhere.
$\{\Delta k_{\text{up}}, \Delta k_{\text{down}}\} \leftarrow \{\text{minimum}(k \otimes I \otimes I + I \otimes I \otimes k_3, I \otimes k_1 \otimes I + \sqrt{k_2^2}), \text{maximum}(|k \otimes I \otimes I - I \otimes I \otimes k_3|, |\sqrt{k_2^2} - I \otimes k_1 \otimes I|)\}$ ▷ $\Delta k_{\text{up}}, \Delta k_{\text{down}}$:= limits of integration of equation 4.9. ▷ The maximum and minimum functions are element-wise.

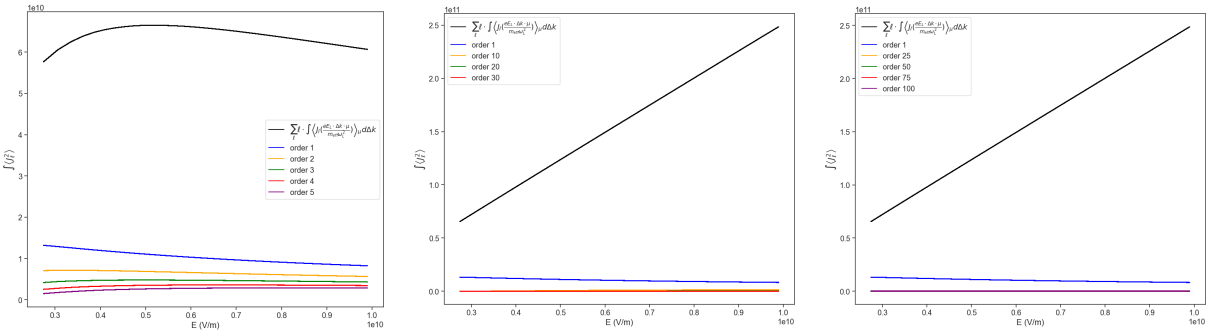

(a) For orders 0 through 5. (b) For orders 0 through 30. (c) For orders 0 through 100.

Figure 4.20: $\sum_\ell \ell \cdot \int \left\langle J_l(\frac{eE_L \cdot \Delta k \cdot \mu}{m_{eff}\omega_L^2}) \right\rangle_\mu d\Delta k$ as a function of E_L, in black. $\int \left\langle J_l(\frac{eE_L \cdot \Delta k \cdot \mu}{m_{eff}\omega_L^2}) \right\rangle_\mu d\Delta k$ for select orders of the Bessel function in different colors.

Algorithm 3 Continuation of algorithm 2. Here the time iteration is performed, within the finite-differences framework, to find the non-equilibrium distribution function, at each time step.

for i in [0,1,...,length(t_1)] **do**

  for j in orders **do**
    $B_{av}[j] \leftarrow 1/2 \cdot \int J_j^2(e \cdot E_L[i]/(m_{eff} \cdot w_L^2) \cdot \otimes \mu) d\mu$ ▷ J_l is a Bessel function of order ℓ and first kind.
  end for
  $f(k) \leftarrow \text{spline}(f(k))$
  for j in [0,1,...,orders] **do**
    $\{f_{\Delta k}[j], f_{\Delta k}^-[j], f_k\} \leftarrow \{f(a[j]), f(a^-[j]), f(k \otimes I)\}$
    $\{\mathcal{F}_{ei}, \mathcal{F}_{ei}^-\} \leftarrow \{f_{\Delta k}(1-f_k) - f_k(1-f_{\Delta k}), f_{\Delta k}^-(1-f_k) - f_k(1-f_{\Delta k}^-)\}$
  end for
  $B_{av} \leftarrow B_{av} \otimes I$
  $B_{av}[0] = 1/2 \cdot B_{av}[0]$ ▷ The zeroth order is counted in both the positive and negative order terms of the sum over ℓ.
  $\kappa^2 \leftarrow \kappa_{ei}^2 \cdot e^2 m_{eff}/(\pi^2\hbar^2\varepsilon_0) \cdot \int f(k) dk$
  $\{M_{ei}, M_{ei}^-\} \leftarrow \{m_{eff}e^4/(\hbar^3 \cdot 2\pi\varepsilon_0^2\Omega) \cdot (1/k) \otimes (\Delta k/(\Delta k^2 + \kappa^2)^2)$ where $p_{\text{bool}} ==$ True. Else 0., $m_{eff}e^4/(\hbar^3 \cdot 2\pi\varepsilon_0^2\Omega) \cdot (1/k) \otimes (\Delta k/(\Delta k^2 + \kappa^2)^2)$ where p_{bool}^-==True. Else 0.$\}$
  $\delta f_{ei} \leftarrow \sum_{\ell=[0,1,\ldots,\text{orders}]} \int (M_{ei} \cdot \mathcal{F} \cdot B_{av} + M_{ei}^- \cdot \mathcal{F}^- \cdot B_{av}) dk_3$

  $\{f, f_1, f_2, f_3\} \leftarrow \{f(k \otimes I \otimes I), f(I \otimes k_1 \otimes k_3), f(\sqrt{k_2^2}), f(I \otimes I \otimes k_3)\}$
  $\mathcal{F}_{ee} \leftarrow f_3 f_1 (1-f)(1-f_2) - f f_2 (1-f_3)(1-f_1)$
  $\kappa^2 \leftarrow \kappa_{ee}^2 \cdot e^2 m_{eff}/(\pi^2\hbar^2\varepsilon_0) \cdot \int f(k) dk$
  $M_{ee} \leftarrow m_{eff}e^4/(2(2\hbar\pi)^3\varepsilon_0^2\kappa^3) \cdot (1/k) \otimes k_1 \otimes k_3$ where e_{bool} ==True, else 0.
  $I \leftarrow \arctan(\Delta k_{\text{up}}) + \Delta k_{\text{up}}\kappa/(\Delta k_{\text{up}}^2 + \kappa^2 \otimes I) - \left(\arctan(\Delta k_{\text{down}}) + \Delta k_{\text{down}}\kappa/(\Delta k_{\text{down}}^2 + \kappa^2 \otimes I)\right)$
  $\delta f_{ee} \leftarrow \iint M_{ee} \cdot I \cdot \mathcal{F}_{ee} dk_3 dk_1$

  $M[k] \leftarrow T_r(\varepsilon_t, f)$ ▷ T_r form equation 4.1.
  $f(k) \leftarrow f(k) + (\delta f_{ei} + \delta f_{ee}) \cdot dt_1$
end for

for k in len(t_2) **do**
  $k \leftarrow k + len(t_1)$
  Repeat previous "for" cycle but without electron ion calculations.
end for

Return M

Finally, algorithm 3 is the continuation of algorithm 2, in which the tensors defined in the former are used

to calculate the collision integral for each time-step over a total of 500 fs. The packages used to perform the computational task were again *NumPy* and *SciPy*. The spline function, refers to a cubic spline with the *InterpolatedUnivariateSpline* tool of *SciPy* the integrals were performed with Simpson's rule by *SciPy*'s *simps* package.

4.3.3 Analysis of solutions

Having described the algorithm used to solve equation 2.9 without the phonon term, we will now discuss the solutions. Figure 4.21 displays $f(k,t)$ at three different time steps of the Boltzmann equation model solved for $F = 3900$ J/m^2, $\kappa_{ee} = \kappa_{ie} = 1$ and $m_{eff} = m_e^0$. In figure 4.21a, the initial effect of the laser irradiation becomes clear, when observing the step-like structure of $f(k,t)$: electrons below the Fermi energy are removed and added 1.55 eV or multiples of that above their initial energy. This only happens near the Fermi edge because Pauli blocking prevents electrons from jumping to occupied spaces. Roughly 10 fs after the first snapshot, and before most of the pulse energy has been deposited in the sample, the difference between $f(k,t)$ and a Fermi-Dirac function is negligible, as is shown in figure 4.21b. This is due to the e-e collisions that quickly thermalize the distribution.

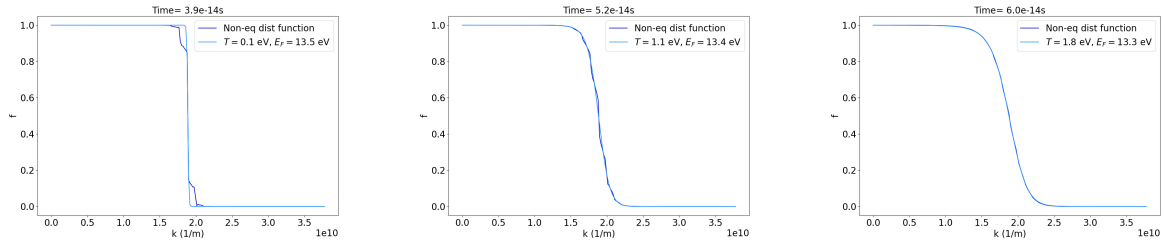

(a) Simulation for $t = 39$ fs. (b) Simulation for $t = 52$ fs. (c) Simulation for $t = 60$ fs.

Figure 4.21: Analytical solution of equation 2.9, without the phonon term, at different time steps, for $F = 3900$ J/m^2, $\kappa_{ee} = \kappa_{ie} = 1$ and $m_{eff} = m_e^0$. Here, as in the TTM section, laser intensity peaks at 100fs. The light blue line corresponds to a fit of a Fermi Dirac function to the obtained non-equilibrium $f(k,t)$.

To further understand how the model functions, the results of different simulations with all but one of the free parameters kept constant were performed. Figure 4.22 displays three different model runs (the same time step for the three), all performed for $F = 3900$ J/m^2, $\kappa_{ee} = 1$ and $m_{eff} = m_e^0$ but with increasing vales of κ_{ie} from left to right. It is clear that, exposed to the same laser fluence, an increase in κ_{ie} decreases the total amount of energy density deposited in the sample.

Remembering that κ is the inverse of the screening radius of the Coulomb potential, in this specific case the Coulomb potential intermediating the e-i collisions necessary for IB absorption, we can explain this decrease. For higher κ_{ie} the potential is more shielded and becomes more localized, reducing the e-i collisions. As a result, photons are absorbed less often, resulting in reduced energy density and a longer decay length of the electric field inside the material. The latter point suggests κ_{ie} controls the skin depth.

Moving on to the effects of κ_{ee}, figure 4.23 displays the solutions to the 3 different runs of the Boltzmann model, at 100 fs, but for increasing κ_{ee} and all other parameters constant. Here, all three cases show a

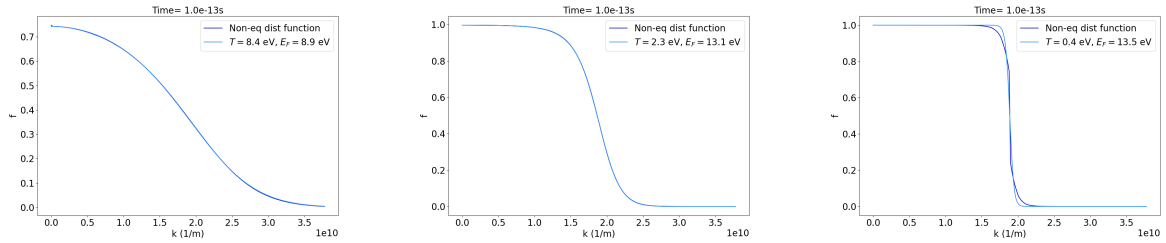

(a) Simulation for $\kappa_{ie} = 1$. (b) Simulation for $\kappa_{ie} = 2.5$. (c) Simulation for $\kappa_{ie} = 5$.

Figure 4.22: Analytical solution of equation 2.9, without the phonon term, at 100 fs, for 3 different simulations run with $F = 3900$ J/m^2, $\kappa_{ee} = 1$, $m_{eff} = m_e^0$ and different κ_{ie}. Here, as in the TTM section, laser intensity peaks at 100fs. The light blue line corresponds to a fit of a Fermi Dirac function to the obtained non-equilibrium $f(k, t)$.

similar T_e when fitted to a Fermi Dirac. On the other hand, as κ_{ee} increases the step-like structure of the distribution becomes more pronounced. This is the imprint the laser itself leaves on the electronic distribution when being absorbed, since it can only move electrons by 1.55 eV (energy of a single photon) or multiples of that, and is a clear sign of slower thermalization of the electron gas with itself. The physical reasoning for this increased thermalization time for higher κ_{ee} is similar to before: a more localized scattering potential between the electrons, resulting from an increase in inverse screening length, leads to less e-e collisions which are responsible for thermalization of $f(k, t)$ to an equilibrium Fermi-Dirac, and to a longer relaxation time.

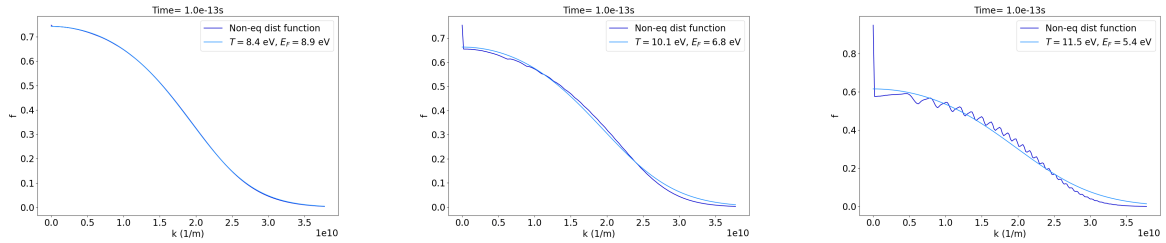

(a) Simulation for $\kappa_{ee} = 1$. (b) Simulation for $\kappa_{ee} = 2.5$. (c) Simulation for $\kappa_{ee} = 5$.

Figure 4.23: Analytical solution of equation 2.9, without the phonon term, at 100fs, for 3 different simulations run with $F = 3900$ J/m^2, $\kappa_{ie} = 1$, $m_{eff} = m_e^0$ and different κ_{ee}. Here, as in the TTM section, laser intensity peaks at 100fs. The light blue line corresponds to a fit of a Fermi Dirac function to the obtained non-equilibrium $f(k, t)$.

Finally, the electronic mass parameter effects on the simulations can be deduced from figure 4.24, where all parameters were kept steady except for an increasing m_{eff} from left to right. The time step chosen for all figures was 40 fs, before broad thermalization so the differences in laser-absorption-driven changes in $f(k, t)$ could be studied. From the figure, we can see that the step-like structures become wider with increasing m_{eff}. This effect is tied to the quasi-free dispersion relation $\varepsilon(k) = \hbar^2 k^2/(2m_{eff})$. Higher mass implies that a smaller increase in energy is required to achieve a bigger wave vector. As such, the 1.55 eV of energy deposited goes further, in terms of wave vector, than before. Furthermore, after the laser has deposited all its energy in the three simulation runs of figure 4.24, $T_e^{\max}$ is smaller for bigger effective masses. Physically, heavier electrons can accept more energy without changing their temperature as much as lighter ones. In this

way, the m_{eff} controls the heat capacity of the electron gas and, consequently, the T_e of any sub-zone.

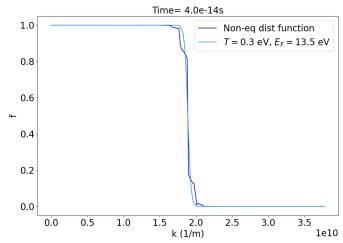

(a) Simulation for $m_{eff} = m_e^0$.

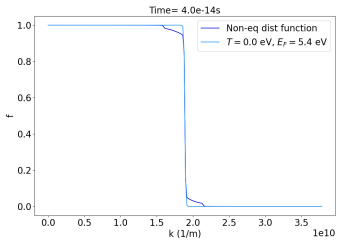

(b) Simulation for $m_{eff} = 2.5 \cdot m_e^0$.

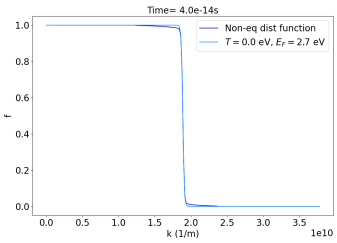

(c) Simulation for $m_{eff} = 5m_e^0$.

Figure 4.24: Analytical solution of equation 2.9, without the phonon term, at 100fs, for 3 different simulations run with $F = 3900$ J/m^2, $\kappa_{ie} = \kappa_{ee} = 1$, and different $_{eff}$. Here, as in the TTM section, laser intensity peaks at 50 fs. The light blue line corresponds to a fit of a Fermi Dirac function to the obtained non-equilibrium $f(k, t)$.

4.3.4 MCMC searches

Two different types of MCMC searches were deployed taking advantage of the described physical forward model. The first one was a search for the joint posterior distribution of the three different sub-zones of the 150 μJ family of data series. In this search, all the zones share the relevant physical parameters and only the incident fluence changes from one to the next. In the second search, a different MCMC was run for each of the sub-zones. Here the posterior being sampled in each MCMC is related to the data of that sub-zone only. The physical parameters are free to float from one zone to the next, according to the ensemble evolution of their own MCMC. The searches themselves were initialized and run using the techniques described in section 4.2.

Joint search

Figure 4.25 displays the 2D correlation and marginalized posterior distributions of the Boltzmann model free parameters. They were obtained from an MCMC search of the joint posterior distribution of all the sub-zones of the data family with 150 μJ. From the marginalized posteriors, we can extract the central estimates and 1σ error bar of or free parameters, as was done before, resulting in $\kappa_{ie} = 1.03^{+0.05}_{-0.05}$, $\kappa_{ee} = 1.25^{+0.47}_{-0.24}$, $m_{eff} = 1.61^{+0.29}_{-0.38}$ and $\varepsilon_t = -7.02^{+1.67}_{-1.44}$. The two screening parameters κ_{ie} and κ_{ee} are close to 1, the result expected for a quasi-free electron gas. The e-i screening coefficient has a very small relative error but, even so, is compatible with $\kappa_{ie} = 1$. The effective mass estimate is above one, which is not unexpected given the strongly peaked d-orbitals at the beginning of the Ti continuum and near the Fermi energy (figure 2.3).

Looking more closely at the 2-dimensional correlations of the posterior distribution, only a strong direct correlation between the effective mass and ε_t stands out. The correlation can be explained along similar lines to the ones used in section 4.2. All else being equal, a lower ε_t - corresponding to the HHG pulse exciting electrons to further away from the Fermi energy -, requires a higher equivalent T_e to get the same amount of transmission drop. One of the ways of obtaining a higher equivalent T_e, for the same absorbed fluence, is

to reduce the effective electronic mass thus reducing heat capacity. Interestingly, no similar correlation can be said to exist between the k_{ie} parameter and ε_t, as one might expect. From an algorithmic perspective, it remains unclear why this is the case since both parameters affect the equivalent T_e. The best hypothesis we can put forward is that the κ_{ie} parameter affects the different sub-zones differently, thus while one zone might be getting optimized with changes to κ_{ie} some other will fall out of agreement dramatically.

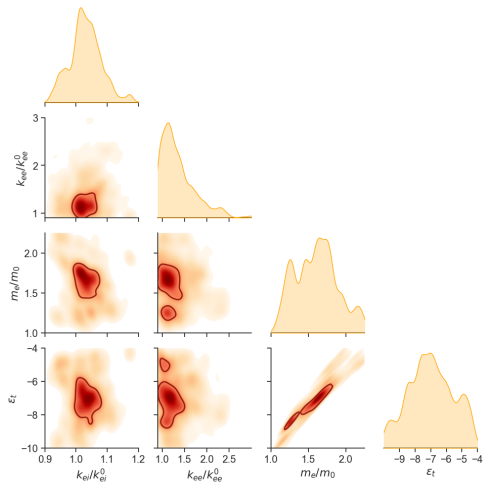

Figure 4.25: 2D correlations and marginalized posterior distributions of the free parameters of a physical forward model based on the Boltzmann equation 2.9, without the phonon term. Estimated via MCMC search, with an ensemble of 40 walkers, evolved for a total of 15000 model evaluations. 10000 evaluations discarded as burn-in. Family of 150 μJ data series utilized. The darker line on the 2D correlation is the 1σ band.

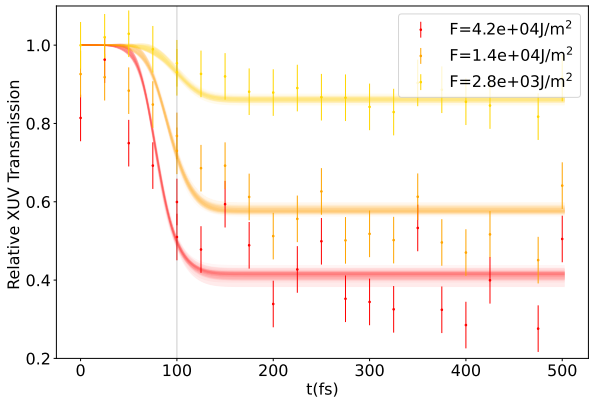

Figure 4.26: 50 model runs with parameters sampled independently from the ensemble generated by the MCMC search, for a physical forward model of the Boltzmann equation 2.9, without the phonon term, plotted on top of the experimental data. In log scale with the laser fluence peaking at 100 fs.

Figure 4.26 plots the forward model results from fifty model runs, using fifty sets of parameters, independently chosen from the ensemble MCMC-generated ensemble, overlaying the obtained data series. Reasonable agreement is found between both, in terms of the slope of the fall and of the level of stabilization of transmission. The most striking exceptions are in the earlier moments of the highest fluence data series. The way the observable is calculated in the forward model (equation 4.1) does not allow for XUV transmission values other than one, before energy deposition, making the model rigid at earlier time steps. Better agreement between the slope of the model and acquired data might also be obtained if the value of ε_t was allowed to relax over time, to somewhat include the shifts in energy of the DOS as T_e increases (figure 2.3), that lead to energy shifts between the core $3p$ state and a given part of the continuum.

The fact that strong agreement is found for free electron-like parameters is notable. As discussed in the introduction, WDM is difficult to model due to the fact that it sits in a region where solid matter and plasma physics methods collide. Here, the results from a first principles model, seem to indicate only a slight material dependence of the model results (specifically in the effective mass). For the experimental conditions of our sample, the electronic population behaves like a nearly-free, fast-thermalizing, electron gas. Both the closeness of the shape of fall in transmission to that of the TTM-modeled one; and observing the Boltzmann model runs,

with the parameters set to their central estimates, converging in tens of fs to a hot Fermi-Dirac distribution, validate the TTM assumptions of instantaneous thermalization of the electron gas, with itself, for our time resolution.

Figure 4.27 displays the estimate, performed as in section 4.2, of the electronic heat capacity as a function of temperature. It has a shape congruent with a free-electron-like DOS (the blue line for Al), which was expected due to the nearly free DOS assumption of the model. The absolute value of the extracted heat capacity is, however, significantly lower than the theoretical predictions. Figure 4.28 is very similar to the same data points plotted for the TTM, in all cases. This is due to the MCMC walkers being more likely to sample regions of high agreement with the data. In this sense, only T_e is truly predicted from the forward model, while the minimal XUV transmission is bounded by the observed data. The disagreements between the finite temperature DFT predictions are, as before, hypothesized as coming from the poor estimation of the distance between the $3p$ and continuum states, of the DFT methods.

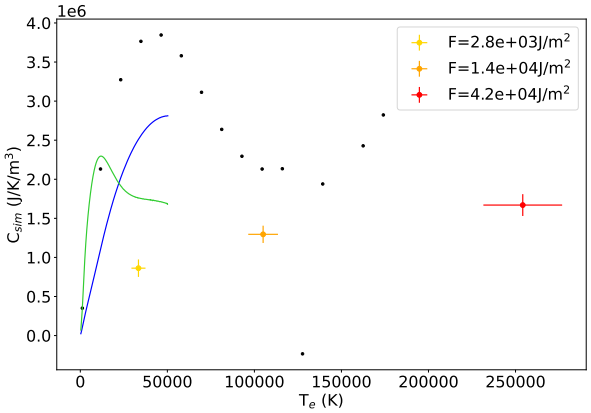

Figure 4.27: C_e vs maximum T_e, for each sub-zone considered, calculated from equation 4.6. Central estimate and error bars obtain by sampling 50 model runs, from MCMC search results for a physical forward model of the Boltzmann equation 2.9. The light green line is Lin's result ([41]) for a cold Ti DOS and the dark blue line refers to calculations with the same formula but an Al (or FEG-like) DOS. The black dots are the heat capacity estimates from a finite temperature DFT simulation with a cold lattice.

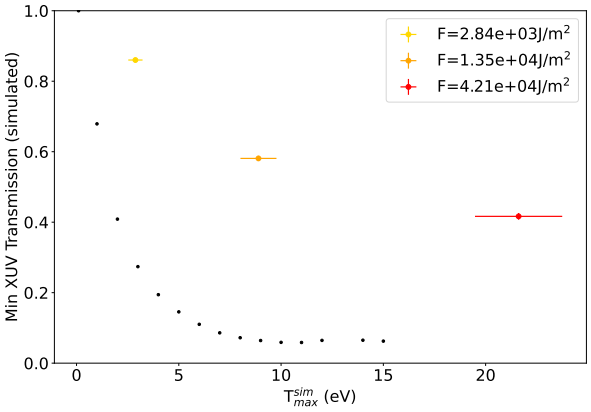

Figure 4.28: Minimum XUV transmission vs maximum T_e, for each sub-zone considered. Central estimate and error bars obtain by sampling 50 model runs, from MCMC search results for a physical forward model of the Boltzmann equation 2.9. The black dots are the optical response properties estimates from a finite temperature DFT simulation with a cold lattice.

Both detailed collision terms we have been working with can be interpreted as providing relaxation times as a function of wave vector. Going back to equation 2.7, we can re-write it, drawing inspiration from the relaxation time approach, as:

$$I^{\text{out}}(\mathbf{k}) = -\frac{f_{\mathbf{k}}}{\tau_{\text{out},\mathbf{k}}} + \frac{1-f_{\mathbf{k}}}{\tau_{\text{in},\mathbf{k}}}, \text{ with } \frac{1}{\tau_{\text{out},\mathbf{p}}} = \int_{\mathbf{k}_2,\mathbf{k}_3,\mathbf{k}_1} W_{\mathbf{k}\mathbf{k}_2,\mathbf{k}_1\mathbf{k}_3} f_{\mathbf{k}} \left(1-f_{\mathbf{k}_3}\right)\left(1-f_{\mathbf{k}_1}\right), \; \frac{1}{\tau_{\text{in},\mathbf{k}}} = \int_{\mathbf{k},\mathbf{k}_3,\mathbf{k}_1} W_{\mathbf{k}_3\mathbf{k}_1,\mathbf{k}_2\mathbf{k}} f_{\mathbf{k}_3} f_{\mathbf{k}_1} \left(1-f_{\mathbf{k}}\right). \tag{4.15}$$

To provide a single value for time step (or T_e) and averaging procedure become necessary. In this case we

consider all electrons and holes that could participate in the scattering, resulting in:

$$\langle \tau_{\text{out},\mathbf{k}} \rangle = \frac{\int_{\mathbf{k}} f_{\mathbf{k}} \cdot \tau_{\text{out},\mathbf{k}}}{\int_{\mathbf{k}} f_{\mathbf{k}}} \text{ and } \langle \tau_{\text{in},\mathbf{k}} \rangle = \frac{\int_{\mathbf{k}} (1 - f_{\mathbf{k}}) \cdot \tau_{\text{in},\mathbf{k}}}{\int_{\mathbf{k}} (1 - f_{\mathbf{k}})}. \tag{4.16}$$

A similar procedure can be followed for e-e collisions. Overall we obtain plots like figures 4.29 and 4.30. Figure 4.29 is comparable to figure 1.4, although for a non-equilibrium situation with cold ions. It shows an increasing collision frequency with increasing temperature. This behavior is also patent in figure 1.4. The results shown here, however, point to a lower collision frequency, especially at lower energies, which might result from the fact that no phonon collisions are being considered. At higher energies, these collisions lose their relative importance and so we see ν_{ie} behaving more like the results in figure 1.4. Figure 4.30 shows a steep increase in e-e collisions with increasing energy, compatible with less restrictive Pauli blocking freeing electrons to participate in scattering events, as the ensemble heats up. For T_e upwards of 10 eV the collision frequency is on the order of the plasma frequency, an encouraging result.

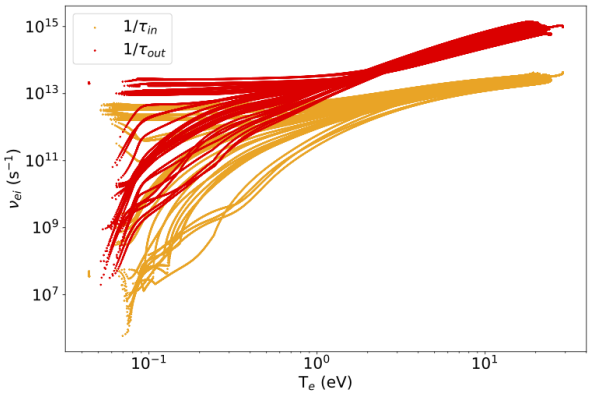

Figure 4.29: Average e-e collision rates calculated from equation 4.16, as a function of T_e, for 50 different model runs. Each continuous line corresponds to results of a model run.

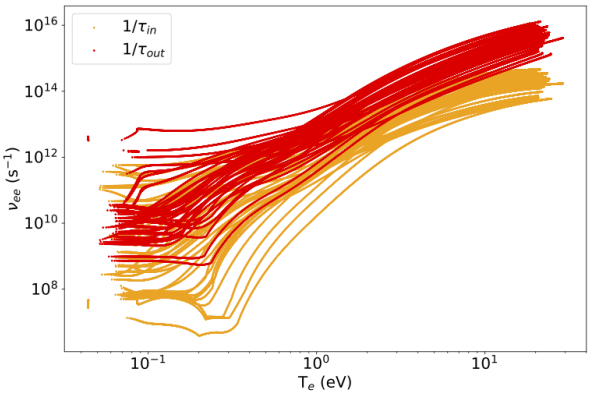

Figure 4.30: Average e-e collision rates calculated from equation 4.16, as a function of T_e, for 50 different model runs. Each continuous line corresponds to the results of a model run.

The Γ and Θ parameter, discussed in 1.2.2, can also be calculated by resorting to the equivalent T_e and μ form a Fermi-Dirac fit, performed for every configuration of $f(k)$ the model goes through, and the formula $n_e = \hbar^2/m_{eff} \cdot \int D(k, m_{eff}) f(k) k dk$. These parameters will allow us to properly place the created non-equilibrium plasma in the phase diagram of figure 1.3. Figure 4.31 shows the degeneracy parameter calculated for the lowest and highest fluency sub-zones. The middle sub-zone was not plotted, since the calculations become numerically unstable near $\mu \sim 0$ and produce big error bars that distort the scale. As the blue line also shows, close to $\Theta \sim 1$ there should be a transition from positive to negative chemical potential, indicating a transition to a classical system as the plasma heats up and this is what is observed.

The plasma parameter Γ, calculated for maximal T_e and corresponding densities, for each of the sub-zones considered, is plotted in figure 4.32. As we move to higher fluence zones, T_e increases and, with it, we see a steep decrease in Γ- i.e closer to classical plasma behavior. For the highest fluence zone $\Gamma \sim 2$ was achieved.

This result is consistent with our physical expectations: an increase in T_e increases electronic kinetic energy and makes their behavior closer to that of free uncorrelated particles, even before the density parameter changes

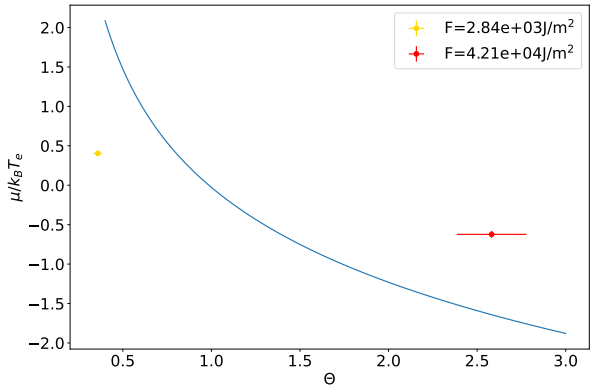

Figure 4.31: Chemical potential μ/k_BT_e as a function of the degeneracy parameter calculated form equation 1.5, for the maximal T_e of the sub-zone in question. Central estimate and error bars obtain by sampling 50 model runs, from MCMC search results for a physical forward model of the Boltzmann equation 2.9. The blue line corresponds to the interpolating fit between the two degeneracy regimes shown in figure 1.2.

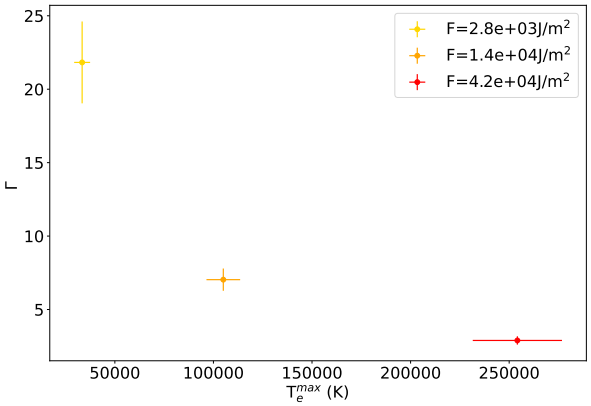

Figure 4.32: Plasma parameter $\Gamma = d/l$ (section 1.2.2), as a function of maximal T_e of the sub-zone in question. Central estimate and error bars obtain by sampling 50 model runs, from MCMC search results for a physical forward model of the Boltzmann equation 2.9.

Finally, the δ_s can also be recovered from the model runs since we have access to simulated absorbed energy density. The area over which a given energy density was absorbed is also known and corresponds to the area of the respective sub-zone. The volume over which 68% of the total absorbed energy is deposited will be this area multiplied by δ_s. Since the total absorbed energy is only dependent on the absorbed fluence and the area of absorption, only δ_s remains unknown. To discover it, the absorbed energy density was calculated for different δ_s until the experimental one was matched, for each of the fifty model runs sampled from the MCMC-generated ensemble and each of the sub-zones. The results are present in figure 4.33. In [56], a skin depth of $\delta_s = 27.2$ nm was reported, in a multi-pulse ablation study, with an 800 nm 40 fs laser, in broad agreement with our results.

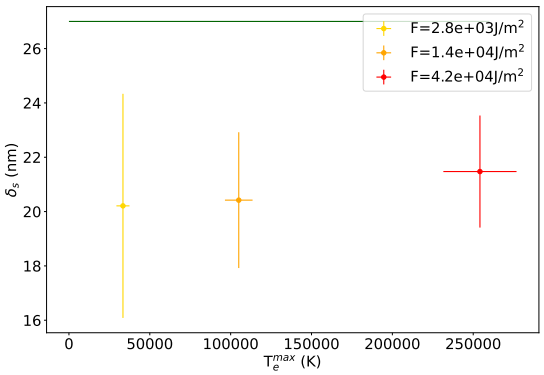

Figure 4.33: δ_s as a function of T_e calculated by inversion of the absorbed energy calculation for each sub-zone. Central estimate and error bars obtain by sampling 50 model runs, from MCMC search results for a a physical forward model of the Boltzmann equation 2.9. The blue line corresponds to the interpolating fit between the two degeneracy regimes shown in figure 1.2. The dark green line the [56] measurement.

Separate searches

The search performed previously, over the data of the three sub-zones all at the same time, was expanded here to three independent searches, with the free parameters no longer constrained to be the same for the three different zones. The ε_t parameter was set to - 6 eV due to time constraints, with the aim of reducing the dimensionality of our space of parameters and thus shortening the convergence time. Figure 4.34 shows the different marginalized posteriors and 2D correlations resultant from these searches, with the color code for incident fluency of the zone the same as in figure 4.35. The central estimations and 1σ error bars extracted from these posteriors are present in table 4.4 and together tell an interesting tale.

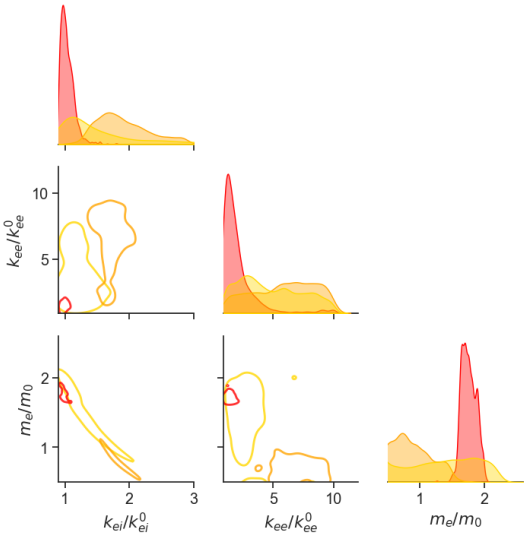

Figure 4.34: 2D correlations and marginalized posterior distributions of the free parameters of a physical forward model based on the Boltzmann equation 2.9, without the phonon term. Estimated via 3 different MCMC searches, with an ensemble of 40 walkers, evolved for a total of 15000 model evaluations and 20000 evaluations discarded as burn-in. Family of 150 μJ data series utilized. The darker line on the 2D correlation is the 1σ band.

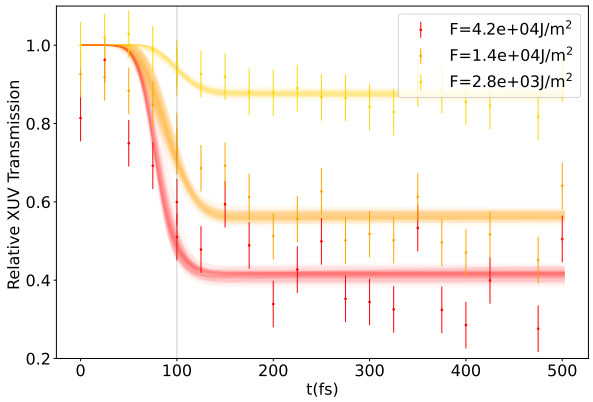

Figure 4.35: 50 model runs with parameters sampled independently from the ensembles generated by the MCMC searches, for a physical forward model of the Boltzmann equation 2.9, without the phonon term, plotted on top of the experimental data. In log scale with the laser fluence peaking at 100 fs.

To some extent, in κ_{ie} and even more patently in κ_{ee}, the 150 μJ innermost sub-zone seems to be the one more significantly constraining the parameters to be close to free electron-like. This might be indicative of a regime change, from the highest fluence sub-zone to the intermediate one, namely a move away from a highly correlated electrons state - that creates the Ti-specific DOS, in the cold solid.

For κ_{ie}, the third zone sees a suppression of the expected inverse correlation between κ_{ie} and m_{eff} in the joint search. This correlation is expected since, all else being, equal both a reduction in m_{eff} and κ_{ie} lead to a higher equivalent T_e being reached. As such they move inversely to one another to counteract this effect. As for κ_{ee}, this highest fluence sub-zone is the only one with a peak marginalized posterior at a value close to a free electron result. The other two zones show broad posteriors resulting in wide error bars that indicate an insensitivity of the observable changes in this parameter.

Zone	$\kappa_{ei}/\kappa^0_{ei}$	$\kappa_{ee}/\kappa^0_{ee}$	m_{eff}/m^0_{eff}
150 μJ, outer	$1.39^{+1.22}_{-0.46}$	$5.19^{+3.25}_{-2.81}$	$1.30^{+0.61}_{-0.71}$
150 μJ, middle	$1.78^{+0.46}_{-0.31}$	$5.94^{+2.70}_{-3.36}$ eV	$0.82^{+0.42}_{-0.33}$
150 μJ, inner	$1.01^{+0.12}_{-0.07}$	$1.62^{+1.28}_{-0.52}$ eV	$1.74^{+0.14}_{-0.10}$

Table 4.4: Most likely value and 1σ errors of the 3 MCMC searches performed, one for each sub-zone, for a physical forward model of the Boltzmann equation 2.9, without the phonon term.

It is also noticeable that the m_{eff} parameter does not decrease as the excitation level of the electrons increases. This would be expected since, in the Ti DOS (figure 2.3) the electrons closest to the Fermi energy are d band electrons, while the electrons closer to zero continuum energy (the last ones to get excited by the pump laser) are s like. This discrepancy might be due to ε_t being fixed in these simulations, since these would seem to suppress the strong correlations that exist between m_{eff} and ε_t and tend to fix m_{eff} to the corresponding value of ε_t that was previously fixed.

Finally, 4.35 displays a similarly good agreement to the joint search. Probably, the addition of ε_t to the search would produce an even better agreement, but that remains to be seen. The remainder of the graphs shown in the previous section do not change substantially and neither do their interpretations.

4.3.5 Summary and Conclusions

- A Boltzmann equation considering detailed e-e and e-i-pt collision terms was analytically simplified (momentum sums turned to integrals which were solved, not including electron-phonon and non-elastic e-i collisions). After the computational solution was implemented, we performed a study of the different effects of the screening parameters and the effective mass on the behavior of $f(k)$;

- A joint and three other separate MCMC searches were performed for a physical forward model based on the Boltzmann equation. This was done to simulate the absorption of the NIR pump by the Ti film on a fundamental level and check if longer-lived non-equilibrium electrons, created by the absorption process, contribute to the differences in slope between the TTM and the data;

- We can conclude that a nearly free electronic DOS adequately captures the broad effects observed in the data. Overall the m_{eff} was higher than one, which is expected for a d band metal;

- In the three separate searches, the highest fluence zone stands out as the one with the most peaked marginalized posteriors and the one with κ_{ie} and κ_{ee}, the inverse screening radius, closer to the one expected for a free electron gas. This has to do with the innermost zone achieving the highest T_e and, as such, being the one with the lowest e-e binding energy, relative to kinetic energy, i.e., the more free-electron-like;

- The joint search for the three sub-zones indicates fast thermalization of the electrons (in a situation close to figure 4.21), such that, for the experimental time resolution, non-equilibrium effects would not affect the observable. The three separate searches did not provide better agreement despite significantly more model freedom.

Chapter 5

Conclusions and Perspectives

Throughout this thesis, we presented an experimental study of isochorically heated warm dense Ti, out of equilibrium, probed with XUV in the bound-to-continuum region. The results are centered around two different physical forward models used to simulate the electronic distribution, in time, of the Ti electronic population. From this distribution, the experimental observable can be simulated, if we also know the distance in energy between the $3p$ states and the electron continuum. As such, both physical models were used for the likelihood function calculation, enabling MCMC searches, an algorithm aiming to independently sample the posterior probability distribution. Two different types of searches were performed, for each of the models: searches of the joint posterior distribution, concerning the data of several sub-zones in the same search; and independent searches, for each sub-zone.

The first forward model deployed was a TTM. It assumes instantaneous e-e thermalization but was expected to adequately model e-i energy exchange, if provided with the right coefficients. The MCMC searches of the joint posterior distributions revealed poor agreement between the model and experimental data when the cold Ti DOS was employed in the Lin-like calculations of C_e and G_{ei} (equations 2.16 and 2.17, respectively). The joint search results for a nearly free DOS, using the previously mentioned e-i coupling formula were more congruent with the experimental data, possibly because of the added freedom coming from the parameter-dependent DOS. They still reveal, however, some overestimation of the e-i energy exchange rate, for the lower fluence sub-zones, and an underestimation of it, for higher fluence sub-zones. We obtained better agreement between model results and data when the searches were run independently for each sub-zone. In this case, G_{ei} was considered a constant, for a given sub-zone, but allowed to vary between sub-zones, resulting in the most data-driven estimation of how this parameter changes with T_e, which behaves differently from theoretical predictions.

The second forward model utilized seeked to describe the detailed absorption and e-e relaxation processes and was based on solving the Boltzmann equation, with detailed collision integrals. Both joint and independent MCMC searches revealed good agreement between the model results and the data and revealed nearly-free screening coefficients of the electron gas. These results also appear to validate a TTM-like treatment of the experimental data, for a 50 fs time resolution, since in our best-fit simulations e-e equilibrium was established

in a few fs, after the laser excitation begins. Overall, we can conclude that e-e thermalization is quick, from the Boltzmann model, which validates the TTM assumption of instantaneous electron-electron equilibration, at our 50 fs time resolution. The independent MCMC searches of the Boltzamnn model also revealed the highest fluence zones to be constraining the parameters to more free-electron-like.

Correlations between the modeling parameters were found in the TTM runs, which show that a constant G_{ei} can be an effective assumption, in a large range of parameters, if such constant is adjusted for the incident pump intensity. A positive correlation was found between ε_t and δ_s/δ_s^0 while negative correlations prevail between δ_s/δ_s^0 and both G_{ei}/G_{ei}^0 and m_{eff}/m_{eff}^0. Overall a free electron gas and TTM can describe the data well. Values of G_{ei} were shown to increase with temperatures in the domain we probed while remaining in the range of previously published values.

In the future, both models would benefit from DFT Ti DOS calculations for elevated electronic and ionic temperatures. The Boltzmann model could be expanded to include non-elastic e-i collisions and thus the e-i energy exchange. Furthermore, different likelihood functions could be experimented with and Bayesian model selection could be attempted. More robust and faster optimization processes could also be experimented with [64]. On the experimental side, a measurement of ε_t is paramount for a reduction in the uncertainty over simulated T_e. Tighter control of the pump laser spatial profile and total energy would also contribute to results better tagged for average fluence. To better study non-equilibrium e-e effects, a shorter pump pulse would be required as well as an HHG spectrum centered closer to the Fermi energy.

5.1 Contributions

- Except for the raw data acquisition, all the data analysis and computational algorithms were done by the corresponding author;
- Poster presentation for the 13th International Conference on High Energy Density Laboratory Astrophysics, in Lisbon (HEDLA2022);
- Poster presentation at the Extreme Light Infrastructure (ELI) summer school (ELISS2022), in Szeged, Hungary - where it won the award of best scientific poster presentation;
- Presentation on the Radiative Properties of Hot Dense Matter conference, at the Los Alamos National Laboratory in Santa Fe, New Mexico.

.

Bibliography

[1] K. C. Engelhorn, "Ultrafast X-Ray Absorption Spectroscopy of Isochorically Heated Warm Dense Matter," Ph.D. dissertation, University of California, Berkeley, Jan. 2015.

[2] B. Xu and S. X. Hu, "Effects of electron-ion temperature equilibration on inertial confinement fusion implosions," *Phys. Rev. E*, vol. 84, p. 016 408, 1 Jul. 2011.

[3] R. P. Drake, L. Davison, and Y. Horie, *High-Energy-Density Physics: Fundamentals, Inertial Fusion, and Experimental Astrophysics*. Jan. 2006.

[4] F. Graziani, M. Desjarlais, R. Redmer, and S. Trickey, *Frontiers and Challenges in Warm Dense Matter*. Jan. 2014.

[5] K. Falk, "Experimental methods for warm dense matter research," *High Power Laser Science and Engineering*, 2018.

[6] K. Sugioka and H. Sun, "Review ultrafast lasers—reliable tools for advanced materials processing," *Light: Science Applications*, vol. 3, e149, Apr. 2014.

[7] M. Braun, P. Gilch, and W. Zinth, *Ultrashort Laser Pulses in Biology and Medicine*. Jan. 2008.

[8] B. Huettner *et al.*, "The theory of laser materials processing," in Apr. 2013, pp. 315–338.

[9] K. Sugioka and Y. Cheng, "Femtosecond laser three-dimensional micro- and nanofabrication," *Applied Physics Reviews*, vol. 1, no. 4, p. 041 303, 2014. eprint: `https://doi.org/10.1063/1.4904320`.

[10] N. Medvedev and I. Milov, "Electron-phonon coupling in metals at high electronic temperatures," *Phys. Rev. B*, vol. 102, p. 064 302, 6 Aug. 2020.

[11] W. Ebeling, V. Fortov, and V. Filinov, *Quantum Statistics of Dense Gases and Nonideal Plasmas*. Jan. 2017.

[12] A. Ng, T. Ao, F. Perrot, M. W. C. Dharma-Wardana, and M. E. Foord, "Idealized Slab Plasma approach for the study of Warm Dense Matter," Tech. Rep.

[13] D. HOFFMANN *et al.*, "Present and future perspectives for high energy density physics with intense heavy ion and laser beams," *Laser and Particle Beams*, vol. 23, no. 01, Mar. 2005.

[14] Bob Nagler et al, "Turning solid aluminium transparent by intense soft X-ray photoionization," *Nature Physics*, vol. 5, no. 9, Sep. 2009.

[15] G. O. Williams *et al.*, "Tracking the ultrafast xuv optical properties of x-ray free-electron-laser heated matter with high-order harmonics," *Phys. Rev. A*, vol. 97, p. 023 414, 2 Feb. 2018.

[16] Y. A. Il'inskii and L. V. Keldysh, *Electromagnetic Response of Material Media*. Boston, MA: Springer US, 1994.

[17] B. Rethfeld, D. Ivanov, M. Garcia, and S. Anisimov, "Modelling ultrafast laser ablation," *Journal of Physics D: Applied Physics*, vol. 50, p. 193 001, May 2017.

[18] Mark Fox, *Optical properties of solids*, 2nd. Oxford University Press, 2001.

[19] E. G. Gamaly and A. V. Rode, *Physics of ultra-short laser interaction with matter: From phonon excitation to ultimate transformations*, 2013.

[20] L. Spitzer and C. J. Cook, "Physics of Fully Ionized Gases: No. 3 of Interscience Tracts on Physics and Astronomy," *Physics Today*, vol. 10, no. 1, Jan. 1957.

[21] A. Einstein, "On the electrodynamics of moving bodies," *Annalen Phys.*, vol. 17, 1905.

[22] K. Eidmann, J. Meyer-Ter-Vehn, T. Schlegel, and S. Hü, "Hydrodynamic simulation of subpicosecond laser interaction with solid-density matter," Tech. Rep.

[23] B. Rethfeld, A. Kaiser, M. Vicanek, and G. Simon, "Ultrafast dynamics of nonequilibrium electrons in metals under femtosecond laser irradiation," *Physical Review B - Condensed Matter and Materials Physics*, vol. 65, no. 21, pp. 2 143 031–21 430 311, Jun. 2002.

[24] M. Volkov *et al.*, "Attosecond screening dynamics mediated by electron-localization," Tech. Rep.

[25] N. M. Bulgakova, R. Stoian, A. Rosenfeld, I. V. Hertel, and E. E. B. Campbell, "Electronic transport and consequences for material removal in ultrafast pulsed laser ablation of materials," *Physical Review B*, vol. 69, no. 5, Feb. 2004.

[26] S. I. Anisimov, B. L. Kapeliovich, T. L. Perel'man, and L. D. Landau, "Electron emission from metal surfaces exposed to ultrashort laser pulses," Tech. Rep., 1975.

[27] L. Landau, E.M. Lifshitz, and L.P. Pitaevskii, *Electrodynamics of Continuous Media*. Pergamon Press, 1984, vol. 8.

[28] J. Vorberger and D. O. Gericke, "Theory of electron-ion energy transfer applied to laser ablation," 2012.

[29] F. Dorchies and V. Recoules, *Non-equilibrium solid-to-plasma transition dynamics using XANES diagnostic*, Oct. 2016.

[30] M. E. Povarnitsyn, T. E. Itina, K. V. Khishchenko, and P. R. Levashov, "Multi-material two-temperature model for simulation of ultra-short laser ablation," *Applied Surface Science*, vol. 253, no. 15, May 2007.

[31] M. Bonitz *et al.*, "Ab initio simulation of warm dense matter," *Physics of Plasmas*, vol. 27, no. 4, Apr. 2020.

[32] P. Hohenberg and W. Kohn, "Inhomogeneous Electron Gas," *Physical Review*, vol. 136, no. 3B, Nov. 1964.

[33] N. D. Mermin, "Thermal Properties of the Inhomogeneous Electron Gas," *Physical Review*, vol. 137, no. 5A, Mar. 1965.

[34] W. Kohn and L. J. Sham, "Self-Consistent Equations Including Exchange and Correlation Effects," *Physical Review*, vol. 140, no. 4A, Nov. 1965.

[35] E. Bévillon, J. P. Colombier, V. Recoules, and R. Stoian, "Free-electron properties of metals under ultrafast laser-induced electron-phonon nonequilibrium: A first-principles study," *Physical Review B - Condensed Matter and Materials Physics*, vol. 89, no. 11, Mar. 2014.

[36] G. Kresse and J. Hafner, "Ab initio molecular dynamics for liquid metals," *Physical Review B*, vol. 47, no. 1, Jan. 1993.

[37] *Sesame database*, `https://www.lanl.gov/org/ddste/aldsc/theoretical/physics-chemistry-materials/sesame-database.php`.

[38] F. Dorchies *et al.*, "Unraveling the Solid-Liquid-Vapor Phase Transition Dynamics at the Atomic Level with Ultrafast X-Ray Absorption Near-Edge Spectroscopy," *Physical Review Letters*, vol. 107, no. 24, Dec. 2011.

[39] J. F. Seely and E. G. Harris, "Heating of a plasma by multiphoton inverse bremsstrahlung," *Phys. Rev. A*, vol. 7, pp. 1064–1067, 3 Mar. 1973.

[40] B. C. Rethfeld, "Mikroskopische prozesse bei der wechselwirkung von festkörpern mit laserpulsen im subpikosekundenbereich," Ph.D. dissertation, Aug. 1999.

[41] Z. Lin, L. V. Zhigilei, and V. Celli, "Electron-phonon coupling and electron heat capacity of metals under conditions of strong electron-phonon nonequilibrium," *Physical Review B*, vol. 77, no. 7, Feb. 2008.

[42] L. Waldecker, R. Bertoni, R. Ernstorfer, and J. Vorberger, "Electron-phonon coupling and energy flow in a simple metal beyond the two-temperature approximation," *Phys. Rev. X*, vol. 6, p. 021 003, 2 Apr. 2016.

[43] Y. V. Petrov, N. A. Inogamov, and K. P. Migdal, "Thermal conductivity and the electron-ion heat transfer coefficient in condensed media with a strongly excited electron subsystem," *JETP Letters*, vol. 97, no. 1, Mar. 2013.

[44] J. Lindhard, "On the properties of a gas of charged particles," *Kgl. Danske Videnskab. Selskab Mat.-fys. Medd.*, vol. 28, no. 8, Jan. 1954.

[45] B. Y. Mueller and B. Rethfeld, "Relaxation dynamics in laser-excited metals under nonequilibrium conditions," *Phys. Rev. B*, vol. 87, p. 035 139, 3 Jan. 2013.

[46] B. Mahieu *et al.*, "Probing warm dense matter using femtosecond x-ray absorption spectroscopy with a laser-produced betatron source," *Nature Communications*, vol. 9, Aug. 2018.

[47] P. Corkum and F. Krausz, "Attosecond science," *Nature Physics*, vol. 3, pp. 381–387, 2007.

[48] A. Lévy *et al.*, "X-Ray Diagnosis of the Pressure Induced Mott Nonmetal-Metal Transition," *Physical Review Letters*, vol. 108, no. 5, Jan. 2012.

[49] F. Dorchies *et al.*, "Time evolution of electron structure in femtosecond heated warm dense molybdenum," *Physical Review B*, vol. 92, no. 14, Oct. 2015.

[50] J.-W. Lee *et al.*, "Investigation of nonequilibrium electronic dynamics of warm dense copper with femtosecond x-ray absorption spectroscopy," *Phys. Rev. Lett.*, vol. 127, p. 175 003, 17 Oct. 2021.

[51] M. F. Kasim, T. P. Galligan, J. Topp-Mugglestone, G. Gregori, and S. M. Vinko, "Inverse problem instabilities in large-scale modeling of matter in extreme conditions," *Physics of Plasmas*, vol. 26, no. 11, p. 112 706, 2019. eprint: https://doi.org/10.1063/1.5125979.

[52] P. Gregory, *Bayesian Logical Data Analysis for the Physical Sciences: A Comparative Approach with Mathematica® Support*. Cambridge University Press, 2005.

[53] D. Foreman-Mackey, D. W. Hogg, D. Lang, and J. Goodman, "emcee: The MCMC Hammer,", vol. 125, no. 925, p. 306, Mar. 2013. arXiv: 1202.3665 [astro-ph.IM].

[54] J. Goodman and J. Weare, "Ensemble samplers with affine invariance," *Communications in Applied Mathematics and Computational Science*, vol. 5, no. 1, pp. 65–80, Jan. 2010.

[55] P. Virtanen *et al.*, "SciPy 1.0: Fundamental Algorithms for Scientific Computing in Python," *Nature Methods*, vol. 17, pp. 261–272, 2020.

[56] M. Hashida, M. Yasuhiro, N. Takaya, S. Mashiro, I. Shunsuke, and S. Shuji, "Threshold Fluence for Femtosecond Laser Nanoablation for Metals," *Electronics and Communication in Japan*, vol. 99, pp. 88–95, 2016.

[57] G. Kresse and J. Hafner, "Ab initio molecular dynamics for liquid metals," *Phys. Rev. B*, vol. 47, pp. 558–561, 1 Jan. 1993.

[58] G. Kresse and J. Furthmüller, "Efficiency of ab-initio total energy calculations for metals and semiconductors using a plane-wave basis set," *Computational Materials Science*, vol. 6, no. 1, pp. 15–50, 1996.

[59] ——, "Efficient iterative schemes for ab initio total-energy calculations using a plane-wave basis set," *Phys. Rev. B*, vol. 54, pp. 11 169–11 186, 16 Oct. 1996.

[60] G. Kresse and J. Hafner, "Norm-conserving and ultrasoft pseudopotentials for first-row and transition elements," *Journal of Physics: Condensed Matter*, vol. 6, no. 40, p. 8245, Oct. 1994.

[61] G. Kresse and D. Joubert, "From ultrasoft pseudopotentials to the projector augmented-wave method," *Phys. Rev. B*, vol. 59, pp. 1758–1775, 3 Jan. 1999.

[62] C. R. H. andK. Jarrod Millman *et al.*, "Array programming with numpy," *CoRR*, vol. abs/2006.10256, 2020. arXiv: 2006.10256.

[63] N. Hansen. "The cma evolution strategy." (2015), [Online]. Available: http://www.cmap.polytechnique.fr/~nikolaus.hansen/cmaesintro.html.

[64] S. S. Rosa and et al, "Maximizing mrna vaccine production with bayesian optimization.," *Biotechnology and Bioengineering*, vol. 119, no. 8,

[65] J. Vorberger, D. O. Gericke, T. Bornath, and M. Schlanges, "Energy relaxation in dense, strongly coupled two-temperature plasmas," *Physical Review E*, vol. 81, no. 4, Apr. 2010.

[66] E. Principi *et al.*, "Free electron laser-driven ultrafast rearrangementöf the electronic structure in Ti," *Structural Dynamics*, vol. 3, no. 2, Mar. 2016.

[67] G. v. Minnigerode, "Göran Grimvall, E. P. Wohlfahrt (Eds.): The Electron-Phonon Interaction in Metals, Vol. 16, aus: Selected Topics in Solid State Physics. North Holland Publishing Company, Amsterdam, New York, Oxford 1981. 304 Seiten, Dfl 125,-," *Berichte der Bunsengesellschaft für physikalische Chemie*, vol. 87, no. 5, May 1983.

[68] J. P. Colombier, P. Combis, F. Bonneau, R. Le Harzic, and E. Audouard, "Hydrodynamic simulations of metal ablation by femtosecond laser irradiation," *Physical Review B - Condensed Matter and Materials Physics*, vol. 71, no. 16, 2005.

[69] K. K. Anoop, M. P. Polek, R. Bruzzese, S. Amoruso, and S. S. Harilal, "Multidiagnostic analysis of ion dynamics in ultrafast laser ablation of metals over a large fluence range," *Journal of Applied Physics*, vol. 117, no. 8, Feb. 2015.

[70] N. A. Inogamov *et al.*, "Nanospallation induced by an ultrashort laser pulse," *Journal of Experimental and Theoretical Physics*, vol. 107, no. 1, Jul. 2008.

[71] M. E. Povarnitsyn, K. V. Khishchenko, and P. R. Levashov, "Phase transitions in femtosecond laser ablation," *Applied Surface Science*, vol. 255, no. 10, pp. 5120–5124, Mar. 2009.

[72] F. J. Blatt and C. S. Koonce, *Physics of Electronic Conduction in Solids*. Aug. 1969, vol. 22.

[73] F. Bencivenga *et al.*, "Reflectivity enhancement in titanium by ultrafast XUV irradiation," *Scientific Reports*, vol. 4, May 2014.

[74] A. B. Patel and H. Sheng, "Structure and atomic transport of liquid titanium from a pair potential model," *Physical Review B*, vol. 102, no. 6, Aug. 2020.

[75] V. Recoules and S. Mazevet, "Temperature and density dependence of XANES spectra in warm dense aluminum plasmas," *Physical Review B*, vol. 80, no. 6, Aug. 2009.

[76] R. Ernstorfer, M. Harb, C. T. Hebeisen, G. Sciaini, T. Dartigalongue, and R. J. D. Miller, "The Formation of Warm Dense Matter: Experimental Evidence for Electronic Bond Hardening in Gold," *Science*, vol. 323, no. 5917, Feb. 2009.

[77] X. Li and Y. Guan, *Theoretical fundamentals of short pulse laser-metal interaction: A review*, Sep. 2020.

[78] M. HASHIDA, Y. MIYASAKA, T. NISHII, M. SHIMIZU, S. INOUE, and S. SAKABE, "Threshold Fluence for Femtosecond Laser Nanoablation for Metals," *Electronics and Communications in Japan*, vol. 99, no. 10, Oct. 2016.

[79] S. M. Vinko *et al.*, "Time-Resolved XUV Opacity Measurements of Warm Dense Aluminum," *Physical Review Letters*, vol. 124, no. 22, Jun. 2020.

[80] V. V. Temnov, K. Sokolowski-Tinten, P. Zhou, and D. Von Der Linde, "Ultrafast imaging interferometry at femtosecond-laser-excited surfaces," Tech. Rep., 2006.

[81] S. Anisimov *et al.*, "Pulsed laser evaporation: equation-of-state effects," *Applied Physics A: Materials Science & Processing*, vol. 69, no. 6, Dec. 1999.

[82] A. Bykov, F. Paerels, and V. Petrosian, "Equilibration processes in the warm-hot intergalactic medium," *Space Science Reviews*, vol. 134, Jan. 2008.

[83] W. Ebeling, W. Kraeft, and D. Kremp, *Theory of Bound States and Ionization Equilibrium in Plasmas and Solids*. Jan. 1976.

[84] F. Bisio *et al.*, "Long-lived nonthermal electron distribution in aluminum excited by femtosecond extreme ultraviolet radiation," *Phys. Rev. B*, vol. 96, p. 081 119, Aug. 2017.

Appendix A

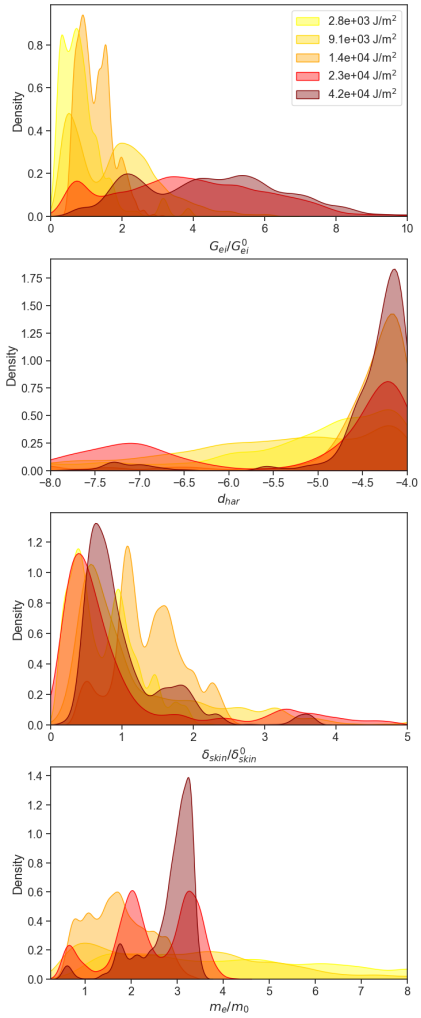

Figure A.1: Marginalized posterior distributions of MCMC searches performed for a physical forward model of a TTM, with constant G_{ei} and DOS as in equation 4.4. Ensemble of 40 walkers. The darker line on the 2D correlation is the 1σ band.